A Morphological Analysis of the Galaxy Cluster XLSSC 122

by

Ophélie Karishma Leste
B.Sc., Saint Mary's University, 2021
A Thesis Submitted in Partial Fulfillment of the
Requirements for the Degree of

MASTER OF SCIENCE

in the Department of Physics and Astronomy

A Morphological Analysis of the Galaxy Cluster XLSSC 122

by

Ophélie Karishma Leste
B.Sc., Saint Mary's University, 2021

Supervisory Committee

Dr. J. Willis, Supervisor
(University of Victoria Department of Physics and Astronomy)

Dr. J. Di Francesco, Member
(University of Victoria Department of Physics and Astronomy, NRC Herzberg)

Abstract

We present a morphological analysis of the 29 spectroscopically confirmed members of the most massive galaxy cluster at $z \sim 2$, XLSSC 122. The cluster was discovered in the XMM Large Scale Structure survey as a faint, extended X-ray source and was later confirmed via a Sunyaev-Zel'dovich decrement along its line of sight. We perform photometry using STATMORPH on images of the cluster members from the *Hubble Space Telescope (HST)* Wide Field Camera (WFC3) in the F140W and F105W bands. We perform visual assesment of the images, as well as non-parametric morphological analyses based on measurements such as the concentration C, asymmetry A, Gini and M_{20} to classify the cluster members as being bulge-dominated, disky or possible mergers. The properties of the XLSSC 122 members show clear evidence of bimodality. The bulge-dominated galaxies are redder, older and are found in the denser regions of the cluster, while the galaxies showing disturbed features are bluer, younger, and are found towards the outskirts of the cluster. XLSSC 122 is also found to be deficient of the blue and disturbed galaxy populations compared to galaxies from CANDELS/3D-HST field surveys. We further consider results from dark-matter only cosmological simulations presented in COSMOSIM to derive the merger history of the members in cluster halos such as XLSSC 122 at the epoch of observation. The analysis of the simulated data along with the morphological observations, suggest that the galaxy interactions that induce structural disturbances in the blue population of XLSSC 122 members occurred at redshifts in the range $2 < z < 3$. This epoch is likely to indicate to the time prior to the infall of these galaxies into the virial radius of the cluster, where galaxy mergers and star formation are eventually suppressed, resulting in their evolution into bulge-dominated red-sequence galaxies.

Contents

List of Tables

List of Figures

Acknowledgements

I would like to thank:

Jon Willis, for giving me the opportunity to contribute to this work, for showing and incredible amount of patience and understanding and for sharing his interests in studies outside of astronomy.

Arianne Trudeau, for sharing their work on XLSSC 122.

Doug Rennehan, for the thorough explanations on the workings of COSMOSIM.

Elizaveta Sazonova, for sharing their data on the morphological analysis of the 4 additional high redshift clusters.

Rebecca Canning, for the instructions on extracting the field galaxy sample.

Henry Ngo, for the incredible amount of support and help while undertaking a complete career change.

The Ministry of Education of Mauritius, for the financial help, without which this journey would not have begun.

Dedication

This work is dedicated:

To the little girl who travelled across the planet, starting her journey coming from a modest background on a tiny unknown island in the middle of the ocean, following her dream of understanding the workings of the Universe and her own mind. A dream, she continues to achieve.

To my mother, Devi who has always strived for me to be able to follow my dreams and always show unconditional support.

To my best friend, Renata who has always been by my side.

To all those who have been supporting me.

Chapter 1

Introduction

1.1 Discovery of Galaxy Clusters

Galaxy clusters are the most massive environments of the Universe. Catalogues of clusters date as far back as the 18^{th} century, among observations made by Charles Messier and Wilhelm Herschel (Messier, 1781; Herschel, 1785). At the time, the notion of the structure of galaxies as known today was still unestablished, and they were referred to as 'nebulae.' Early astronomers of the 18^{th} and 19^{th} century were able to perceive that these 'nebulae' were distinct from stars and comets due to their fuzzy structures and fixed positions on the plane of the sky. As catalogues of these objects became larger, some 'nebulae' appeared to have a tendency to cluster. It was only after the studies of Edwin Hubble that the idea was put forward that some of these nebulae were actually extragalactic and they were then recognised as systems of complete stellar populations (Hubble, 1925, 1926a,b). Consequently, the perspective of astronomers on the scale of the universe was revolutionised upon realising that the observed concentrations of nebulae, were actually colossal clusters of galaxies.

In subsequent studies, measurements of galaxy velocities were made, leading to the assumption that galaxies in clusters are in virial equilibrium[1], that in turn permit the derivation of the mass encompassed within clustered galaxy regions (Hubble & Humason, 1931). The masses of the two nearby galaxy clusters, Virgo and Coma were found using such measurements to be $4.5 \times 10^{13} M_{\odot}$ and $10^{14} M_{\odot}$, respectively (Zwicky, 1933, 1937; Smith, 1936). These studies revealed that the average mass per galaxy within those clusters exceeds the galaxy stellar mass measured from the luminosity, by

[1] refers to when the kinetic energy is $-\frac{1}{2}$ the total gravitational potential energy of a stable, self-gravitating body.

a factor of about 200 to 400. Attempts to explain this puzzling observation, resulted in the speculations that the mass discrepancy is due to the presence of an invisible, uniformly distributed cloud of 'internebular' material, dark matter.

The concept of dark matter became more popular following the discovery of the hot from observations of galaxy clusters at X-ray wavelengths (Cavaliere et al., 1971; Forman et al., 1972; Meekins et al., 1971). The ICM is made up of hot diffuse gas and plasma, which account for the majority of the baryonic matter mass in galaxy clusters, with the other baryonic component being the mass from the stellar population within the galaxies themselves(Kravtsov & Borgani, 2012). The added mass of the ICM, however, was still not sufficient to explain the mass discrepancy, which hence reinforced the need for dark matter. For instance, the Coma cluster is found to be composed of 85% dark matter, 14% baryonic matter in the ICM, and just 1% baryonic matter within its galaxy members (Łokas & Mamon, 2003).

Galaxy clusters, being the most massive structures of gravitationally bound galaxies, provide a unique laboratory to investigate the effects due to repeated interactions between galaxies, the ICM, and dark matter and better understand their connection to the large-scale structure of the Universe.

1.2 Colour Bimodality of Galaxy Cluster Members

An interesting property observed for galaxies in clusters, is that they can be classified into two distinct groups based on their colour. Colour is often used as a proxy for describing the star formation activity and age of a galaxy. Galaxies that are young and actively forming stars are typically bluer while older galaxies with low star formation rates tend to be redder. These relationships have been long known, based on the development of the colour-magnitude diagram (CMD), which made the bimodality of galaxies more apparent (de Vaucouleurs, 1961; Chester & Roberts, 1964; Visvanathan & Sandage, 1977). The CMD separates galaxy populations into two main groups: the red-sequence and the blue cloud. As galaxies evolve and become older, their star formation activity is eventually suppressed and they become redder. Assuming this evolution suite, the position of galaxies on the CMD can trace their evolution from the blue cloud to the red-sequence, as shown in Figure 1.1 (Ferreras et al., 2021).

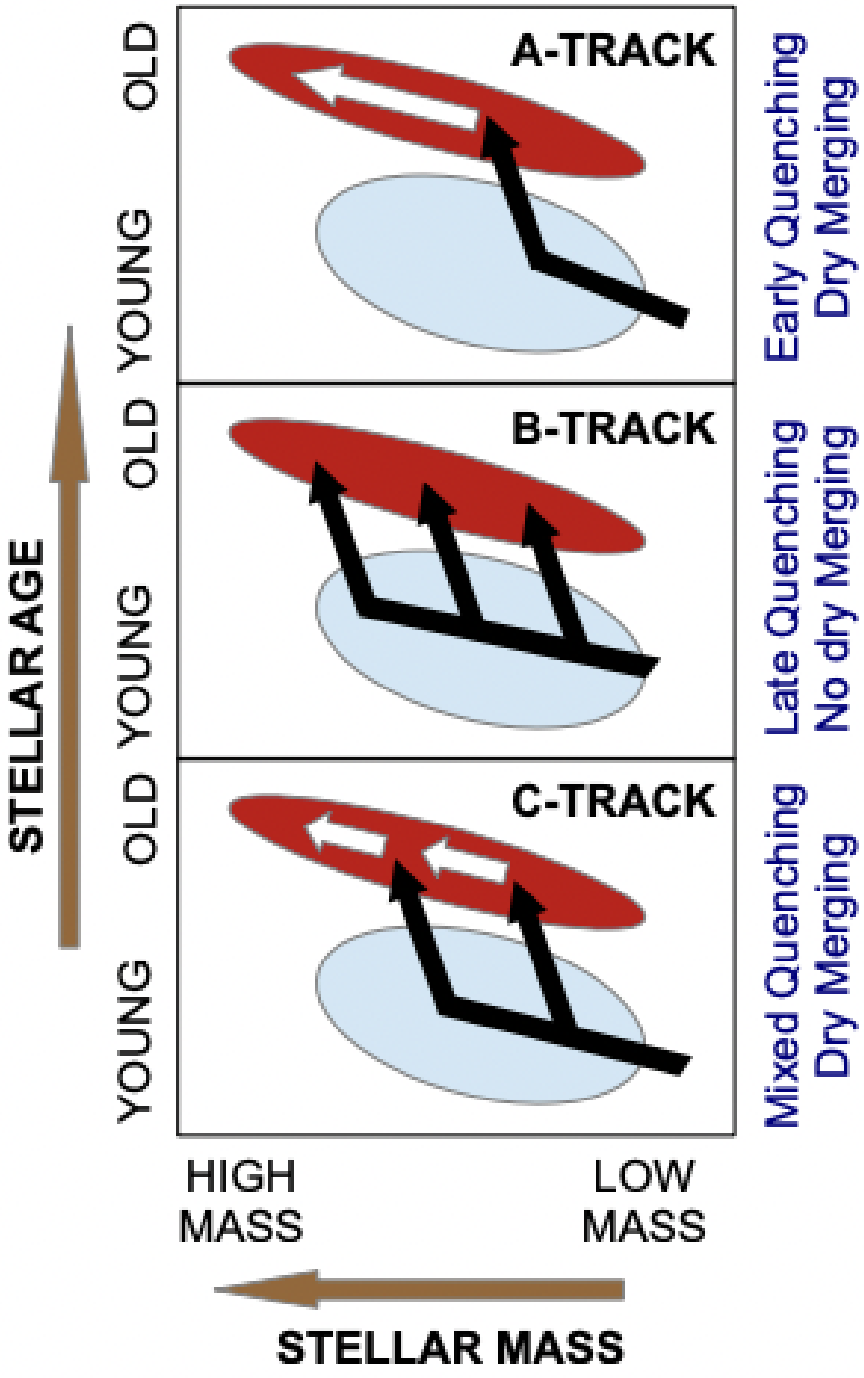

Figure 1.1: Schematics of galaxy evolution from the blue cloud to the red-sequence on the CMD. Black arrows show the galaxy evolution path. Figure from Ferreras et al. (2021).

The colour limit of the red-sequence, was observed to become redder with increasing environmental density (Balogh et al., 2004). As such, the stark distinction between the environment within clusters and the rest of the universe (i.e. in the field) becomes apparent when comparing the CMDs of these galaxy populations. Baldry et al. (2006) shows that the proportion of red-sequence galaxies, is larger in cluster populations than in the field. This difference suggests that galaxies in the dense environment of clusters may have experienced a faster evolution from the blue cloud to the red-sequence than field galaxies.

1.3 Galaxy Cluster Detection

As the importance of galaxy cluster studies became apparent to constrain parameters of the large scale structure of the Universe, methods to detect clusters efficiently at low to high redshifts were developed. The three main methods generally used are presented below.

1.3.1 X-ray

The emission resulting from the deceleration of a charged particle when deflected electromagnetically is called bremsstrahlung radiation. The loss of kinetic energy when the particles decelerate due to the interaction with the ICM, is emitted as a photon in the X-ray regime (Cavaliere et al., 1971). The hardness of X-ray emission shows dependence on the ICM temperature, which is consistent with the velocities of the clustered galaxies. According to the mass-temperature relation, which states that the temperature of the ICM is proportional to the cluster mass, i.e. $T_{gas} \propto M_{vir}^{2/3}$ (Shimizu et al., 2003), a galaxy cluster with a mass of $10^{14} M_{\odot}$, such as the Coma cluster, will have an ICM temperature of ~ 8 keV. At these high temperatures (≥ 0.9 keV) the gas content is expected to be fully ionised, and thus the primary form of emission occurs through free-free (bremsstrahlung) emission (Mo et al., 2010). As such the X-ray emission can be used as a signal to detect galaxy clusters within surveys such as the ROSAT-ESO Flux-limited X-Ray Survey (Böhringer et al., 2002) and the XMM Survey (Mehrtens et al., 2012).

1.3.2 SZ effect

Photons from the Cosmic Microwave Background (CMD) interact with thermal electrons of the hot ICM through inverse Compton scattering. As a result, the CMD spectrum towards the cluster is modified to higher energy values. When viewed in a limited frequency filter, regions where galaxy clusters lie can appear dimmer than the field. This dimming is termed as the Sunyaev-Zel'dovich (SZ) decrement (Sunyaev & Zeldovich, 1970). It is therefore possible to comb through millimeter wavelength observations of the CMD for the presence of SZ decrements that signify the presence of galaxy clusters.

1.3.3 Red-sequence Identification

The identification of galaxy overdensities as clusters goes back to Abell (1958). The detection of these overdensities relies upon the colour bimodality of rich clusters, i.e. the presence of the homogeneous red-sequence population. As a result, several methods have been developed using the red-sequence as a direct indicator of overdensity. Cluster finding algorithms such as redMapper (Rykoff et al., 2014), find galaxy clusters by mapping the density of galaxies in a survey within narrow colour slices, giving greater weight to brighter galaxies and flagging the highest overdensities as candidate clusters (Gladders et al., 2007).

An advantage of this method of cluster detection and membership determination is its simplicity, which allows the probing of clusters in imaging data of large-scale surveys at optical and infrared wavelengths (Gladders & Yee, 2000). At higher redshifts, however, the contrast of a cluster of galaxies against the background of non-cluster galaxies becomes lower. Therefore, this lower contrast increases the likelihood that cluster membership determined using the red-sequence identification method will be contaminated by field interlopers.

1.4 Morphology

Back when galaxies were still thought to be 'nebulae,' descriptions of their structure and morphology were already being discussed (Wolf, 1908). With developments in photography, visual analysis and classification of the structure of 'nebulae' were made possible, leading to the modern form of galaxy classification developed by Edwin Hubble, known as the *Hubble Tuning Fork* (Hubble, 1926a). The Hubble sequence, as

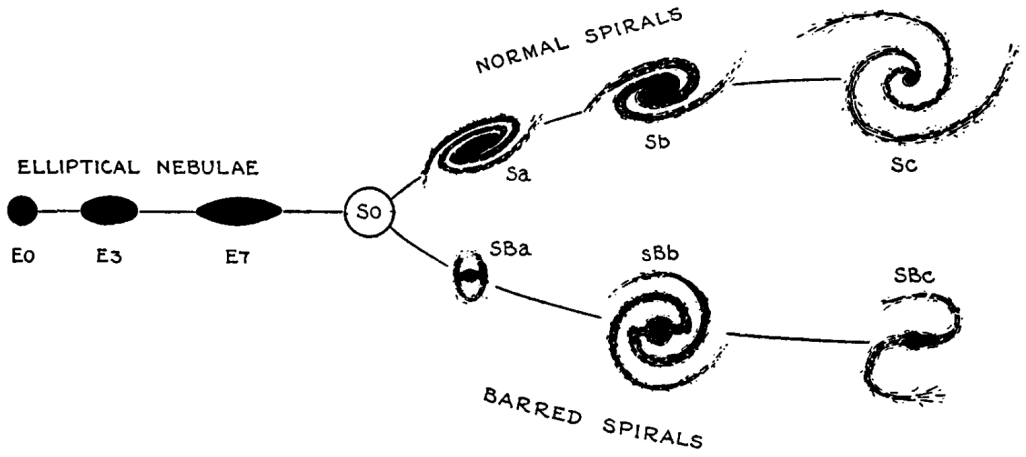

Figure 1.2: Hubble Sequence of Nebular Type from *The Realm of the Nebulae* (Hubble, 1936).

shown in Figure 1.2, separates galaxies into two main types: ellipticals (S0, E0 to E7) and spirals (Sa, Sb, Sc). A revised version was later developed to include structures such as bars, rings, and other internal structures by de Vaucouleurs (1959). Ellipticals tend to be smoother and bulge-dominated, while spirals present more substructures and are more disk-like. During the development of this classification system, galaxies were thought to evolve along the Hubble Sequence from left to right, starting off as ellipticals and gaining structural complexity as they mature into spirals. As a result, elliptical galaxies were termed early-type galaxies, while spirals were termed late-type galaxies.

Concurrent studies established that the visual structures of galaxies could be linked to their intrinsic properties (Holmberg, 1958). Elliptical galaxies are found to be more massive and redder, with low star formation rates (SFR) and low rotational velocities, while spirals to be less massive, bluer and have active star formation and higher rotational velocities (Bernardi et al., 2010). The morphological classification, hence closely relate to the colour bimodality expressed in the CMD. These observations contributed to disrupting the evolutionary scheme following the Hubble sequence, as it is unlikely for ellipticals to rotate spontaneously more quickly to become spirals, without external processes. Nevertheless, the terms early-type and late-type are still commonly used to describe ellipticals and spirals, respectively.

The morphology of a galaxy is highly dependent on the activity of its stellar population (Buta, 2013). Galaxies undergoing active star formation, generally have

morphologies distinct from those of passive galaxies (Kennicutt, 1998). In local galaxies, the gas-rich, clumpy arms of spiral galaxies are locations of active star formation. On the other hand, ellipticals show rapidly declining star formation rates or no star formation activity whatsoever. The main processes responsible for the triggering and cessation of star formation in galaxies have been the subject of multiple studies and debates (Stewart et al., 1999; Grudić et al., 2018; Luisi et al., 2021).

One of the ways through which galaxies grow in mass is through galaxy interactions and mergers. During these events, the resulting gas dynamics, affects the structure of the interacting galaxies, leaving them with irregular features, and imprints in the morphology of the merger remnant (Joseph & Wright, 1985; Sanders & Mirabel, 1996). For instance, interactions between two gas-rich galaxies, known as a 'wet merger,' may induce compression of their constituent gas and cause shocks, triggering additional star formation and resulting in clumpy disks. Another possibility arising from of this kind of interaction, is the increase in nucleic activity, which may result in the disruption of the disks, and the formation of an elliptical merger remnant (Lin et al., 2008; Barton et al., 2000; Pearson et al., 2019; Lotz et al., 2008b). Conversely, 'dry mergers', which occur between gas-poor galaxies and are generally smoother with low SFR. Dry mergers do not cause dramatic changes in the star forming activity, but are one of the main methods by which massive red galaxies accrete more stellar mass. Consequently, the morphology of a galaxy can be used as a merger indicator and gives us insights on its formation history and the paths through which its evolution took place.

With the advent of deep-field surveys and imaging with better resolution from the Hubble Space Telescope (HST), observations of galaxies at larger distances and higher redshifts became possible. These data unveiled further aspects of the formation of galaxies, for instance, the structure of distant galaxies is significantly different from what is observed in the local universe. Namely, galaxies appear to progress from being small, irregular, and star-forming at high redshifts to being the massive, red galaxies found at low redshifts, and that the Hubble sequence was not in place at $z > 1$. Furthermore, following the studies done by Madau & Dickinson (2014), the star formation rate density in the universe was found to peak around redshift $z \sim 2.5$, which is known as the *cosmic high noon*. Studying the morphology of galaxies at this epoch opens another window to our perspective on the state of the universe during its early stages.

With more technological progress and the invention of Charged Coupled Devices

(CCD), detailed quantitative measurements of the light distribution of galaxies became possible, which revolutionised the morphological studies of galaxies (Peng et al., 2002; Simard et al., 2011). Thus, the classification of galaxies based on their structures no longer relied solely on the qualitative interpretation of their features. These measurements facilitate the comparison of galaxies at different redshifts.

One of the most common methods for measuring galaxy structures is known as the CAS system (Conselice, 2003), which describes the concentration, asymmetry, and smoothness of the light distribution of galaxy images, and thus captures their major structural features. Different types of galaxies are found to have different combinations of these parameters. For instance, ellipticals generally have high concentration values, while spirals have low smoothness values. Other parameters such as the ones presented by Abraham et al. (2003) and Lotz et al. (2004), include the Gini and M_{20} coefficients, which are used extensively in this study.

1.4.1 Morphology-Density Relation

The morphologies of galaxies correlate with the local environment they occupy. Dressler (1980) found that the fraction of elliptical and non-star-forming galaxies increases as the density of the local environment increases, while the fraction of spirals and star-forming galaxies decreases. This trend is known as the morphology-density relation (Fig.1.3). Additionally, the intrinsic properties of galaxies are affected by environmental processes that impact their star formation and mass accretion rates, such as ram-pressure stripping and tidal stripping during galaxy interactions and mergers (Tempel et al., 2011; Papovich et al., 2018).

Moreover, the properties of galaxies within the same morphological classification, can differ depending on their local environment. For instance, spiral galaxies in clusters tend to be redder and have lower star formation rates than field spirals do(Kennicutt, 1983; Gavazzi et al., 2006). This observation, together with the morphology-density relation, suggest that galaxies in denser environments evolve faster than in the field and are experiencing mechanisms that shut down star formation. Several studies find that the morphology-density relation was already in place at $z \sim 1$ (Postman et al., 2005; Smith et al., 2005; Capak et al., 2007). The comparison of galaxy morphologies at higher redshift between clusters and the field may shed light on the evolutionary mechanisms through which the morphology-density relation observed in the local universe was established.

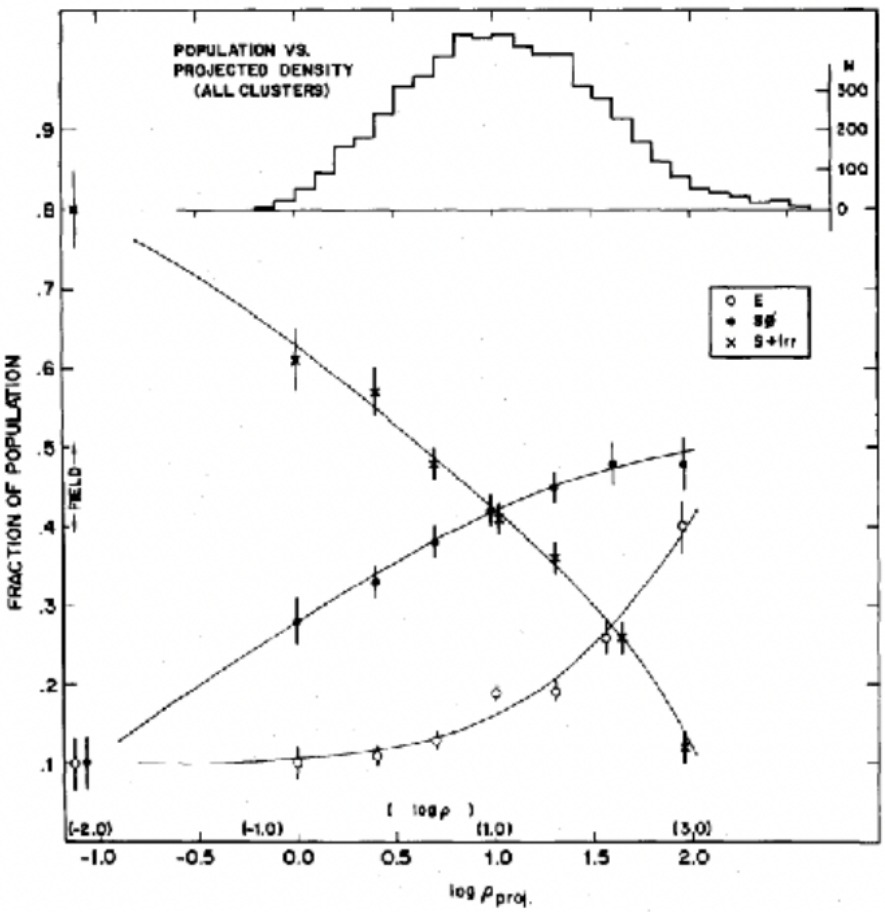

Figure 1.3: The morphology density relation for ellipticals (*open circle*), S0 (*dots*), Spirals and Irregulars (*cross*) from low to high density environments going from left to right (Dressler, 1980).

1.5 Thesis Overview

The study of galaxy clusters is important for our understanding of the large-scale structure of the universe and for constraining cosmological parameters. They provide a unique laboratory to study the evolution of galaxies over a wide variety of environments where galaxies interact with the ICM and each other, ranging from within their dense cores, to their outskirts and the field. Moreover, observing galaxy clusters at high redshifts, provides a window into the state of these environments in the early universe, and the possible properties of protoclusters that evolve into the clusters in the local universe.

In this study, we examine the spectroscopically confirmed members of the galaxy cluster XLSSU J021744.1-034536 (XLSSC 122 onwards). XLSSC 122 is a mature galaxy cluster at redshift z=1.98, that was detected in the XMM-Newton Large Scale Structure survey (Pierre et al., 2004), from its extended X-ray emission, with subsequent Sunyaev-Zel'dovich detection along its line of sight (Mantz et al., 2014). These identifications make XLSSC 122 one of the few galaxy clusters with measurements of its intracluster medium at the highest redshift. In particular the cluster provides an exceptional site to study galaxy evolution with respect to their environment, around *cosmic noon*.

XLSSC 122 has a mass of $M_{500} = (6.3 \pm 1.5) \times 10^{13} M_{\odot}$, within a radius of $r_{500c} = 295 \pm 23$ kpc, corresponding to the region where the mean density of the cluster is 500 times the critical density c, of the universe at that redshift (Mantz et al., 2014, 2018). Subsequent studies of the cluster identify 37 galaxy members with spectroscopic redshifts, using Hubble Space Telescope Wide Field Camera 3 (HST WFC3) images in F105W and F140W bands and low-spectral-resolution slitless spectroscopy using G141 grism, following methods detailed in Willis et al. (2020). That study concluded from the presence of a prominent red-sequence, that the cluster is mature and that its members already have experienced their most active period of evolution prior to observation. Follow-up studies agree with this hypothesis, suggesting that the cluster members experienced accelerated size evolution at higher redshifts and that the period of star formation of the red population happened before the virialisation of the cluster on a short timescales (Noordeh et al., 2021; Trudeau et al., 2022).

In Chapter 2, we describe the data used to perform photometry, the methods of morphological analyses applied to classify the galaxy members of XLSSC 122 and discuss the implications of our results. In Chapter 3, we use data from large-scale structure simulations to deepen our understanding of the mass accretion history of galaxy clusters such as XLSSC 122. We finally summarise our findings and present the basis for future works in Chapter 4. Throughout this study, we adopt cosmology with $H_0 = 70$ km s^{-1}Mpc^{-1}, $\Omega_M = 0.3$, and $\Omega_\Lambda = 0.7$. Thus, the age of the universe is 3.26 Gyr at $z = 1.98$.

Chapter 2

HST Image Morphological Analysis of XLSSC 122

2.1 Hubble Space Telescope Images

XLSSC 122 is the most distant massive galaxy cluster identified via X-ray emission at $z \sim 2$. The cluster was discovered as an extended X-ray source in the XMM-Newton Large Scale Structure survey (XMM-LSS) and correlated with an overdensity of galaxies identified from the CFHTLS and Spitzer-SWIRE data, at a photometric redshift $z = 1.9 \pm 0.2$ (Willis et al., 2013). Mantz et al. (2014) confirmed a presence of the hot ICM, in addition to a SZ decrement and performed further studies of the cluster in deeper XMM-Newton observations that resulted in measurements of an average temperature of $kT = 5.0 \pm 0.7$ keV, a metallicity of $Z/Z_{\odot} = 0.33^{+0.29}_{-0.17}$ and a spectroscopically confirmed redshift $z = 1.99^{+0.07}_{-0.06}$, based on the *Fe* line emission in the X-ray spectrum (Mantz et al., 2018).

Subsequent deep imaging of XLSSC 122 by the HST WFC3 in F105W (9000-12000 Å) and F140W (12000-16000 Å) bands and slitless spectroscopy with G141 *grism*, were obtained between November 4^{th} 2017 and January 13^{th} 2018. The respective exposure times for F105W ,F140W and G141 were 2,612 s, 5,171 s and 26,541 s, respectively. F140W and F105W correspond to rest-frame wavelengths of $\sim$ 3000 Å and $\sim$ 5300 Å, respectively and therefore our observations span the 4000 Å break, and sample both young and more evolved stellar populations. Images in the F140W and F105W bands were reduced using *GRIZLI* (Brammer, 2019) and sources were detected by applying SExtractor (Bertin, E. & Arnouts, S., 1996) on the F140W

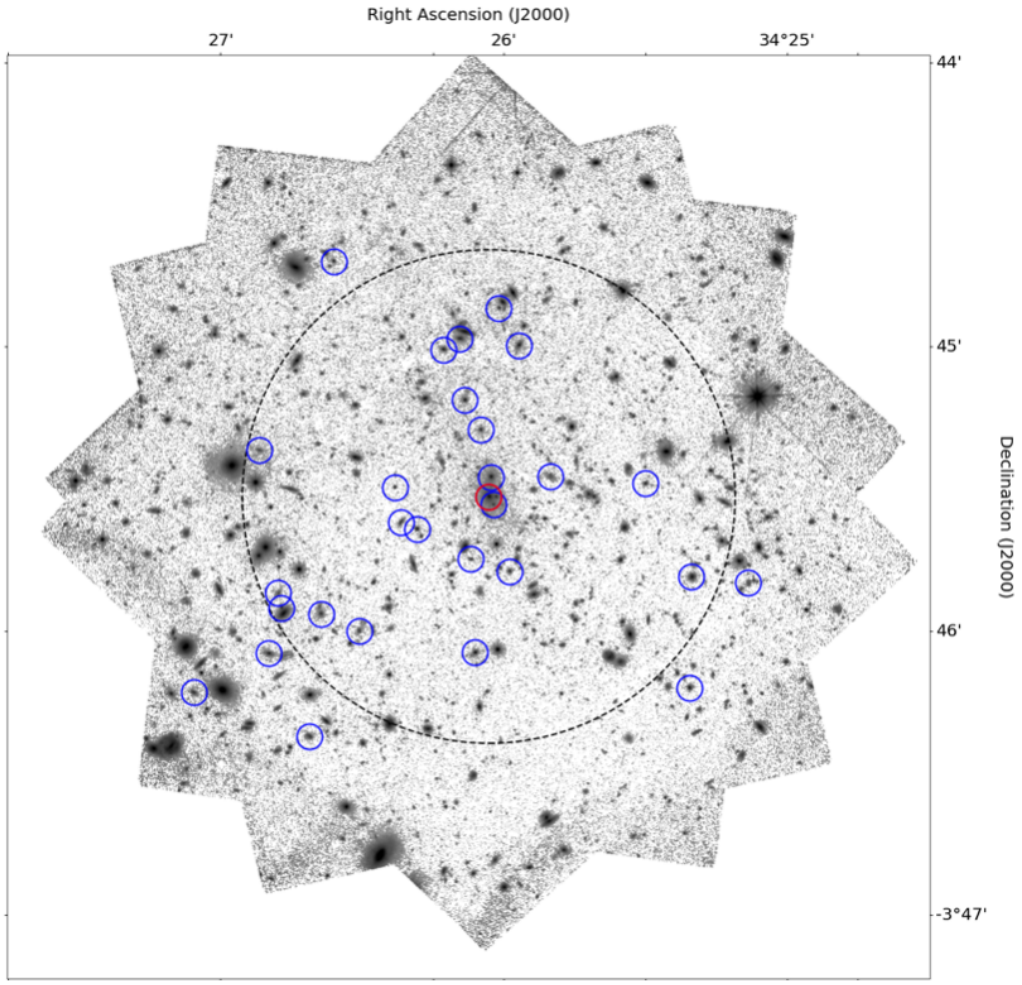

Figure 2.1: F140W image of the XLSSC 122 cluster. Blue circles mark the confirmed cluster members and the red circle shows the BCG. The dashed circle shows the r_{200c} of the cluster.

images (Willis et al., 2020). The segmentation map obtained from the processed F140W images is used to compute AB magnitudes in both bands, within an elliptical aperture based upon the Kron radius (Kron, 1980), with Kron factor, $k = 0.8$. Figure 2.1 shows the WFC3 F140W image of XLSSC 122 with the position of the brightest cluster galaxy (BCG) and the virial radius of the cluster $r_{200c} = 443 \pm 35$ kpc indicated.

Spectroscopy was performed by building full field spectral contamination models on the G141 images for sources matching the F140W segmentation map. Robust contamination models were obtained by splitting the G141 observations into four orientations and two-dimensional spectra for each source were extracted. A probability distribution function, PDF for the redshift of each source was derived by fitting the

spectra to a suite of galaxy templates with $0.2 < z < 4$. The best fitting models were selected on using a minimum χ^2 test.

The integral of the redshift PDF within $1.96 < z < 2.00$, P_{mem} was used to confirm cluster membership for the sources from the F140W image. Those galaxies with $P_{mem} > 0.5$ and $F140W_{kron} < 24$ were defined as 'gold' members, resulting in a sample of 29 spectroscopically confirmed XLSSC 122 members. This sample of galaxies, with cutouts in F140W band shown in Figure 2.2, represents the primary dataset used in this thesis.

Figure 2.3 shows the cluster members separated into two populations based on the bimodal distribution of their F105W-F140W colour into Red-Sequence and Blue-Cloud galaxies. These observations suggest that XLSSC 122 is a mature cluster with a well-defined sample of members with evolved stellar populations (Willis et al., 2020).

2.1.1 HST Image Visual Inspections

We visually inspect each of the F140W images of the 29 XLSSC 122 members (Fig.2.2). After examining the shape of the cluster members together with their isophotes, we find ten members (ID 146, 240, 434, 454, 455, 554, 604, 726, 808 and 1065) with structures that may indicate recent galaxy interactions (Fig.2.4).

ID 434, 454, and 726 show the greatest disturbance in their structures and highly asymmetric shapes. The brightest pixels of ID 146, 554, and 1065 appear to be off-center, and their contour maps trace 'tail-like' structures. ID 240, 604 and 808 show the presence of double-nuclei. Finally, ID 455 is generally smooth, but its contour map reveals a 'tail-like' structure.

The morphologies of these ten galaxies are quantified and further discussed through-

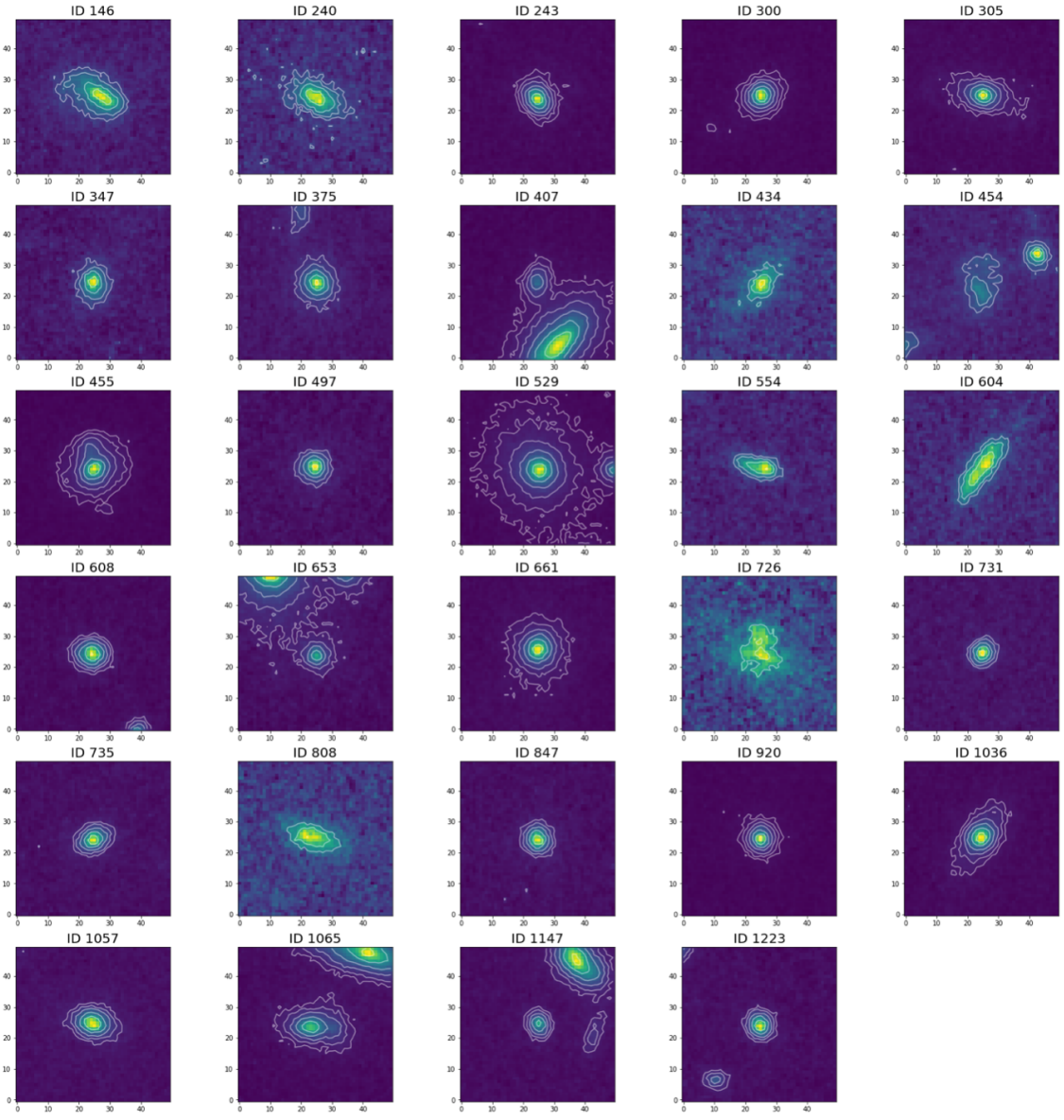

Figure 2.2: HST F140W image cutouts of the 29 'gold' cluster members with isophotes overplotted. The BCG is shown with ID 529.

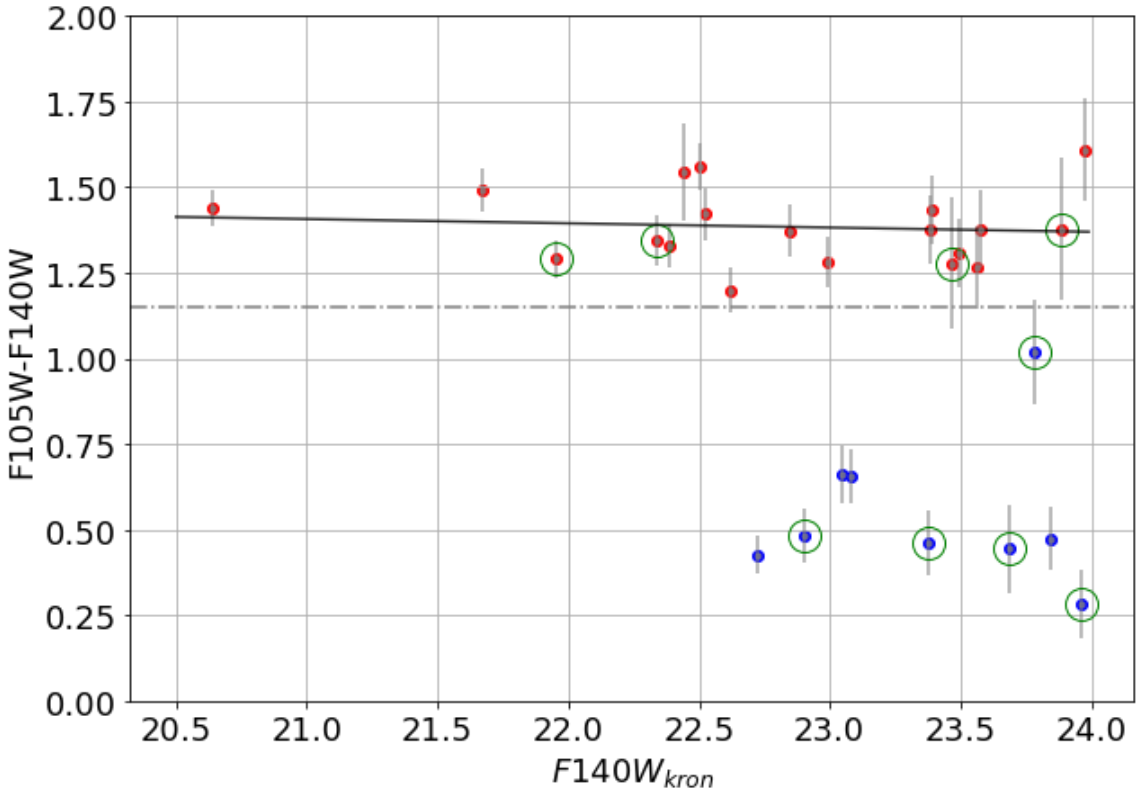

Figure 2.3: Colour-Magnitude Diagram (F105W-F140W vs $F140W_{kron}$) of the XLSSC 122 cluster members. Green circles shows the visually disturbed members (Fig.2.4). The black line shows the least square fit to the distribution of the red sample. The grey dot-dashed line shows the lower colour limit (F105W-F140W = 1.15) to be considered a red-sequence galaxy. A reiteration of Fig. 3 from Willis et al. (2020)

out this study.

2.2 Additional Data

In addition to the HST images of the cluster, we use measurements from previous related studies. In doing so, we aim to expand our understanding on the processes affecting the morphology of XLSSC 122 members and to investigate their juxtaposition against other galaxy populations.

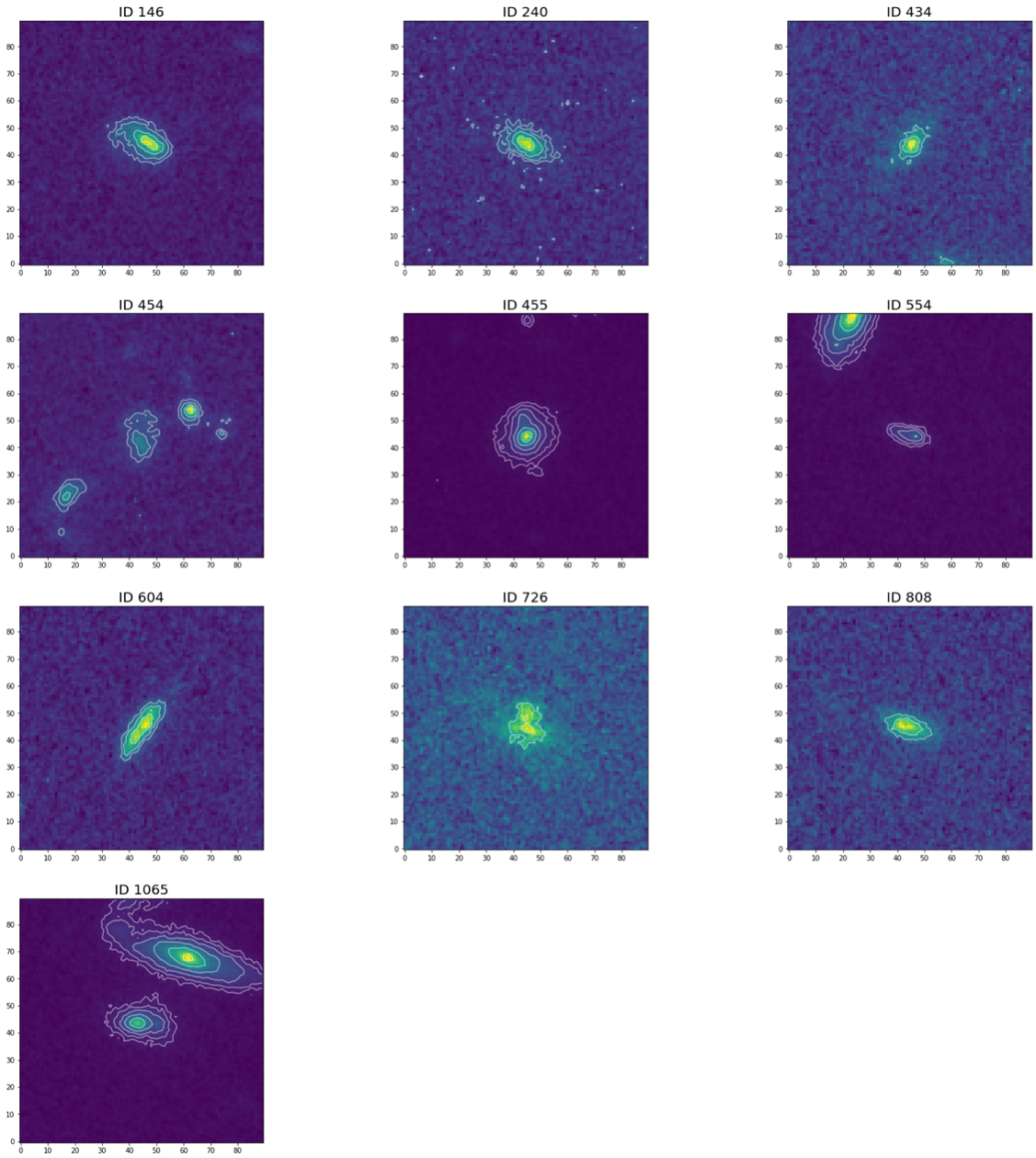

Figure 2.4: F140W images with isophotes of the 10 cluster members showing disturbed structures.

2.2.1 Sérsic Index Measurements

Noordeh et al. (2021) performed a preliminary morphological analysis of the spectroscopically confirmed XLSSC members from the same HST images described in Section 2.1, as part of an investigation into the mass-size relation of high redshift galaxies.

They measured the surface brightness of the cluster members by fitting the light distributions in F140W band to a single component, two-dimensional Sérsic profile using GALFIT (Peng et al., 2002), defined by the exponent n, in Equation 2.1. They defined bulge-dominated members as those having Sérsic indices > 2 and found that 78% of the cluster's red-sequence galaxies are bulge-like, on the basis of this criteria. No significant correlations between the galaxies' sizes, masses and morphologies, however were found.

We use their Sérsic index measurements to supplement the morphological measurements presented in this thesis to expand our understanding of the structure of the XLSSC 122 members.

$$I(r) = I(r_e)exp\left\{-\kappa\left[\left(\frac{r}{r_e}\right)^{1/n} - 1\right]\right\}, \tag{2.1}$$

2.2.2 Mass and Age Measurements

Trudeau et al. (2022) analysed the mass accretion history of XLSSC 122. In their study, they performed fittings on multiband photometry of the spectroscopically confirmed cluster members, using the python package Bayesian Analysis of Galaxies for Physical Inference and Parameter EStimation (BAGPIPES) version 0.8.4 (Carnall et al., 2018), that generates SED models of their stellar populations. Hence, they measured the age of the oldest stars, the characteristic time, the dust extinction, the metallicity and total stellar mass.

Trudeau et al. (2022) classified the members into 4 different groups: very old, old, young and star forming. They found that the red-sequence galaxies show a variety of ages, yet all with short characteristic time, expressing a short duration of star formation in this subset of member galaxies.

We use their resulting values of median age and stellar mass measured from the full probability distributions of the star formation history parameters generated from the SED fitting of the XLSSC 122 members.

2.2.3 Field Galaxy Sample

Similarly to the the study done by Noordeh et al. (2021), we build a sample of 531 field galaxies using images in the F140W and F814W (7000-10000 Å) bands from the CANDELS/3D-HST survey, more specifically from AEGIS, COSMOS, GOODS-S,

GOODS-S and UDS (Momcheva et al., 2016; Brammer et al., 2012; Skelton et al., 2014). We select sources with spectroscopic redshifts in the range $1.9 < z < 2.1$ and with $F140W < 24$ to match the members of XLSSC 122. The location of these galaxies in the respective field surveys are shown in Figure 2.5.

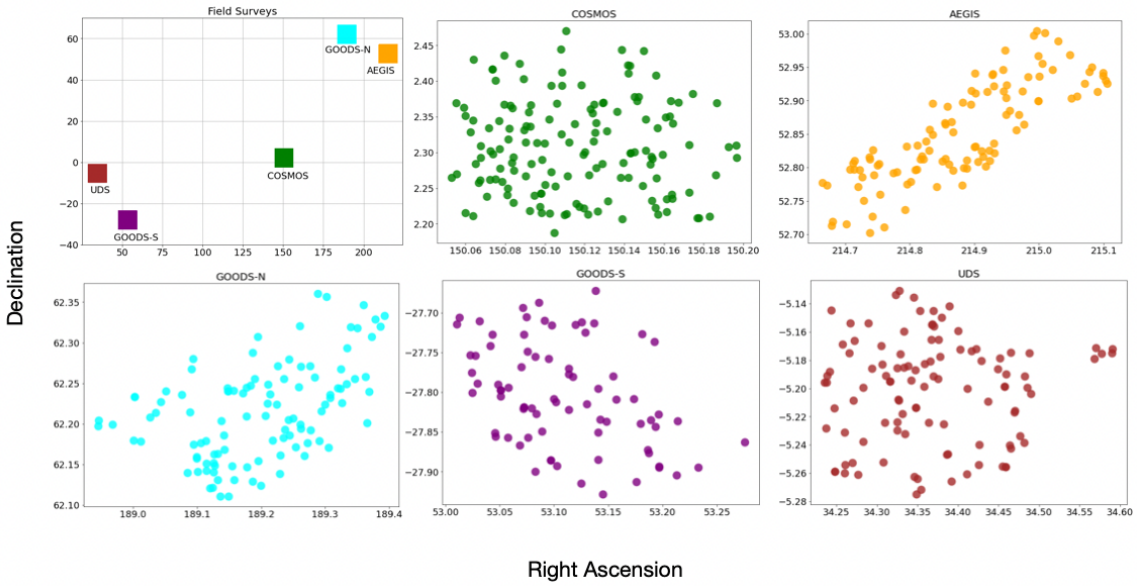

Figure 2.5: Position of the Field surveys and the selected field galaxies within them at $z = 2$.

In Section 2.4.4, we describe the morphological analysis of the field sample and compare their measurements to those of the XLSSC 122 galaxies.

2.2.4 High Redshift Galaxy Clusters at $1.2 < z < 1.8$

Sazonova et al. (2020) explored the morphology-density relationship within high redshift galaxy clusters. They performed morphological measurements from the HST WFC3 images in the F140W and F160W bands of four galaxy clusters at redshifts 1.19, 1.40, 1.49 and 1.75. The sample of galaxy members within these clusters is referred to as S20 hereafter, which provide a sensible sample of high redshift cluster members to compare with the XLSSC 122 members, given similar data and analysis methods. The one important difference is that our study uses spectroscopic data to identify cluster members, whereas the S20 sample was built using a mixture of spectroscopic and photometric methods, with a heavy reliance on methods such as the red-sequence identification method. Sazonova et al. (2020) used Statmorph (Section 2.3.1) to perform photometry on the four clusters to measure the morphological indices defined in Section 2.3.2 below. They concluded that the morphology-density relationship observed in the local universe exists as far back as $z = 1.75$, suggesting that bulge-dominated galaxies (early-type galaxies) were already established this early in the history of the universe.

In Section 2.4.4, we compare the morphological measurements of the XLSSC 122 to those of the four high redshift galaxy clusters in S20.

2.3 Methods

2.3.1 STATMORPH

The non-parametric morphological measurements used in this study are calculated using the Python package, Statmorph (Rodriguez-Gomez et al., 2019). It is a publicly available code that follows the methods and definitions described in (Lotz et al., 2004, 2008b). Measurements can be made on images containing a single or multiple detection sources. In this study, we run the algorithm on individual cutouts of each XLSSC 122 members, as opposed to the whole image of the cluster.

The Statmorph code requires the following input data:

- an image containing the object of interest given as a 2D array. We run the code

separately for each cluster member by providing the cutouts as shown in Fig. 2.2.

- a segmentation map describing the object pixels in the image, given as a 2D array of the same size as the image. We provide the segmentation map generated within SExtractor to detect the sources from the HST image (Section2.1).
- the weight map representing the 1σ variation of each pixel value in the image data product from *grizli*.
- a segmentation map representing pixels to be masked and excluded in the calculation. We masked the pixels marking the position of foreground stars, which resulted in the masking of only one object from the image.

2.3.2 Morphological Indices

Concentration

The concentration C, is defined as the ratio of the radii defining the 80th and 20th isophotes of a source (Kent, 1985):

$$C = 5 \log_{10} \left(\frac{r_{80}}{r_{20}} \right), \tag{2.2}$$

Elliptical galaxies, which are more bulge-dominated systems, have higher values of C, signifying that its light is concentrated in the center (Conselice, 2003). Similarly to the Sérsic index defined in Eq.2.1 (Sérsic, 1963), C tends to decrease for later Hubble type (disky) galaxies (Bershady et al., 2000).

Asymmetry

The asymmetry A, is a parameter defined to quantify the morphology of galaxies, especially at high redshifts (Lilly et al., 1995; Brinchmann et al., 1998). This method was shown to be effective in detecting features producing asymmetric light distribution, such as star formation, galaxy interactions, mergers or dust lanes (Conselice et al., 2000a):

$$A = \frac{\sum_{i,j} |I_{i,j} - I^{180}_{i,j}|}{\sum_{i,j} |I_{i,j}|} - A_{bgr}, \tag{2.3}$$

where, $I_{i,j}$ and $I_{i,j}^{180}$ are the flux within each pixel of the original image and 180° rotated image, respectively. A_{bgr} is the average asymmetry of the background.

A galaxy's asymmetry value is calculated by rotating the galaxy image by 180° about the center of the object of interest and subtracting the resulting light distribution from the original image, as shown in Eq.2.3 (Conselice et al., 2000a). Bulge-dominated galaxies have very low asymmetry values (A $\sim$ 0.02), while spirals have intermediate asymmetry values (0.07 < A < 0.2) and merging galaxies can have very large asymmetry values (A $\sim$ 0.32).

Gini Index

The Gini index G, was originally introduced in economics (Gini, 2005), where it is used to measure the distribution of wealth in a society. In astronomy, we use it to measure the distribution of light among the galaxy pixels. To calculate G, all a galaxy's pixels are ranked from brightest to dimmest and Gini is defined as (Abraham et al., 2003):

$$G = \frac{1}{\bar{X}n(n-1)} \sum_{n=1}^{n} (2i - n - 1)X_i, \tag{2.4}$$

where $\bar{X}$ is the mean over the pixel values. However, Lotz et al. (2004) demonstrated that the traditional definition of the Gini index as shown in Equation 2.4, becomes less accurate for images with lower SNR, due to the increasing number of pixels with flux values below the mean sky level. They altered the calculation for the Gini index as shown in Equation 2.5, where G is calculated for the absolute values of the pixel values, which thus makes the comparison of Gini indices for galaxies at high-redshift comparable to local galaxies.

$$G = \frac{1}{|\bar{X}|n(n-1)} \sum_{n=1}^{n} (2i - n - 1)|X_i|, \tag{2.5}$$

where $|\bar{X}|$ is the mean of the absolute values $|X_i|$. A Gini index of 1 means that all the galaxy light are concentrated in one pixel, while a Gini index of zero means that the total galaxy flux is evenly distributed among all of the pixels belonging to the galaxy. Highly concentrated early-type galaxies have higher Gini values while diffuse galaxies with extended regions and weak bulges have low Gini values.

Similar to C, Gini measures the compactness of light of the galaxies, but it is

independent of the position of the brightest region and does not require it to be in the central region. Therefore, the Gini index is more sensitive to galaxy mergers and double nuclei. Additionally, as shown by Lotz et al. (2004), it is less dependent on limiting flux and the signal-to-noise ration (SNR) of the image, unlike concentration, which makes it useful for high redshift analyses.

$\mathbf{M_{20}}$

M_{20} was first introduced by Lotz et al. (2004) and it is the measure of the second moment (i.e. variance) of the spatial distribution of the highest 20% of the galaxy light. It is calculated by ranking each of the galaxy pixels according to flux and the spread of the brightest 20% of the pixels is calculated using the following:

$$\mu_{tot} = \sum_{i=1}^{n} \mu_i \equiv \sum_{i=1}^{n} I_i[(x_i - x_c)^2) + (y_i - y_c)], \tag{2.6}$$

$$M_{20} = \log_{10}\left(\frac{\sum_i \mu_i}{\mu_{tot}}\right), while \sum_i I_i < 0.2 I_{tot}, \tag{2.7}$$

where μ_{tot} is the total second-order central moment, I_{tot} is the total flux of the pixels for the galaxy. A low (more negative) M_{20} value signifies that the brightest pixels are concentrated in the central region and may correspond to spheroidal galaxies. A high M_{20} (less negative) implies that the brightest pixels are offset from the center and may correspond to bright star forming regions in disky galaxies, or merger features. M_{20} is expected to correlate with C, according to their similar definition. However, similarly to Gini, M_{20} weakly depends on limiting flux and SNR, as expressed in Lotz et al. (2004).

Concentration-Asymmetry Diagram

Concentration and asymmetry measurements are part of a set of widely used non-parametric morphological analysis tools, known as CAS (Concentration, Asymmetry and Smoothness) statistics (Conselice, 2003).

Smoothness S, describes the patchiness or clumpiness of a galaxy's light distribution. It is defined as the summation of the residuals resulting from subtracting the flux within pixels of a smoothed image from the original image (Conselice, 2003). Ellipticals in general do not have high-spatial frequency power in their structures and therefore have a smoothness value of around 0. On the other hand, galaxies that

are undergoing star formation contain large amounts of clumpy regions and have larger S values. In this study, we do not consider the measurements of smoothness for the cluster members, as they do not provide additional useful information and the measurements appear to be less effective for high redshift objects with lower SNR (Appendix A.1).

The relationship between concentration and asymmetry is one that is used in the classification of galaxies based on their morphologies to separate populations with disturbed structures from those that are more relaxed (Conselice, 2014). We use this method to determine whether XLSSC 122 cluster members show more bulge-dominated morphologies or features showing merger interactions.

Gini-M_{20} Diagram

Even if the C-A analysis is more straight forward, it is not without shortcomings. For instance, the concentration, based on its definition, assumes a predefined center for the circular apertures used and therefore implicitly assumes circular symmetry, which makes it inefficient in describing irregulars. Lotz et al. (2004) explored multiple ways to combine the aforementioned non-parametric methods to better classify galaxy morphology and detect possible mergers. For instance, they compared the morphological parameters of known 'normal' galaxies (E-Sd galaxies) to those of ultra-luminous infrared galaxies (ULIRGs). ULIRGs often show morphological features of on-going or recent mergers, multiple nuclei and tidal features, resulting in high asymmetry values. They found that multi-nucleus galaxies show larger differences in their Gini index values (larger Gini index values) relative to 'normal' galaxies than seen when their concentrations are compared. Additionally, in identifying single-nucleus galaxies, M_{20} is more robust than asymmetry especially at lower SNR. When plotting Gini against M_{20}, they find that ULIRGs are separated above 'normal' galaxies on the diagram. The combination of Gini and M_{20} is more sensitive to mergers with baryonic mass ratios between 1:1 and 9:1, while asymmetry becomes less efficient in finding minor mergers with baryonic mass ratios greater than 4:1 (Lotz et al., 2004).

Lotz et al. (2008b) described regions on the Gini-M_{20} diagram that can be used to separate galaxies into disky, bulge-dominated galaxies and possible mergers, based on the location of visually classified galaxies at $0.2 < z < 0.4$. The disky region is populated by a combination of spirals and irregular galaxies, while the bulge-dominated region contains ellipticals and spheroids. The region separating mergers

is based on the location of ULIRGs showing visual characteristics of merger activity. The regions on the diagram are defined as follows:

$$\text{Mergers} : G > -0.14M_{20} + 0.33$$
$$\text{Bulge-Dominated} : G \leq -0.14M_{20} + 0.33 \text{ and } G > 0.14M_{20} + 0.80$$
$$\text{Disky/Irr} : G \leq -0.14M_{20} + 0.33 \text{ and } G \leq 0.14M_{20} + 0.80$$

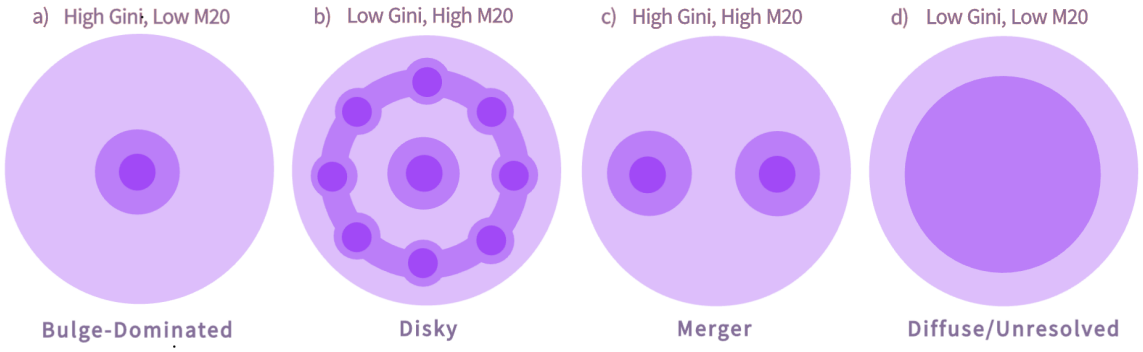

Figure 2.6: Diagram representing simplified examples of the light distribution of galaxies resulting in different Gini and M_{20} values for the types described in the text.

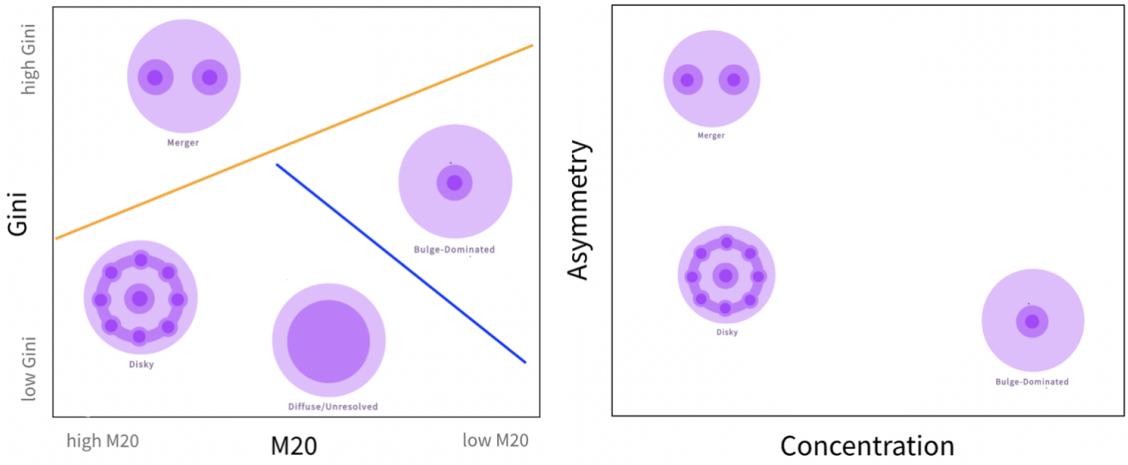

Figure 2.7: Diagram representing simplified examples of the general positions of galaxy types described in Fig.2.6 on the Gini-M_{20} plot (*left panel*) and on the C-A plot (*right panel*). The orange and blue lines are the boundaries described in Equ.2.3.2.

We present in Figure 2.6 a sketch of the light distributions corresponding to different Gini and M_{20} measurements for the galaxy types defined above. Bulge-dominated galaxies have high Gini and low M_{20} values signifying that light is concentrated within a few pixels in their galactic centers (Fig.2.6a). A high Gini and high M_{20} describes galaxies with their light concentrated in a few bright spots and off-center, which may correspond to star-forming arms in their disks (Fig.2.6b). For galaxies classified as mergers, a high Gini value corresponds to the presence of light concentrated in clumps, and a high M_{20} indicates the clumps are offset from the center (Fig.2.6c). This situation may represent features such as double nuclei of a merger remnant. In Figure 2.7 we show the general positions of galaxies with morphologies described in Figure 2.6 on the Gini-M_{20} and C-A plots.

The positions of galaxies on Gini-M_{20} plot has shown to be effective in detecting minor and major mergers in their early stages of the merger compared to other previous methods which are better at detecting mergers in their later stages (Lotz et al., 2010).

2.3.3 Environment

The relationship between galaxy properties (such as their morphology, star formation rates, luminosity, colour, etc.) and their surrounding environment has been the subject of many studies in the past decade. Previous measurements of environmental dependence of the physics of galaxy formation have shown that early-type galaxies tend to be in more clustered regions while blue star-forming galaxies are found in less clustered regions (Norberg et al., 2002; Ellison et al., 2009; Webb et al., 2013). This observational feature, known as the morphology-density relation, states that in the local Universe, the fraction of elliptical galaxies and spheroids compared to disky galaxies is higher in denser regions (Dressler, 1980).

There is extensive debate about whether dense environments contribute to suppressing the star formation activity in galaxies (Tran et al., 2010; Quadri et al., 2012). Since star formation is one of the main processes that alter galaxy morphology, quantifying the surface density within galaxy clusters at high-redshift may give significant insight on the environmental processes that contribute to the transformation of galaxies. Many studies show that galaxy clusters at $z \sim 1.5$ are already populated by red galaxies (Kurk et al., 2009; Wilson et al., 2009; Strazzullo et al., 2010). Therefore, observations of clusters at even higher redshift might provide an opportunity to identify

the processes that established the dominant red galaxy population we observe in the local Universe.

The environment in which galaxies form and evolve imprints itself on the properties of the galaxies which end up in clusters. Galaxies are theorised to start in low-density regions of the universe, such as voids or filaments and then migrate down the potential well into dense groups (Hatch et al., 2016). Mapping the surface density distribution of galaxy clusters, therefore may give clues about the protoclusters from which they originate.

To measure the local surface density, two main methods can be used: 1) by considering a specific number of nearest neighbours to find the underlying density fields and 2) by finding the number of galaxies in a fixed aperture around the target galaxy (Muldrew et al., 2012). The first method is independent of the dark matter halo mass, while the aperture-based method identifies the high density region corresponding to high mass haloes. For this thesis, we use the first method to find the local density within an aperture radius corresponding to the distance to the 5^{th} neighbour, r_{5nn}.

To calculate the local surface density ρ_{5nn}, within the radius to the fifth nearest neighbour, r_{5nn}, on the plane of the sky around each cluster member, we apply the following equation:

$$\rho_{5nn} = \frac{5}{\pi r_{5nn}^2} \tag{2.8}$$

We represent the overdensity δ in the following equation, as a ratio of ρ_{5nn} to the average surface density of the whole cluster, ρ_{avg}. The latter is calculated using the quotient of the total number of cluster members and the area of the cluster within the cluster's r_{200c} radius.

$$\delta = \frac{\rho_{5nn}}{\rho_{avg}} - 1 \tag{2.9}$$

We also consider an alternative definition for the local density as described by Cowan & Ivezić (2008), where it is calculated using the cumulative distances to the n nearest neighbours. Therefore, considering the sum of the distances to the five nearest neighbouring cluster members, Equation 2.8 becomes:

$$\phi_5 = \frac{1}{\rho_{avg} \sum_{i=1}^{5} r_i^2} \tag{2.10}$$

Considering the distances to all five neighbours, compared to only the distance

to the 5^{th} neighbour has shown to provide a more robust measure, as this method minimises distortions caused by interlopers (Hatch et al., 2016; Ivezić et al., 2005).

2.4 Results

In the following section, we discuss our observations based on the morphological measurements performed on the HST images of the XLSSC 122 cluster. We compare the morphologies of its galaxies to their internal properties, as well as to the morphologies of other galaxy samples. Table 2.1 shows all the measurements made for the 29 cluster members.

2.4.1 Morphology

Gini-M_{20}

We present the measurements of Gini and M_{20} for the XLSSC 122 members in Figure 2.8, showing the relationship between the two morphological indices. The cluster members are separated into 3 main types: *disky*, *bulge-dominated* or *merger*, based on their position on the Gini-M_{20} plot as described in Section 2.3.2. The blue population of galaxies are all classified as having disky structures. The red-sequence galaxies have higher bulge-strength, represented by larger Gini and lower M20 values. This finding is consistent with the observations made by Lotz et al. (2008b), whereby 75% of their bulge-dominated sample lie on the red-sequence. Four XLSSC 122 members, ID 305, 529, 653 and 1036 (Fig.2.4), are within the bulge-dominated region of the plot. ID 661 is classified as being a possible merger, being located in the plot above the boundary defined by Lotz et al. (2008b). The measurements for this particular galaxy, however, may be impacted by it being one of the closest neighbours to the BCG, and the light within the segmentation map corresponding to this source may be contaminated by light from both the BCG and ICM. As shown in the photometry obtained with Statmorph shown in Figure A.2 (Appendix A.2), the light distribution of ID 661 results in measurements corresponding to a more disturbed light distribution than expected.

The ten visually disturbed members (Fig.2.4) are all located in the region of the Gini-M20 plot belonging to disky galaxies. This region is also populated by red galaxies. As observed by Lotz et al. (2008b), red galaxies classified as disky or irregulars by the Gini-M_{20} plot may be disks reddened by dust. For instance, ID 726

Table 2.1: Table with measurements from the HST images of the XLSCC 122 cluster members.

ID	$F140W_{kron}$	$F105W_{kron}$	Gini	M20	Sersic Index	C	A	$log(M/M_{\odot})$	Age (Gyr)	Age Group
BCG	20.6356	22.0918	0.588	-1.884	7.56	3.797	0.037	11.462	2.237	very old
146**	22.9016	23.446	0.471	-1.343	0.9	2.517	0.163	9.808	0.0280	star forming
240*	23.0151	99.0	0.544	-1.725		2.994	0.065			
243	22.6169	23.7783	0.505	-1.763	2.17	2.731	0.033	10.688	0.963	old
300	22.5026	24.085	0.526	-1.72		2.763	0.03			
305	22.5249	23.8277	0.6	-2.082	7.3	3.524	0.025	10.827	0.931	old
347	23.5611	24.8274	0.511	-1.77	2.06	2.788	0.034	10.355	1.622	old
375	23.0819	23.5689	0.531	-1.862	2.89	3.087	0.009			
407	23.0458	23.5492	0.441	-1.68	2.75	2.484	0.061			
434*	23.8874	25.0249	0.497	-1.822	2.61	2.974	0.018			
454**	23.6887	24.0581	0.386	-1.304	0.45	2.187	0.098	9.807	0.604	star forming
455**	21.9504	23.1633	0.506	-1.818	2.94	2.991	0.156	11.145	1.287	very old
497	23.5789	24.9355	0.489	-1.677	2.44	2.739	0.028	10.794	2.213	very old
554**	23.9599	24.2755	0.449	-1.194	0.36	2.29	0.116	9.361	0.139	star forming
604*	23.375	23.9281	0.43	-1.33	0.37	2.436	0.007	9.863	0.337	star forming
608	22.991	24.2768	0.466	-1.613	1.21	2.471	0.039	11.026	2.312	very old
653	22.4436	23.9066	0.54	-1.895	4.15	3.596	0.06			
661	21.6681	23.1297	0.626	-1.859	3.07	4.616	0.033	11.291	2.331	very old
726*	23.4635	24.8816	0.485	-1.579	1	2.572	0.029			dusty*
731	23.9736	25.4998	0.452	-1.671	1.93	2.506	0.004	10.769	2.303	very old
735	23.3896	24.8732	0.495	-1.72	2.6	2.7	0.02			
808**	23.7828	24.9066	0.473	-1.519	0.75	2.841	0.111	9.905	0.630	young
847	23.3821	24.7253	0.498	-1.635	1.94	2.689	0.027	10.704	2.470	very old
920	22.7254	23.2372	0.495	-1.758	6.39	2.81	0.051	10.129	0.147	star forming
1036	22.3846	23.7272	0.542	-1.881	5.03	3.209	0.029	10.984	1.644	old
1057	22.8479	24.1777	0.496	-1.685	1.63	2.667	0.044	10.983	1.676	old
1065**	22.3414	23.6267	0.547	-1.645	0.94	2.979	0.151			
1147	23.8472	24.2785	0.467	-1.617	0.86	2.563	0.042			
1223	23.4942	24.8741	0.471	-1.657	2.19	2.533	0.043	10.308	0.680	young

* Visually disturbed members

** Visually disturbed members and classified as Mergers using C-A.

underlined: bulge-dominated classified using C-A.

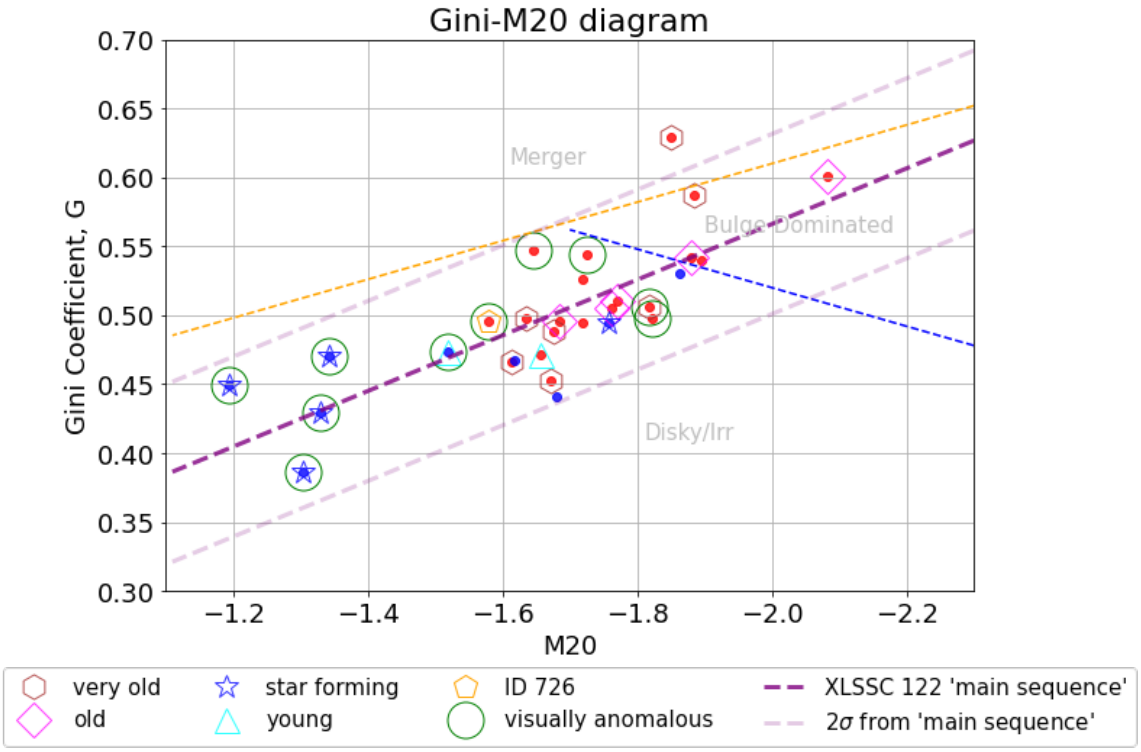

Figure 2.8: Gini-M_{20} plot with symbols representing age groups defined by Trudeau et al. (2022) and the 10 members with visually disturbed features (Fig.2.4). The points are shown in red and blue dependent on the respective galaxy's position on the CMD. The blue and orange boundaries are defined by Lotz et al. (2008b) to separate disky, bulge-dominated, and merger galaxies. The purple dashed line is the 'main sequence' of the Gini-M_{20} distribution of XLSSC 122 members and the pale purple dashed line shows the 2σ deviation from the 'main sequence'.

is a red-sequence galaxy in the Disky/Irr region that also shows high dust-extinction (Trudeau et al., 2022).

We also represent in Figure 2.8 the age groups described in Section 2.2.2, as defined by Trudeau et al. (2022) for the XLSSC 122 members. The star-forming and young galaxies of the cluster are all classified as disky or irregular systems, while the older members are among the red-sequence galaxies that are more bulge dominated. ID 1223, which is a young red-sequence member, is an exception, suggesting that it is another example of a disky or irregular galaxy reddened by dust.

We define a Gini-M_{20} 'main sequence' as the linear fit to the distribution of the XLSSC 122 members on the plot (Eq.2.11). A band covering a deviation of 2σ from the 'main sequence', closely matches the boundary defined by Lotz et al. (2008b) to identify mergers. Following the axis moving along the 'main sequence' from left

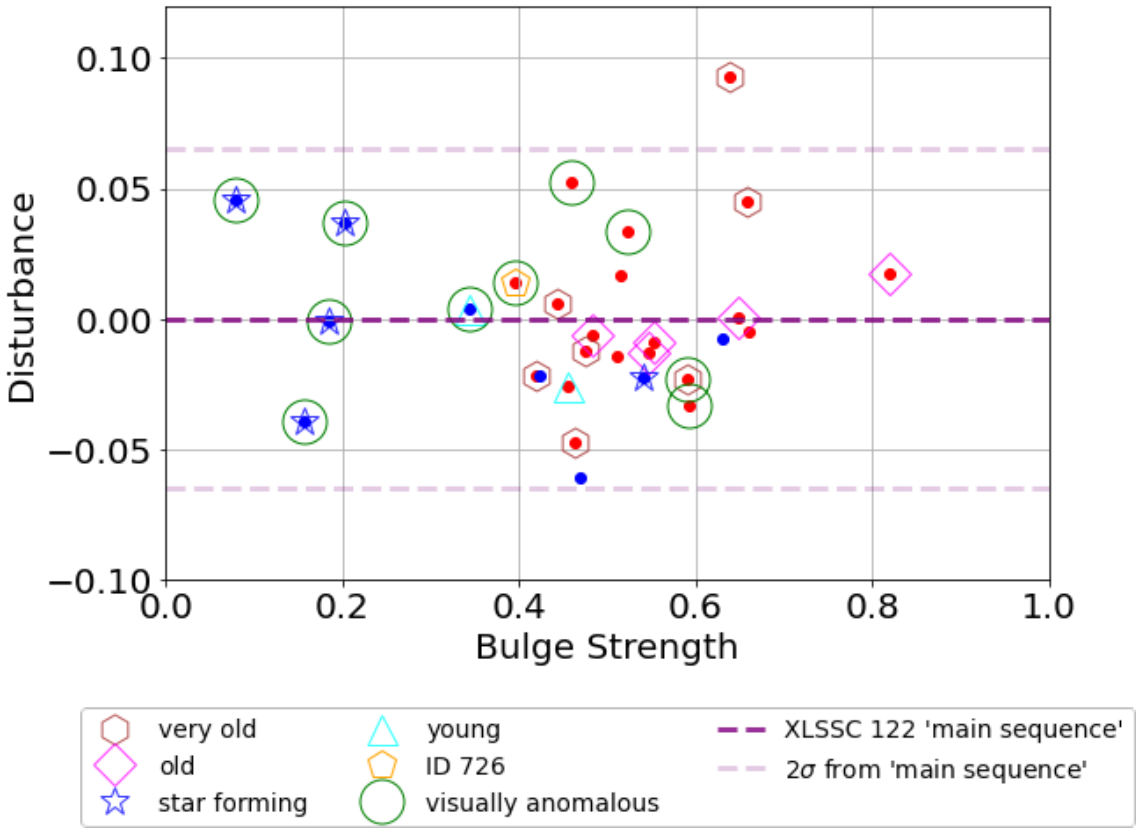

Figure 2.9: Bulge-strength vs Disturbance. Symbols are the same as in Fig. 2.8.

to right, represents an increase in the degree of bulge dominance. We define the normalised distance of the projected position of the cluster members along the 'main sequence' as the *Bulge-strength*, and the positive divergence from the 'main sequence' as a measure of *Disturbance* in the galaxies' structure (Fig. 2.9). Negative disturbance values is however not considered as an indication of disturbed structures.

$$\text{XLSSC 122 Gini-}M_{20}\text{ 'main sequence': } G = -0.20M_{20} + 0.16 \tag{2.11}$$

Figure 2.9 reveals a trend between the bulge-strength and the age groups and colour of the cluster members. This trend is also observed in field and low redshift galaxies, whereby bulge-dominated systems are more likely to be older and redder (Kauffmann et al., 2004). 7 out of the 10 visually disturbed galaxies are found above the 'main sequence', with positive disturbance values.

In the first panel of Figure 2.10, we compare the bulge-strengths to the colours of the cluster members, and observe that the higher the bulge-strength, the redder the

galaxy tends to be. In the second panel, we see that the bulge-strengths are clearly related to the M_{20} values.

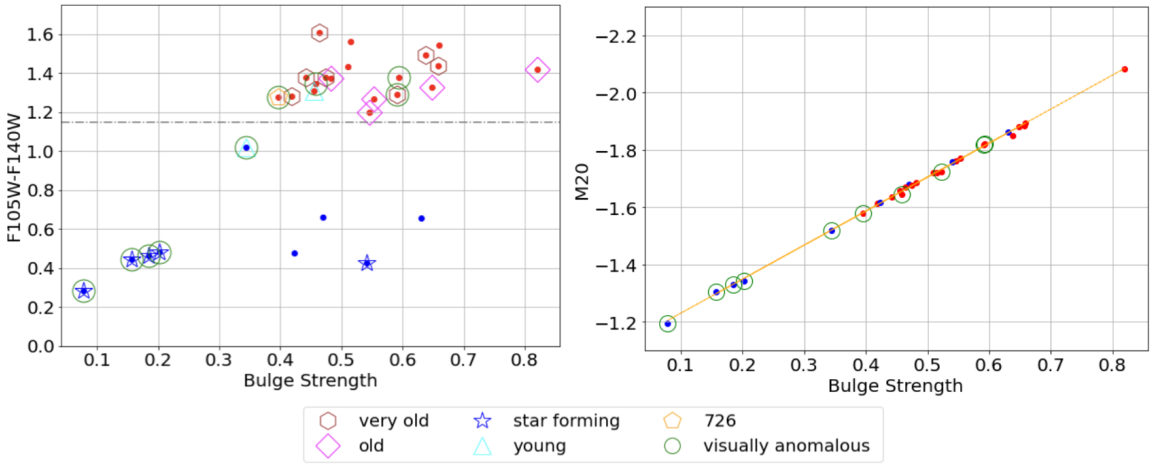

Figure 2.10: *Left panel:* Bulge-strength vs Colour. *Right panel:* Bulge-strength vs M_{20}. Symbols are the same as in Fig. 2.8.

Concentration-Asymmetry

Using the alternative method to classify galaxies quantitatively based on their morphology as described in Section 2.3.2, we show the relationship between the concentration C and the asymmetry A in Figure 2.11. The bimodal distribution of the XLSSC 122 members on the plot separates members with different properties. Red and old galaxies have higher concentrations and lower asymmetries, while those with visually disturbed morphologies have larger asymmetries. We first define regions on the plot based on the positions of the bulge-dominated galaxies classified using Gini-M_{20} plot earlier. Thus, the bulge-dominated galaxies classified using the C-A plot are those with concentration, C$>$ 3.1.

The red and old XLSSC 122 members have in general lower asymmetries, except for two red-sequence galaxies (ID 455 and 1065) which have high asymmetries and are among the visually disturbed subset. As seen in Figure 2.4, these galaxies show very slightly disturbed structures resembling small extended features from their centers, such as streams or tails. The asymmetry measurement captures their appearance effectively and may suggest that these two cluster members have been reddened by dust. In the C-A plot (Fig.2.11), ID 661 is in the region corresponding to bulge dominated systems, with low asymmetry and high concentration values. The C-A

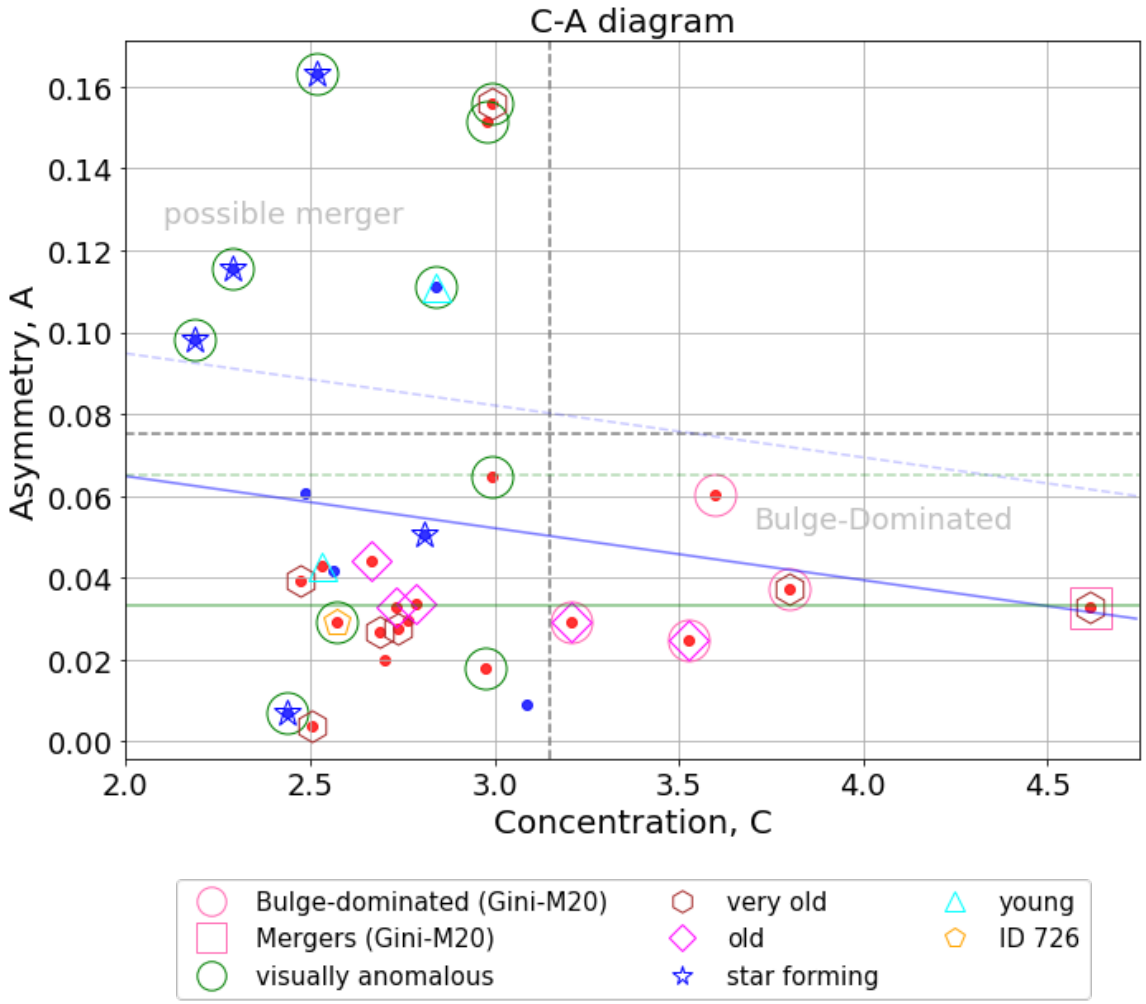

Figure 2.11: Plot of Concentration versus Asymmetry with measurements for cluster members. The points are shown in red and blue dependent on their position on the CMD. The symbols represent the age classification (Trudeau et al. (2022) and the morphological classification based on the Gini-M20 plot. The blue line shows the linear fit to the XLSSC 122 member C-A distribution and the dashed blue line shows the 1σ deviation from the linear fit. The grey vertical and horizontal lines represent suggested boundaries for an alternative way to classify cluster members based on morphology. The green solid and dashed lines, show the mean asymmetry for the low A population and the 2σ deviation from the mean, respectively.

relationship appears to be less sensitive to potential contamination from the BCG and ICM on the light distribution of this galaxy.

The blue and young population of the XLSSC 122 members all exhibit low concentrations and a range of asymmetries. Of those galaxies, the ones with asymmetry values larger than a σ deviation from the linear fit to the C-A distribution of the

cluster members are identified as galaxies having experienced recent or on-going interactions. The possible mergers identified using the C-A plot are ID 146, 454, 455, 554, 808 and 1065, which also show visual morphological disturbance. Since the C-A method is effective at recovering the bulge-dominated members and the visually selected ones, we represent going forward these populations as those classified using this method.

Colour-Morphology Relationship

We further explore the relationship between the colour of the XLSSC 122 members and their quantitative morphological measurements. The top left panel of Figure 2.12 shows the colour-magnitude diagram (similarly to Fig.2.3). We see that the red-sequence galaxies show a wide range in brightness ($20.6 < F140W_{kron} < 23.9$), while the blue members are in general dimmer ($22.7 < F140W_{kron} < 23.9$). This is similar to that found from early, deep HST imaging, where blue and faint galaxies were generally classified as peculiar and with higher asymmetries (Abraham et al., 1996; Driver et al., 1995). In the top right panel of Figure 2.12, we see that the classified mergers tend to be bluer, younger and have higher asymmetry values. The red-sequence galaxies have relatively low asymmetries ($A < 0.07$), except for ID 455 and 1065, while the blue cluster members exhibit a wider range of asymmetry. The trend observed by Conselice et al. (2000b) for nearby galaxies, can also be observed in XLSSC 122, where the bluer the galaxy, the more asymmetric they tend to be.

The correlation between bulge strength and colour becomes clearer in the panels of Figure 2.12 showing the Concentration, Gini, M_{20} and the Sérsic indices, respectively. The Spearman rank correlation coefficients (Spearman, 2008) between the colour and these aforementioned morphological indices (C: 0.52, Gini: 0.59, M_{20}: 0.52 and n: 0.49) are larger than that between the colour and asymmetry (A: 0.31). The Gini index shows the strongest monotonicity with colour and confirms that the red-sequence XLSSC 122 members are hence generally more bulge-dominated, much like the red population of the $z = 1.62$ cluster presented in Papovich et al. (2012). The position of these red cluster members on the colour-Gini plot is similar to their position on the colour-concentration plot. As shown in Figure 2.13, the Gini index is proportional to the concentration, as expected.

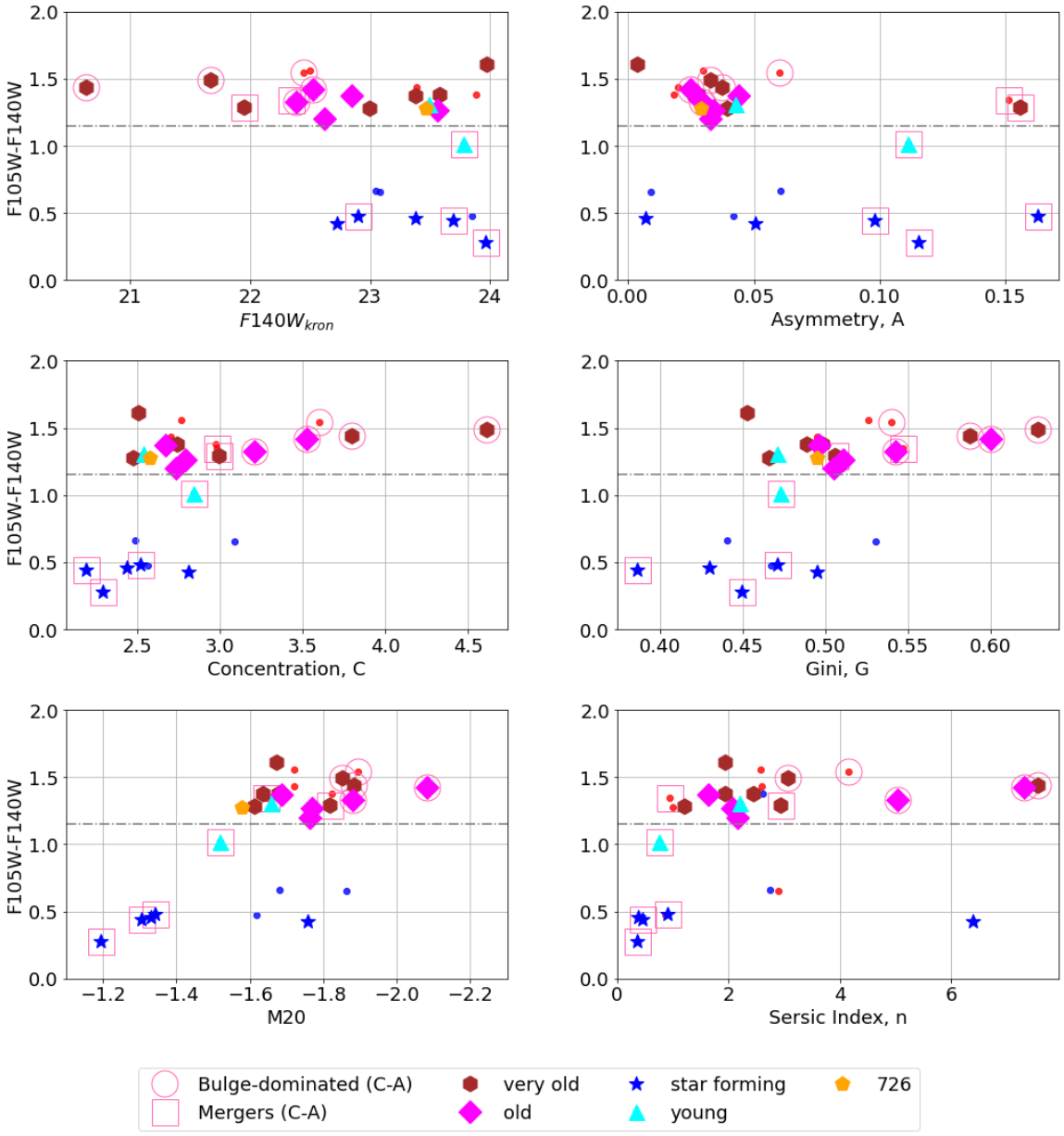

Figure 2.12: Panels show the colours of the cluster members with respect to different morphological parameters. The grey horizontal line separates the red and the blue members. The symbols represent the different age groups defined by Trudeau et al. (2022). Red and blue points are cluster members with no conclusive age measurements. The pink squares and circles shows the morphological classifications made using the C-A plot.

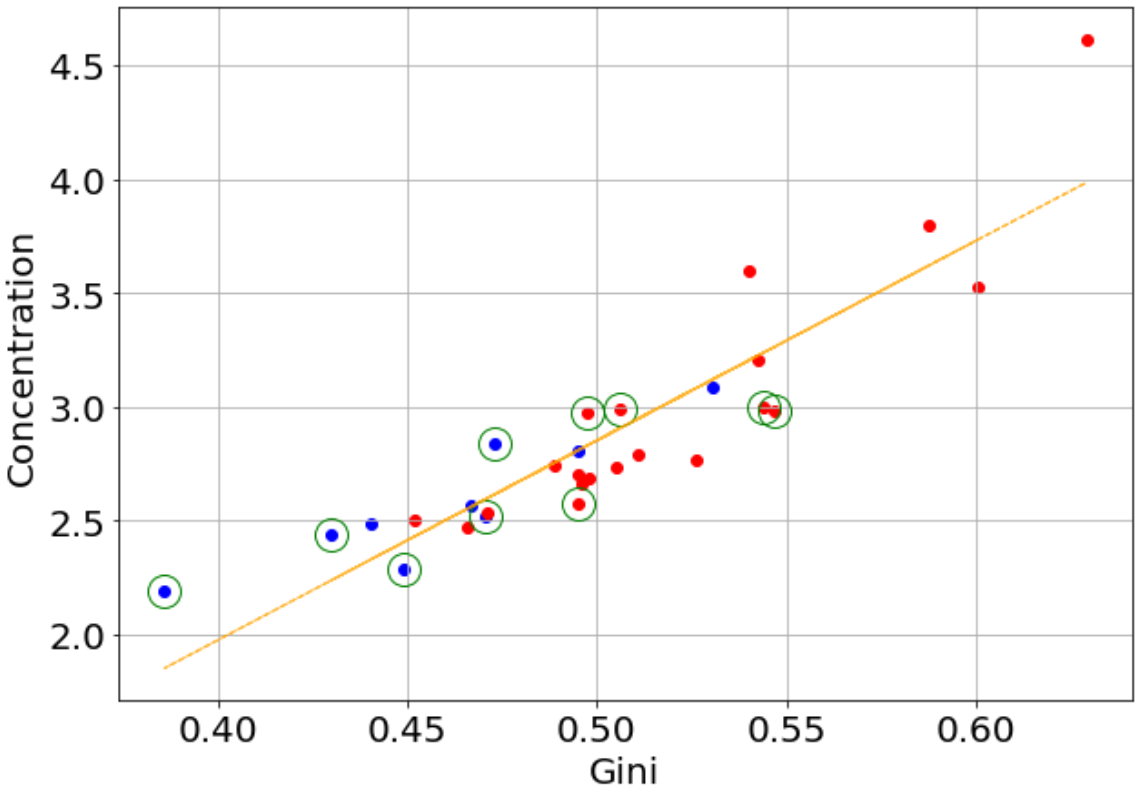

Figure 2.13: Concentration vs Gini. Green circles represent the visually disturbed members. Red and blue points represent the red-sequence and blue-cloud population of XLSSC 122. The orange line shows the least square fit to the distribution.

2.4.2 Environment

To explore the relationship between the morphologies of the XLSSC 122 galaxies and their local environments within the cluster, we find their local surface densities within the area to the 5^{th} closest neighbour for each member, derived using Equations 2.9 and 2.10. In these calculations, to find the distance to the neighbouring cluster members, we include measurements for the 29 cluster members defined in Section 2.1, as well as 29 additional red galaxies in the cluster with $P_{mem} > 0.5$ and $24 < F140W_{kron} < 26$ (Fig.2.14). The addition of the dimmer sample results in more accurate measurements to represent the local surface density of the cluster members, and strengthens the linear correlation of the local surface density to their distances from the center of the cluster R_{BCG}, as shown in Figure 2.15.

In Figure 2.16, we show the position of the XLSSC members and the respective

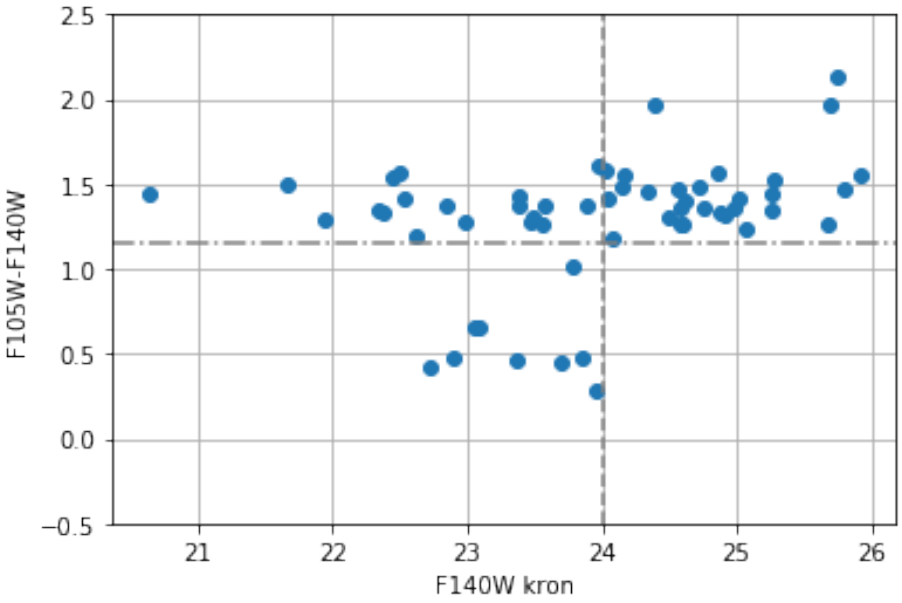

Figure 2.14: Colour-Magnitude diagram of cluster members including dimmer photometric members in the red sequence.

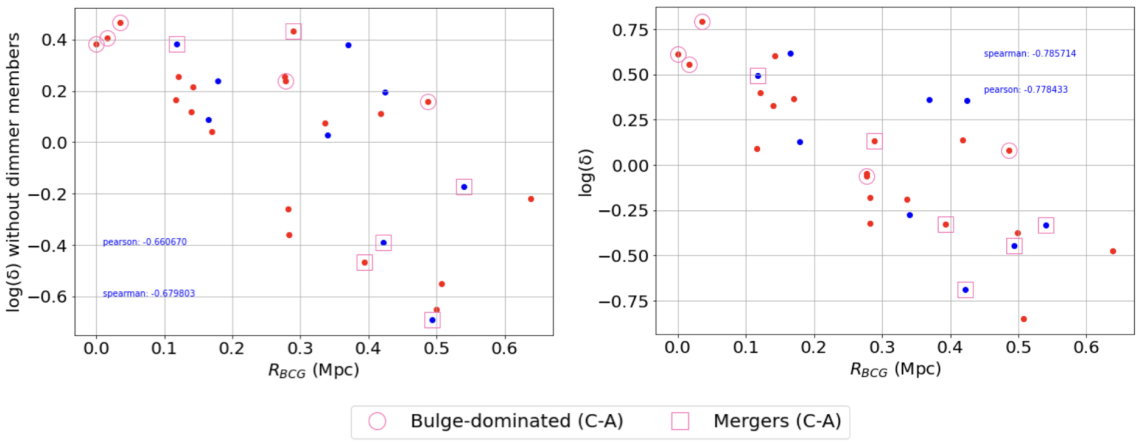

Figure 2.15: The local surface density vs R_{BCG}, where $log(\delta)$ (Equ.2.9) is calculated using only the 29 XLSSC 122 cluster members (*left panel*) and using an additional 29 dimmer red galaxies (*right panel*) (add panel to for log(delta) vs phi)

local surface density measurements, represented by $log(\delta)$ (see Eq.2.9). As expected, the highest surface density is observed in the center of the cluster in the regions surrounding the BCG (Wolf et al., 2007). We also observe two denser than average regions ($log(\delta) > 0$) to the north and south-east of the BCG within r_{200c} of XLSSC 122. We find that 6 out of the 10 visually disturbed members are located r_{500c} and

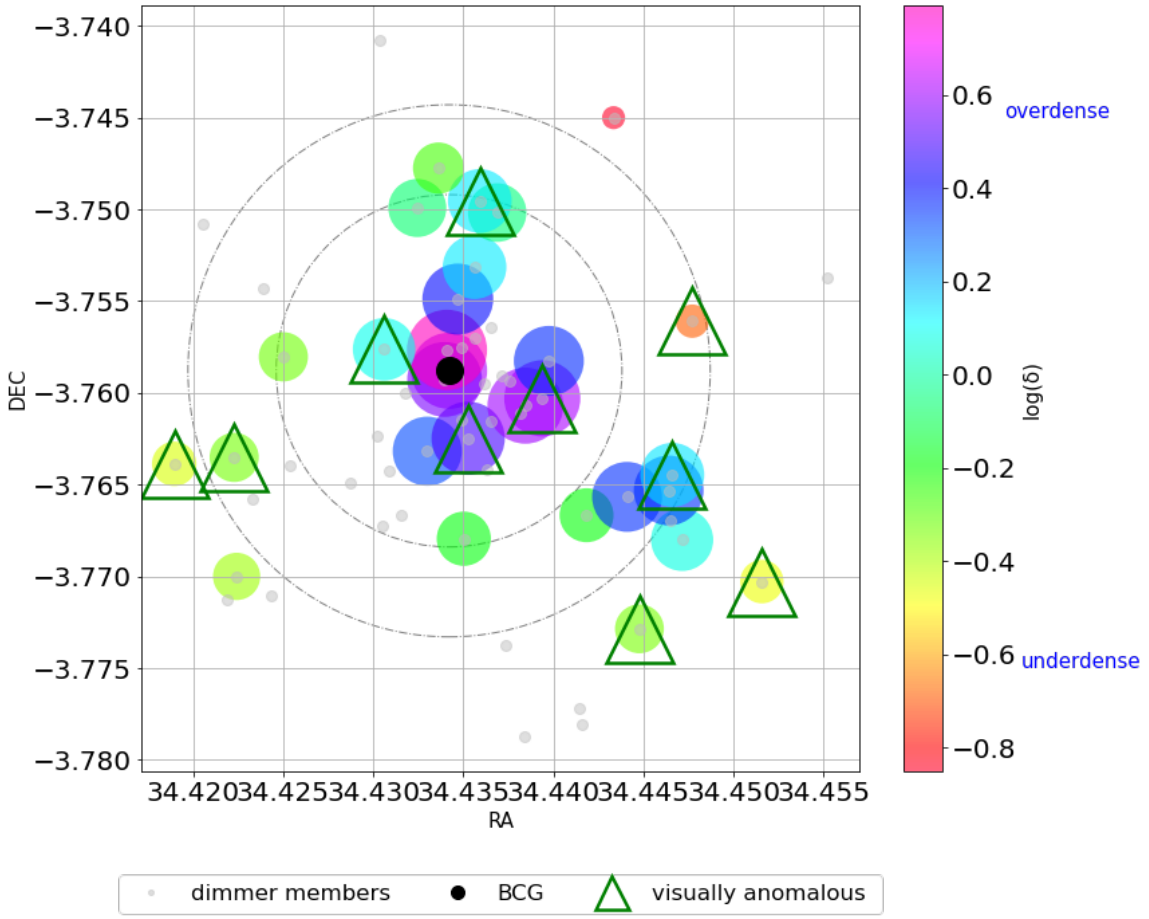

Figure 2.16: Position of cluster members. Grey points show position of dimmer cluster members as described in Fig. 2.14. Coloured markers are cluster members, whose size and colour gradient represent the local surface density defined by $log(\delta)$ (Equ.2.9). The dashed circles represent areas with r_{500c} $(inner)$ and r_{200c} $(outer)$, respectively. The visually disturbed members are represented by green triangles.

within both high and low density regions of the cluster. Noting however, that the measurements for the local surface density does not account for the third dimension projected distances, the visually disturbed members seen at the center of the cluster, may yet be at larger radii.

Figure 2.17 shows the alternative definition for the local surface density defined using the cumulative distances to the 5 nearest neighbours. In contrast to the $log(\delta)$ measurements, ϕ_5 is more sensitive to high surface density regions, making the relative difference in environment more significant (Fig. 2.18). The clumps observed using $log(\delta)$ at radii larger than r_{500c} are also seen here. Noting the positions of the galaxy members classified using the C-A plot in Figure 2.17 and 2.19, 83% of those classified

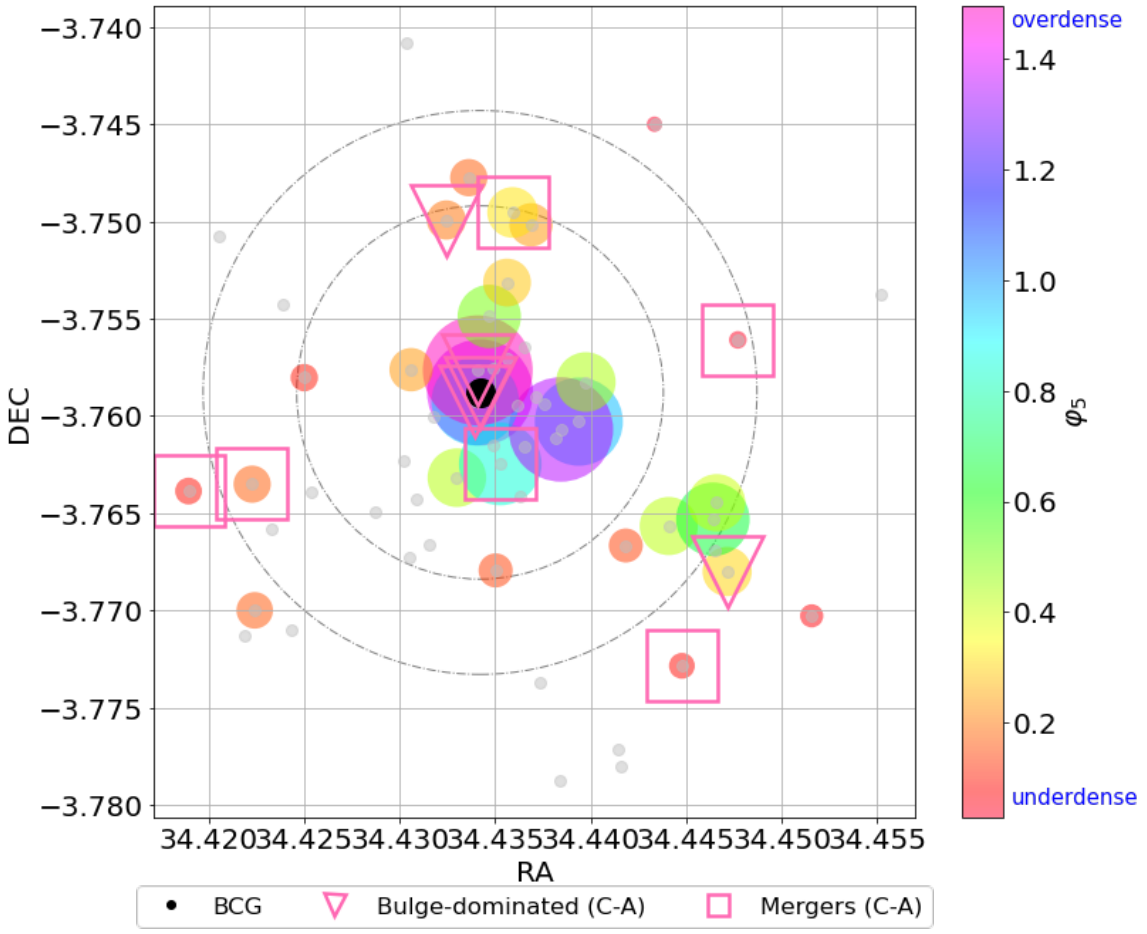

Figure 2.17: Position of cluster members. Grey points show position of dimmer cluster members as described in Fig. 2.14. Coloured markers are cluster members, whose size and colour gradient represent the local surface density defined by ϕ_5 (Equ.2.9). The dashed circles represent areas with r_{500c} (*inner*) and r_{200c} (*outer*). The pink triangles and squares represent the bulge-dominated members and possible mergers, respectively, defined in the C-A plot.

as possible mergers, which are also visibly disturbed, are in low surface density regions (lower than the average ϕ_5) of the cluster at radii greater than r_{500c}. The only exception is ID 554 found close to the cluster's center. On the other hand, 4 out of the 5 bulge-dominated members defined using the C-A plot, are in denser regions ($log(\delta) > 0$), within r_{500c}. ID 305 is the only bulge-dominated galaxy found at a radius larger than r_{200c}. This result is consistent with studies of nearby galaxies, where bulges and elliptical structures are located in higher density regions (Gómez et al., 2003; Blanton & Moustakas, 2009).

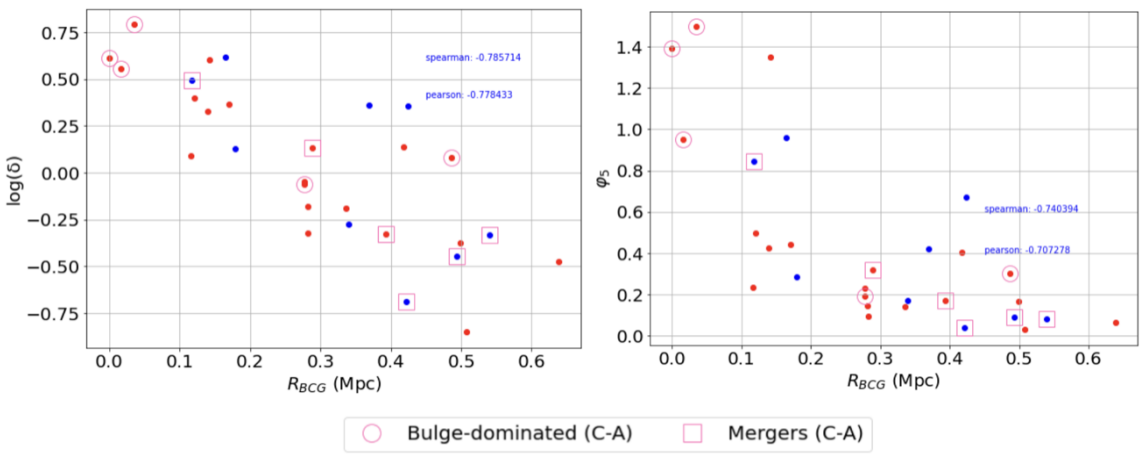

Figure 2.18: The local surface density vs R_{BCG}. *Left panel* shows $log(\delta)$ and *Right panel* shows ϕ_5.

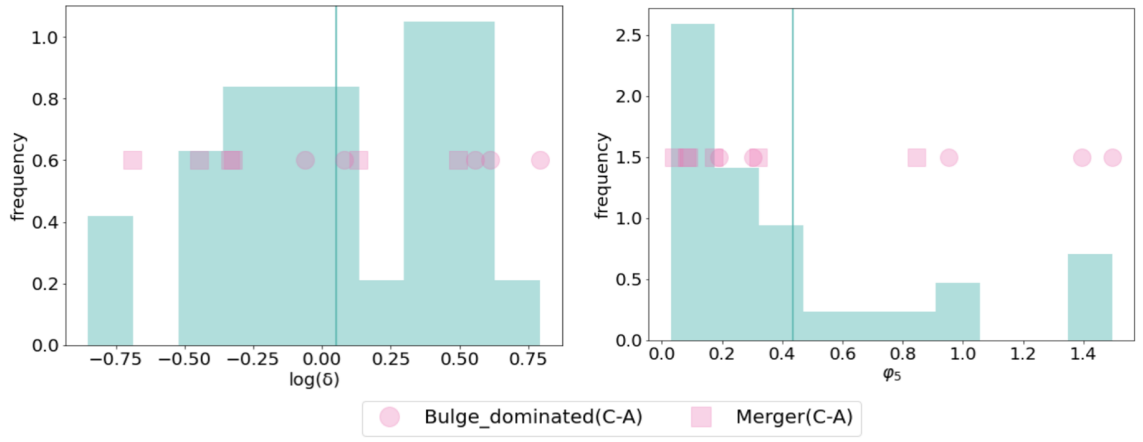

Figure 2.19: Histogram showing the distributions of $log(\delta)$ (*left*) and ϕ_5 (*right*) measurements for the XLSSC 122 cluster members. The vertical line shows the mean $log(\delta)$ and ϕ_5 accordingly and the pink circles and squares show the measurements for the bulge-dominated and disturbed cluster members, respectively.

We explore the relationship between the measurements of morphology to the local surface density of the XLSSC 122 members in Figures 2.20 and 2.21. The members in the denser region are the brightest and classified as being bulge-dominated using the C-A plot. Though no clear trend is seen with colour and the local surface density, the 3 cluster members found within $R_{BCG} < 100$ kpc, are all part of the red-sequence and bulge-dominated. We also observe that the brightest objects with the highest Gini and concentration values are found in the densest regions of the cluster. Compared

to $log(\delta)$, distributions of the ϕ_5 measurement, show clearer bimodality separating members in denser regions and those that are more isolated. Cluster members with lower bulge strength form clumps at low surface density values.

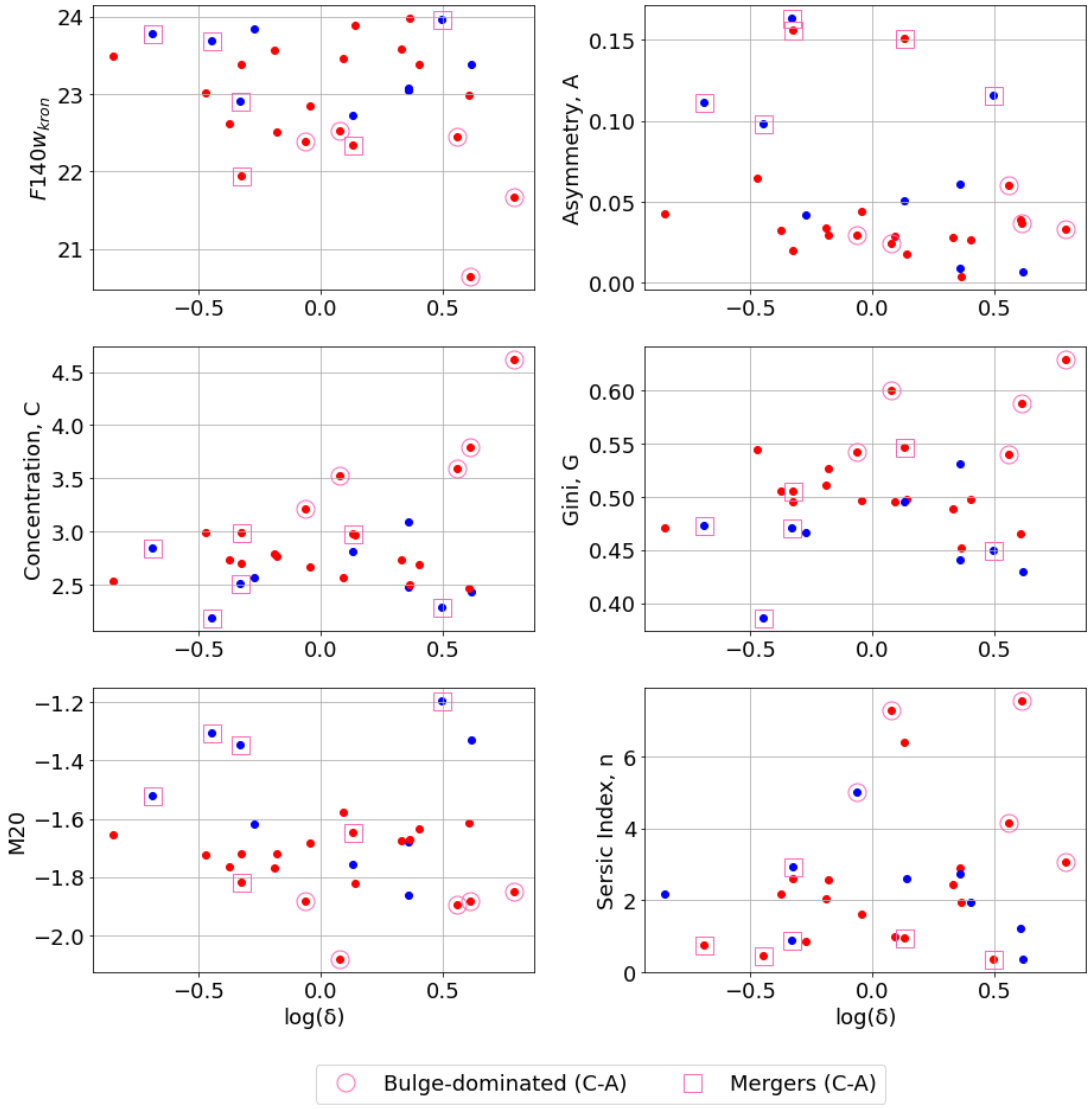

Figure 2.20: Panels shows the relationship of the local surface density, $log(\delta)$ (Eq.2.9) of the cluster members with respect to the different morphological parameters. Red and blue dots represent cluster members in the red and blue sequence respectively. Pink circles and squares represent the bulge-dominated galaxies and mergers of XLSSC 122, respectively, according to the C-A plot.

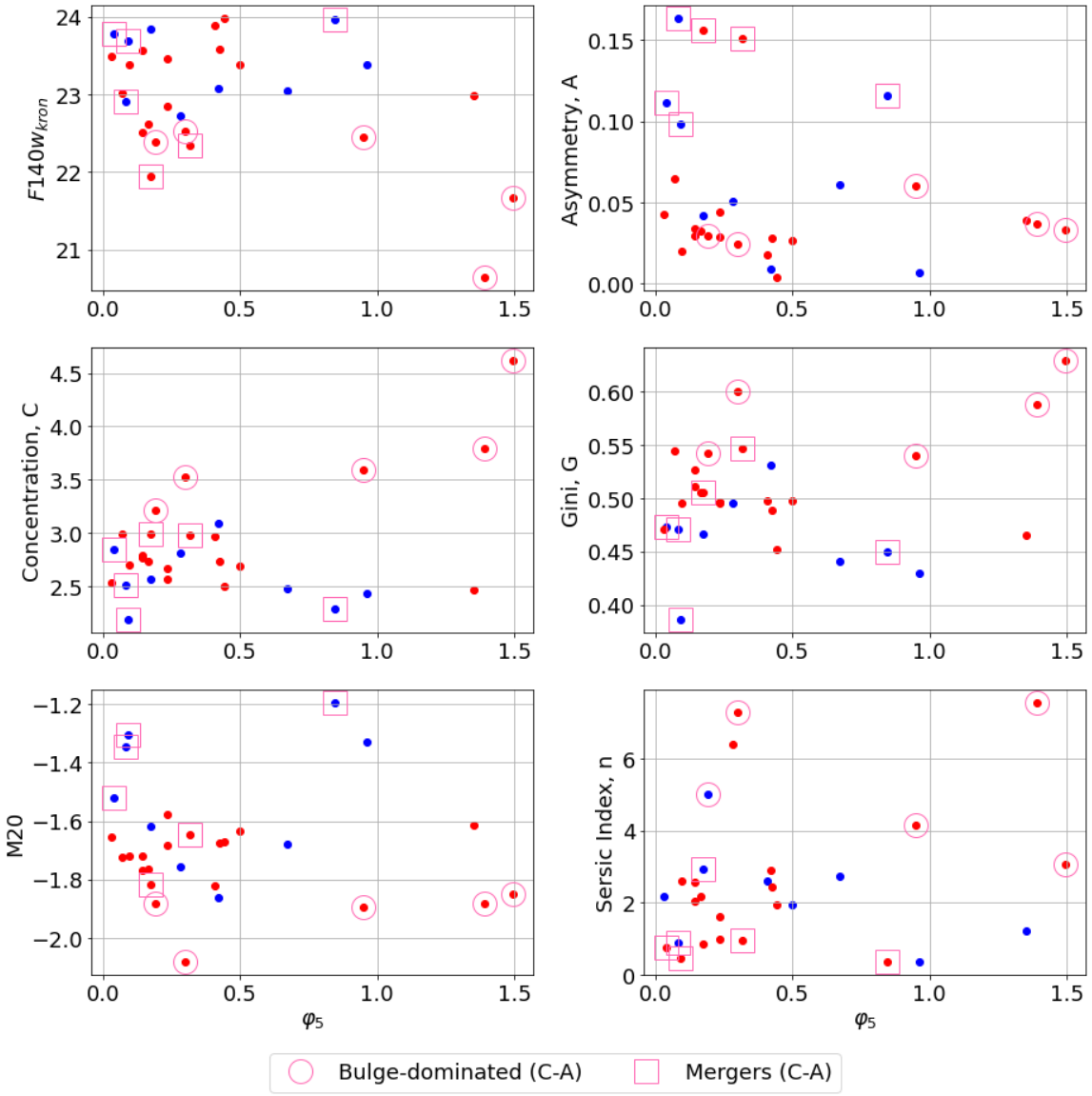

Figure 2.21: Panels shows the relationship of the local surface density, ϕ_5 (Eq.2.10) of the cluster members with respect to the different morphological parameters. Red and blue dots represent cluster members in the red and blue sequence respectively. Pink circles and squares represent the bulge-dominated galaxies and mergers of XLSSC 122, respectively, according to the C-A plot.

2.4.3 Comparing Mass and Age to Morphology

As described in Section 2.2.2, we use the median mass and age values resulting from the SED modelling of the XLSSC 122 galaxies by Trudeau et al. (2022). We take the 16^{th} and 84^{th} percentiles of the probability distributions of these parameters to

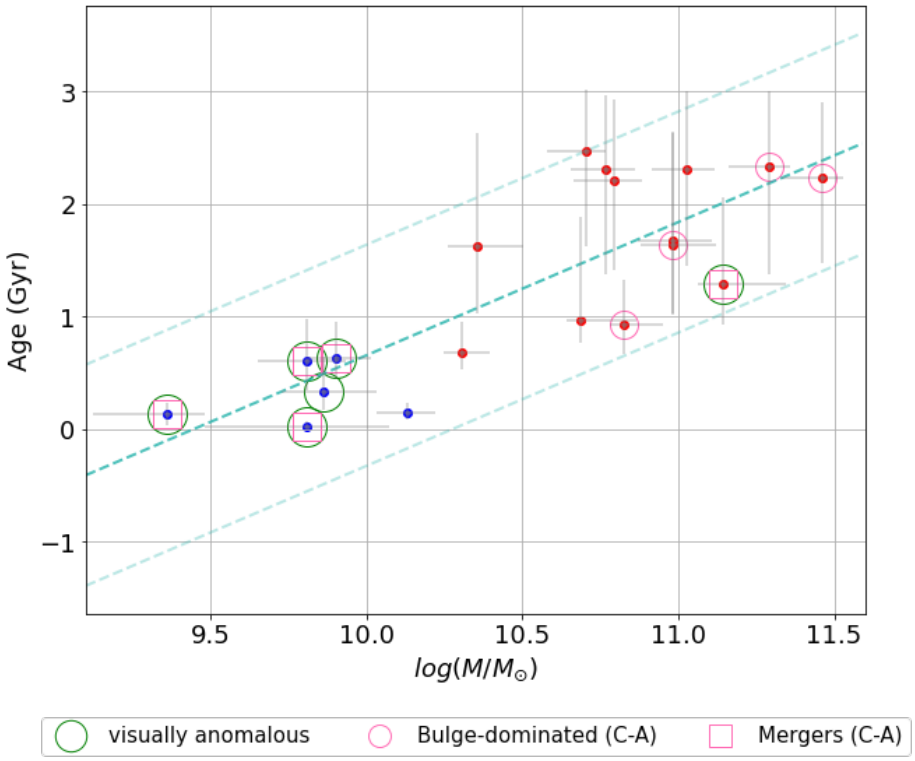

Figure 2.22: Mass vs Age. The error bar are the 16^{th} and 84^{th} percentiles of the measurements resulting from the SED modelling. The blue dash lines represent the least square fit to the distribution of mass and age, and the 2σ deviation from the fit.

represent the uncertainties on these estimates.

In Figure 2.22, we find that the mass and age of the XLSSC 122 members are monotonically correlated (Spearman rank correlation coefficient of 0.79). We see a trend whereby the blue cluster members which also show disturbed structures have masses with $log(\frac{M}{M_\odot}) < 10.2$ and are younger than 1 Gyr. While the red-sequence and bulge-dominated galaxies are more massive and older, similar to observations of another high redshift cluster performed by Papovich et al. (2012). The mass of the classified bulge-dominated galaxies have $log(\frac{M}{M_\odot}) > 10.8$.

The trends comparing Gini, M_{20}, concentration and asymmetry to the age and mass are shown in Figure 2.23 and 2.24, respectively. There is a direct correlation between the bulge-strength, shown in terms of M_{20} and both the age and mass of the cluster members. This observation is more significant between the mass and the morphological indices. The more massive and older members have more concentrated light distributions, while the mergers and young galaxies have higher asymmetries

and are less bulge-dominated.

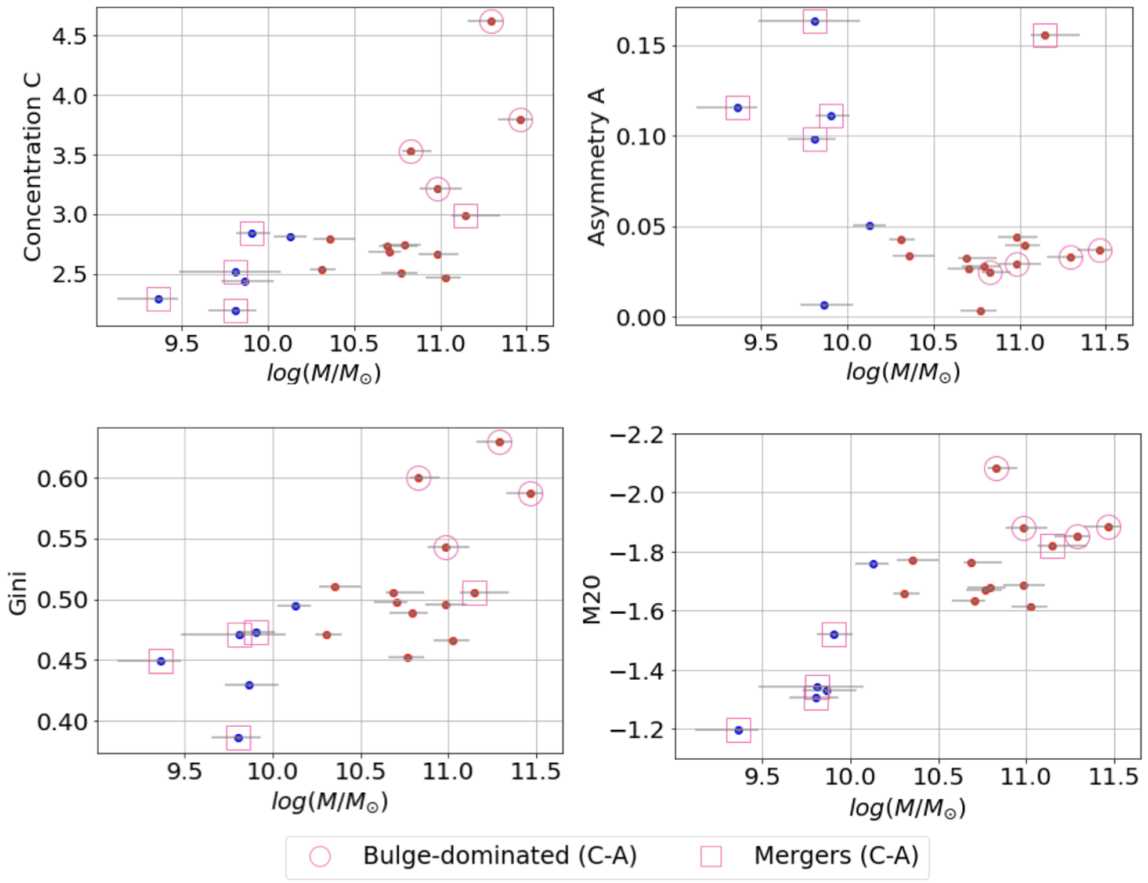

Figure 2.23: Mass versus Morphology. Red and blue dots represent cluster members in the red and blue sequence respectively. Pink circles and squares represent the bulge-dominated galaxies and mergers of XLSSC 122, respectively, according to the C-A plot.

Noting that the age and mass are correlated to each other and thus show similar trends with the morphological indices, we perform a Partial Spearman's Rank Correlation test (Liu et al., 2018) to deduce the main property driving morphological evolution in the cluster. The resulting correlation coefficients represent the relationship between two variables (X and Y), after removing the dependence on a third variable (Z). Table 2.2 list the correlation coefficients relating the morphological indices to the mass, correcting for the age, and vice versa. We observe higher correlation between the mass and Gini, M20 and the concentration, which remains after correcting for the age dependence. On the other hand, the correlation is not recovered after correcting for the mass dependence between the age and the morphological parameters. Hence,

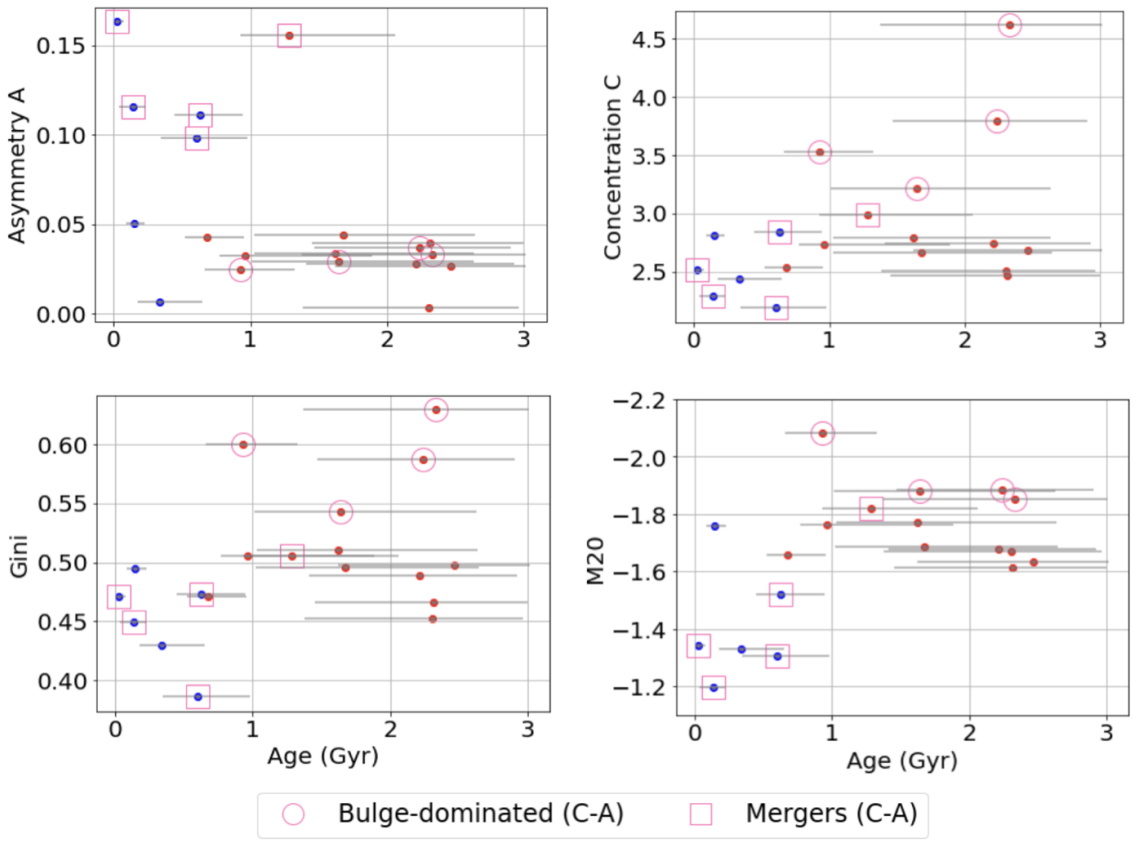

Figure 2.24: Age versus Morphology. Red and blue dots represent cluster members in the red and blue sequence respectively. Pink circles and squares represent the bulge-dominated galaxies and mergers of XLSSC 122, respectively, according to the C-A plot.

galaxy mass may be the main property responsible for the morphological differences in members of the cluster.

Table 2.2: Partial Spearman's Correlation Coefficient between X and Y controlling for Z

X	Y	Z	Correlation Coefficient
Mass	Gini	Age	0.553
Mass	M20	Age	-0.736
Mass	C	Age	0.543
Mass	A	Age	0.120
Age	Gini	Mass	-0.169
Age	M20	Mass	0.292
Age	C	Mass	-0.251
Age	A	Mass	-0.300

Additionally we look at the relationship between the mass and the age with respect to the environment of the cluster members in Fig. 2.25. There is no apparent mass correlation with either the local surface density or the distance to the BCG. We see, however, a relationship between the positions of the galaxies within the cluster and their ages. Older members tend to be closer to the center and in denser regions, while younger members are in the outskirts and in more diffuse regions.

2.4.4 Comparison of XLSSC 122 to other Galaxy Population

To better contextualise the morphological properties of the XLSSC 122 cluster members, we compare their morphology measurements with those of other high redshift galaxy clusters and field galaxies.

Comparison to other high redshift clusters.

We use the morphological measurements of the 4 clusters presented by Sazonova et al. (2020) described in Section 2.2.4. As shown in Figure 2.26, the distribution of the XLSSC 122 cluster members matches that of the S20 sample and the 'main sequence' for both samples closely overlap (Equations 2.11 and 2.12). This similarly suggests that the morphologies seen within these 5 clusters at high redshifts are fairly uniform. The fraction of galaxies classified into the main 2 morphological groups, are approximately the same in both samples. Figures 2.27 compares the distributions of the Gini and M20 measurements for the members of XLSSC 122 and S20 clusters. A Kolmogorov-Smirnov test (Jr., 1951) results in a large p-value for both measurements and therefore, the null hypothesis that both distributions were drawn from the same

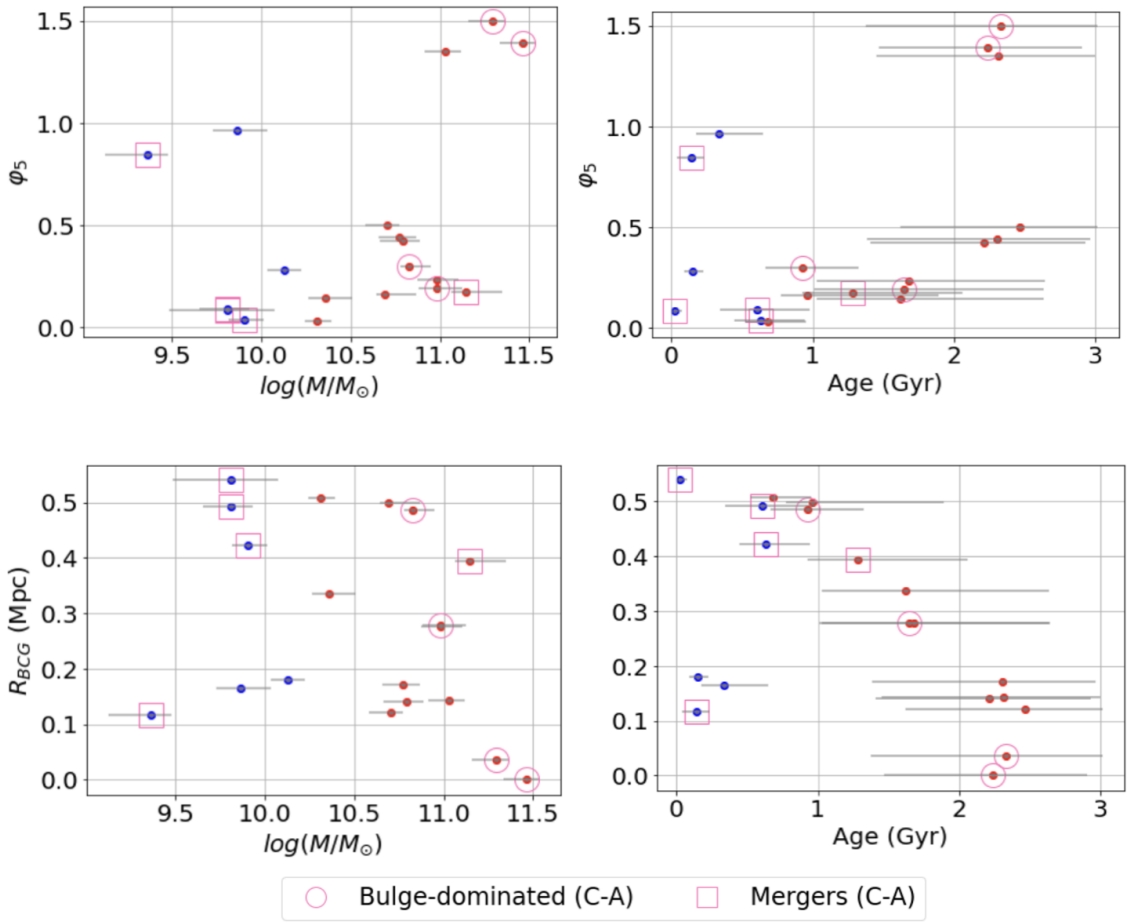

Figure 2.25: Mass and Age with respect to local surface density. Red and blue dots represent cluster members in the red and blue sequence respectively. Pink circles and squares represent the bulge-dominated galaxies and mergers of XLSSC 122, respectively, according to the C-A plot

sample cannot be rejected.

$$\text{S20 Gini-}M_{20}\text{ 'main sequence': } G = -0.21M_{20} + 0.15 \tag{2.12}$$

We also compare the position of the S20 cluster members to that of the XLSSC 122 members on the C-A plot (Fig.2.28). Unlike the Gini-M_{20} relationship, the S20 members show a much wider range of asymmetry and concentration compared to the XLSSC 122 members. Performing a Kolmogorov-Smirnov (KS) test for the two morphological indices between the 2 sample, we cannot reject the null hypothesis for the concentration values. As shown in Figure 2.29, however, the distributions for the asymmetry largely differ. The S20 sample has a larger fraction of cluster members

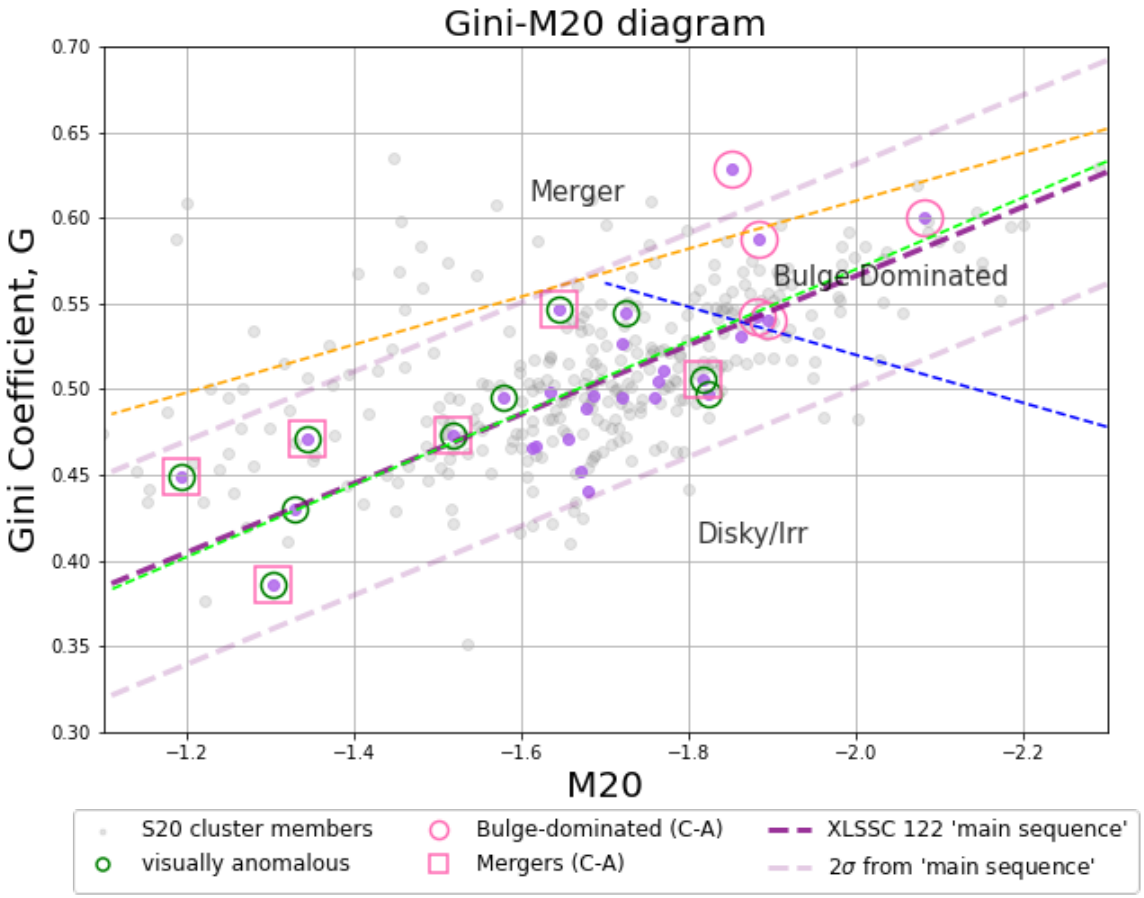

Figure 2.26: Gini-M_{20} plot comparing measurements for XLSSC 122 members and the S20 sample. The blue and orange boundaries are defined by Lotz et al. (2008b) to separate between disky, bulge-dominated and mergers. The purple dashed line is the 'main sequence' of the Gini-M_{20} distribution of XLSSC 122 members and the pale purple dashed line shows the 2σ deviation from the 'main sequence'. The neon green dashed line shows the 'main sequence' for the Sazonova et al. (2020) sample. Visually disturbed XLSSC 122 members are circled in green. The pink circles and squares shows the bulge-dominated and mergers in XLSSC 122 classified using the C-A plot.

with high asymmetries.

It is important to note that the cluster membership of the S20 sample is subject to contamination by field and foreground galaxies due to the limitations from the image quality and the larger inaccuracies in using the red-sequence selection method and a lack of spectroscopically confirmed members.

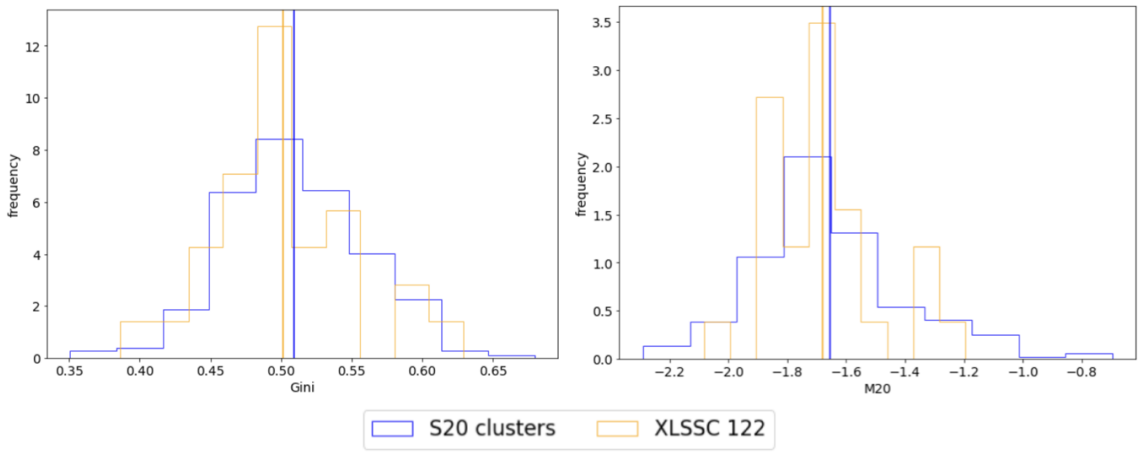

Figure 2.27: Histogram showing the distribution of the Gini index (*left*) and M20 (*right*) measurements for the XLSCC 122 members and the S20 cluster members. The vertical lines shows the means of the two samples.

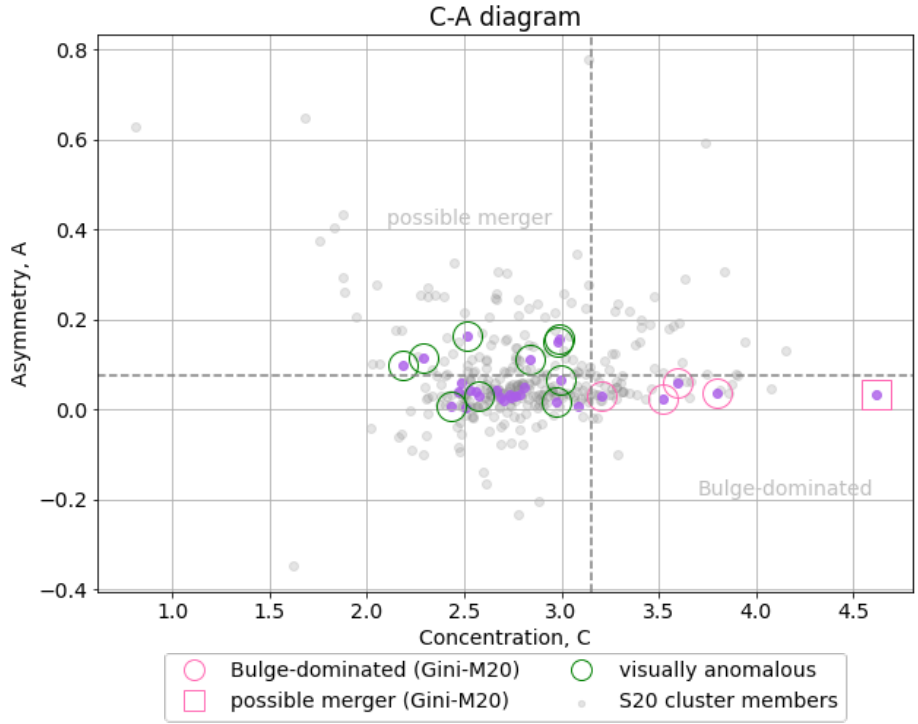

Figure 2.28: C-A plot comparing measurements for XLSSC 122 members and the S20 sample. Purple points are the XLSSC 122 members and the grey points are from the S20 sample. Boundaries and symbols are the same as in Fig.2.11.

Comparison to Field Galaxies.

We next compare the morphologies of the XLSSC cluster members to those of field galaxies, to further our understanding of the effects of these starkly different environ-

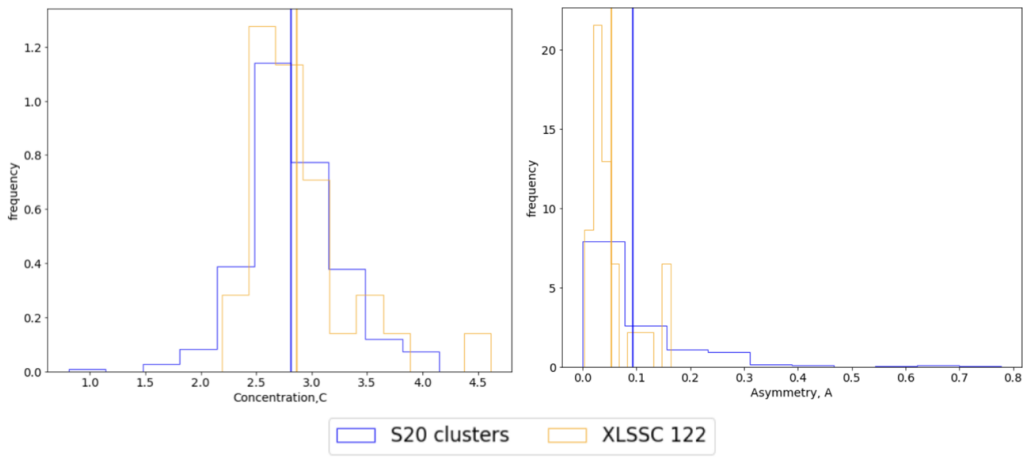

Figure 2.29: Histogram showing the distribution of the Concentration (*left*) and Asymmetry (*right*) measurements for the XLSCC 122 members and the S20 cluster members. Vertical lines shows the mean of the two samples.

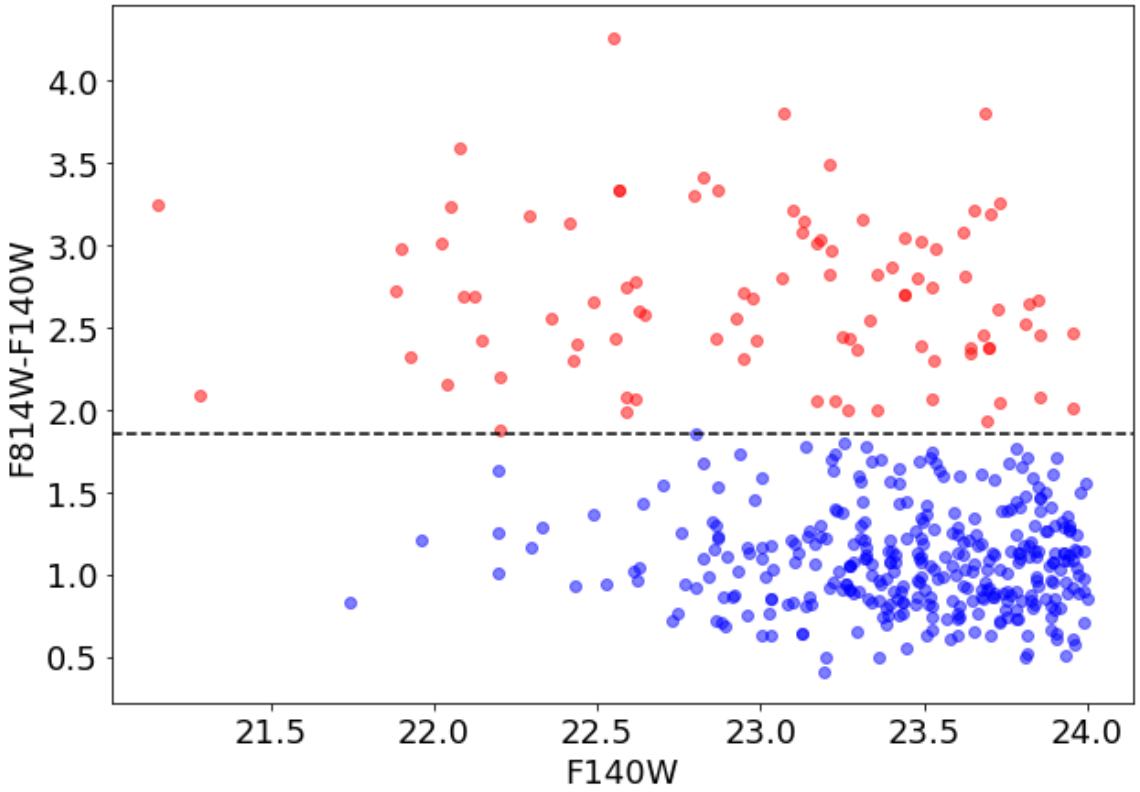

Figure 2.30: Colour-Magnitude Diagram (F814W-F140W vs F140W) of field galaxies at $z = 2$. The dashed like shows the lower colour limit for the field galaxies to be in the red-sequence (F814W-F140W= 1.85).

ments on the evolution of galaxies. Multiple studies at lower redshift have previously investigated the trends in properties between galaxies in clusters and the field (Papovich et al., 2012; Strazzullo et al., 2019; Cantale et al., 2016; Hennig et al., 2017).

Figure 2.30 shows the CMD for the field galaxies selected as described in Section 2.2.3 from the CANDELS/3D-HST fields. Since there are no available images in the F105W band, we construct the CMD using the F814W band, which is the closest available filter to F105W. Galaxies with F814W-F140W > 1.85 are classified as red-sequence galaxies, based on the bimodal distribution in colour. Already we see a striking distinction to the CMD of the cluster galaxies. The field sample consists primarily of blue galaxies, making up 63% of the sample. On the other hand the blue cloud population in XLSSC 122 accounts for only 32% of the cluster members. This suggests that the galaxies in the field at $z = 2$ are actively forming stars, while the cluster members are more likely to have experienced events suppressing their star formation.

Similarly to the XLSSC 122 sample, we use STATMORPH on F140W cutouts of the field galaxies to measure their concentration, asymmetry, Gini and M_{20} values. We first use the Gini-M20 plot to gain insight on the morphological classification of the field galaxies. Figure 2.31 shows that the field galaxies follow a similar distribution, though the slope of the 'main sequence' for the field population is flatter than that of the XLSSC 122 members (Eq. 2.13). 42 field galaxies are classified as mergers while only 25 are bulge-dominated, according to the Gini-M_{20} analysis. These observations agree with the notion that dense environments in clusters suppress galaxy interactions due to the prevailing high velocity dispersions, while in the field where velocity dispersions of galaxies are lower, galaxy mergers are favoured.

$$\text{Field Gini-}M_{20}\text{ 'main sequence': } G = -0.09M_{20} + 0.34 \tag{2.13}$$

We additionally look at the distribution of the field galaxies on the C-A plot (Fig. 2.32). We see that 92% of the field galaxies have concentrations lower than the bulge-dominated lower limit (C< 3.1), set by the distribution of XLSSC 122 members (Section 2.4.1). 82% of these low concentration field galaxies have asymmetries greater than the largest asymmetry value of the cluster members. This further confirms that more disturbed galaxy systems are observed in more isolated regions of the universe.

In Figure 2.33 we compare the distribution of concentration, asymmetry, Gini and M_{20}, between the field and cluster galaxies. A KS-test comparing the two samples for

each morphological index reveals that the null hypothesis that the 2 distributions are drawn from the same sample can be rejected (p-value < 0.05) for the asymmetry and M_{20} measurements. The asymmetry values for the field galaxies are on average higher and reach higher values than the cluster members. Similarly, the M_{20} measurements for the field galaxies are skewed towards lower negative values. Since M_{20} can be used as a measure for the bulge-strength of the galaxies (Fig.2.10), we can deduce that XLSSC 122 is deficient in galaxies with lower bulge-strength and higher asymmetry.

We further explore the colour-morphology relationships in the field and the XLSSC 122 cluster, shown in Figures 2.34 and 2.35. As opposed to the XLSSC 122 members, the distribution of concentrations for the field red and blue population are similar. The red-sequence cluster population has members with higher concentrations than

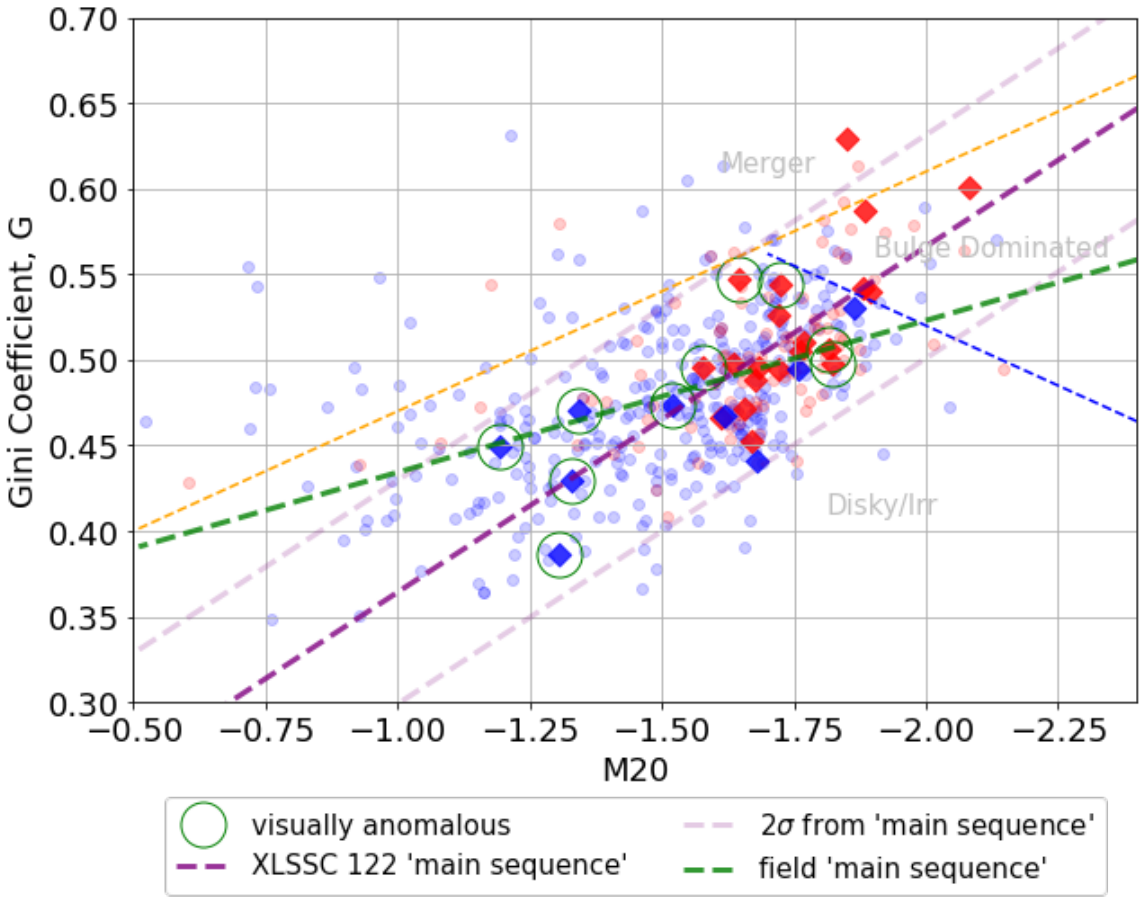

Figure 2.31: Gini-M20 plot for field galaxies at $z = 2$. The red and blue dots represent the red-sequence and blue cloud from the field sample. The red and blue diamonds shows the XLSSC 122 cluster members. The delimitations are the same as in Figure 2.8. The green dashed line is the least square fit to the field sample.

the red field galaxies, while some blue field galaxies have larger concentrations than the cluster's blue-cloud. The skewness in the distribution of the field asymmetry and M_{20} values, seems to be mainly due to the disturbed structures of the blue galaxies. On the other hand, the distribution of Gini values does not differ greatly between the field and the cluster. In both environments, the blue population has on average lower Gini values than the red-sequence galaxies.

Using the available mass measurements of the field galaxies from SED fitting using FAST (Kriek et al., 2009), we investigate the relationship between their morphology and stellar mass (Fig.2.36). As expected, the red-sequence field galaxies are generally more massive than the blue-cloud galaxies, similar to the cluster galaxies. The masses

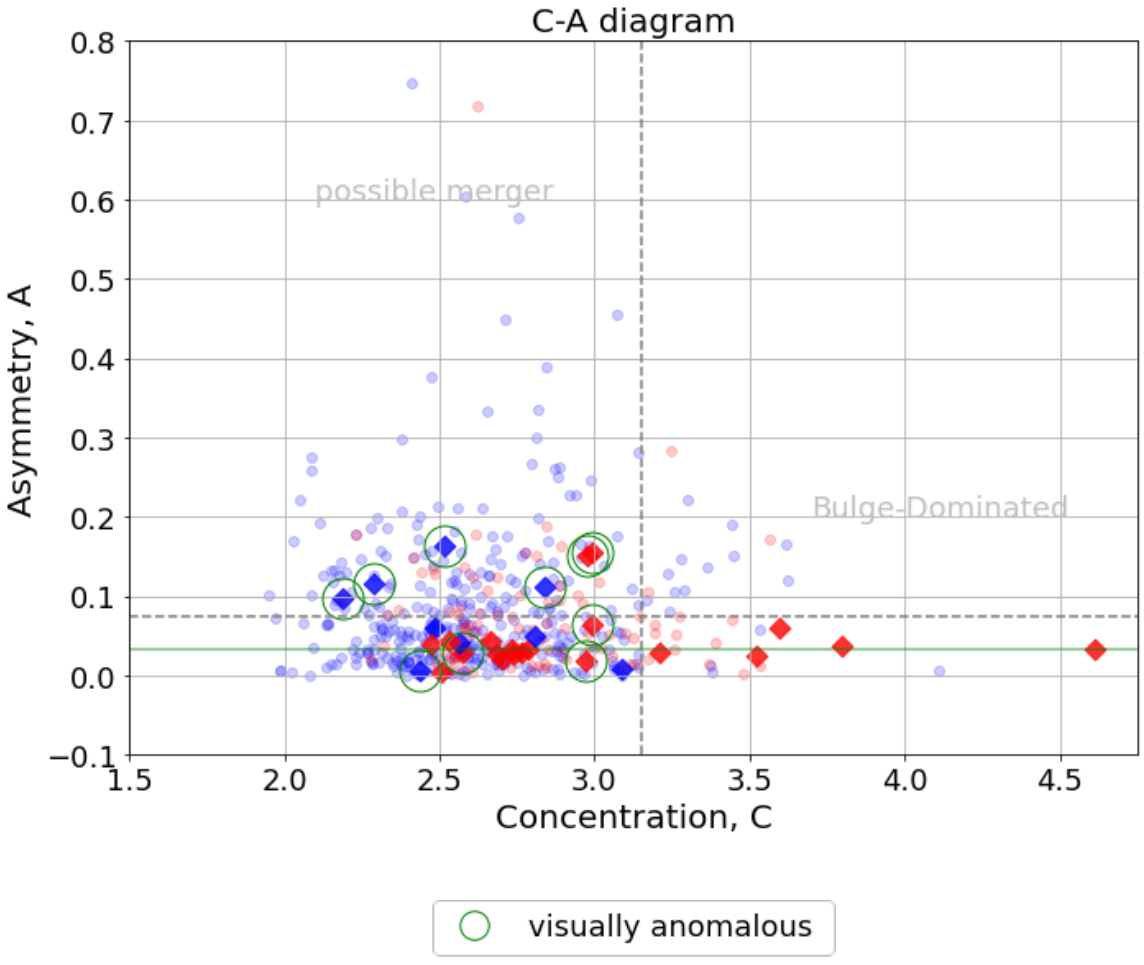

Figure 2.32: C-A plot for field galaxies at $z = 2$. The red and blue dots represent the red-sequence and blue cloud from the field sample. The red and blue diamond shows the XLSSC 122 cluster members. The delimitations are the same as in Figure 2.11.

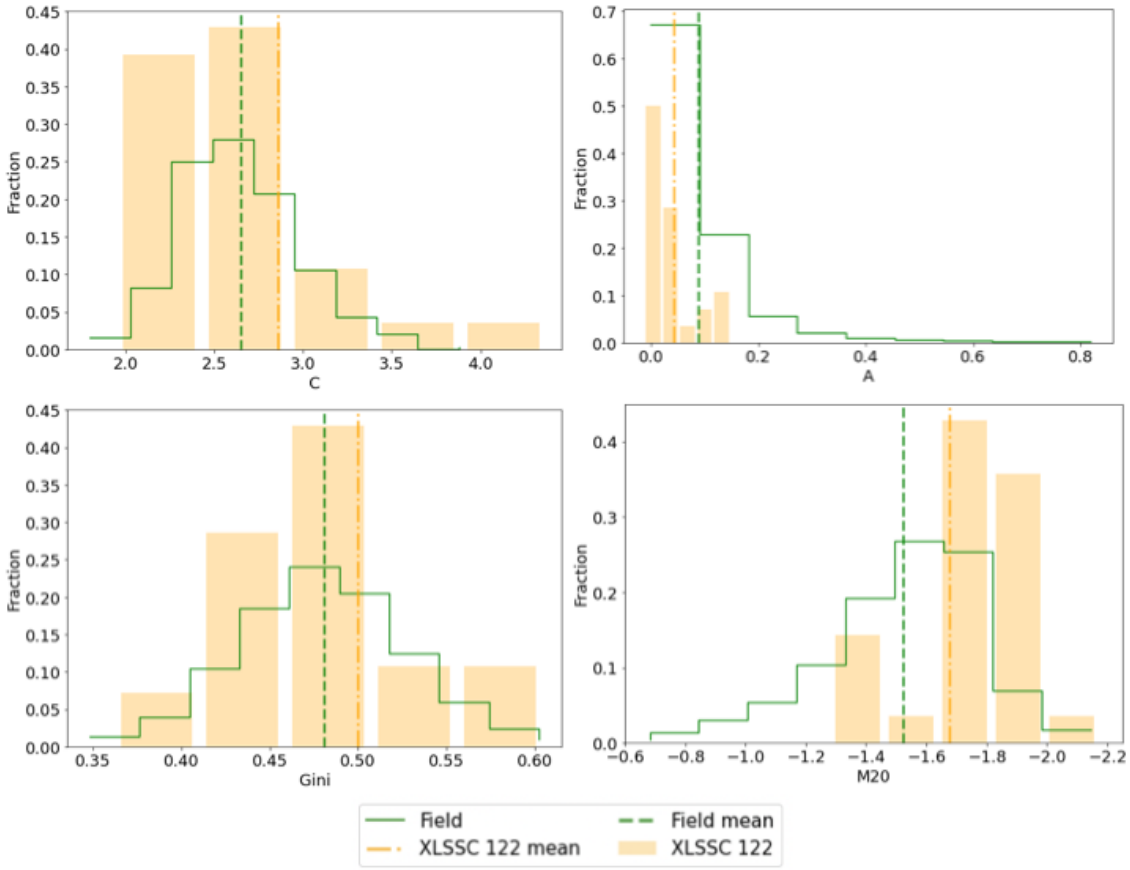

Figure 2.33: Histograms comparing the distributions of morphologies of the cluster and field galaxies. The dashed lines show the mean of each distribution.

of the XLSSC 122 members and those in the field span over similar ranges, though the field blue-cloud contains more massive galaxies than in the cluster. The low mass blue field galaxies ($log(M/M_{\odot}) < 10.2$) account for the highly asymmetric population of galaxies. Moreover, compared to the more massive red galaxies in XLSSC 122, the field red-sequence has galaxies with low bulge-strength (in terms of M_{20} values). These observations indicate signs of galaxy interaction in the red field population, which is absent in the XLSSC 122 cluster.

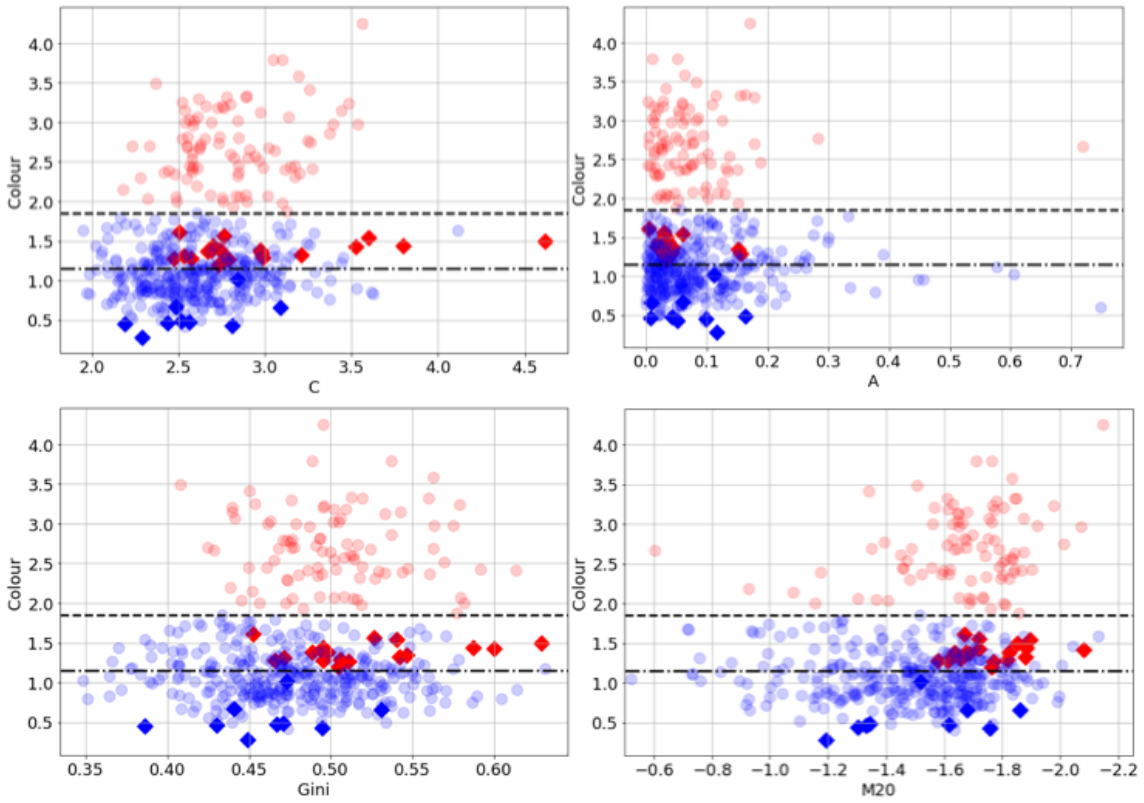

Figure 2.34: The panels show the colour of the field and cluster galaxies versus the morphological indices C, A, Gini and M20. The red and blue dots represent the red-sequence and blue cloud from the field sample. The red and blue diamonds shows the XLSSC 122 cluster members. The dashed line shows the lower colour limit for the field galaxies to be in the red-sequence (F814W-F140W= 1.85) and the dashed-dotted line shows the lower colour limit for the XLSSC 122 galaxies to be in the red-sequence (F105W-F140W= 1.15).

2.5 Discussion

Our analyses of the XLSSC 122 HST images reveal that the cluster has an established population of red-sequence galaxies with high bulge-strength, as well as a population of disturbed blue galaxies. By first using the Gini-M_{20} diagram and regions defined by Lotz et al. (2008b) to classify the cluster members, a clear sample of 4 bulge-dominated galaxies is found. However this method does not effectively recover the visually disturbed galaxies (Fig.2.4), which may be indicative of recent merger events. Instead, these galaxies are classified as disky or irregular galaxies.

If a line is drawn to separate the majority of the visually disturbed members, such

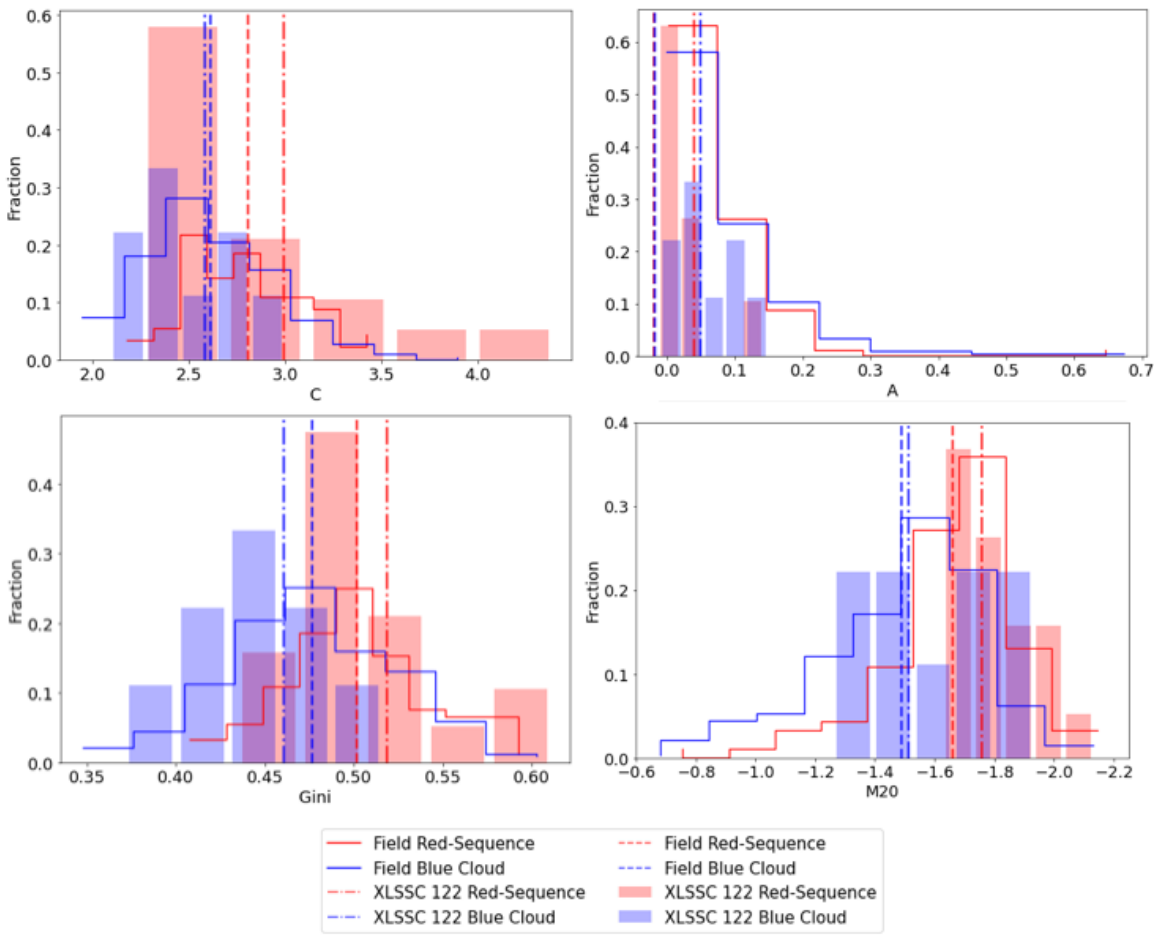

Figure 2.35: Histograms comparing the distributions of morphologies for the red and blue population of the cluster and field galaxies. The dashed lines show the mean of each distribution.

as the line defined by Equation 2.14 and shown in Figure 2.37, the separation is closer to the 'main sequence' of both the S20 and XLSSC 122 cluster members (within a σ deviation). It is also much steeper and shifted towards lower Gini values, compared to the separation described by Equations 2.3.2 for galaxies in these high redshift and high mass clusters.

Consequently, if the 'main sequence' of the cluster members on the Gini-M_{20} diagram is used as the lower limit to detect possible mergers, we recover 70% of the visually disturbed members (except for the red-sequence disturbed members ID 434 and 454). This may be an indication that this classification method may need to be adjusted depending on the redshift of the galaxy population being observed, especially for the detection of possible mergers.

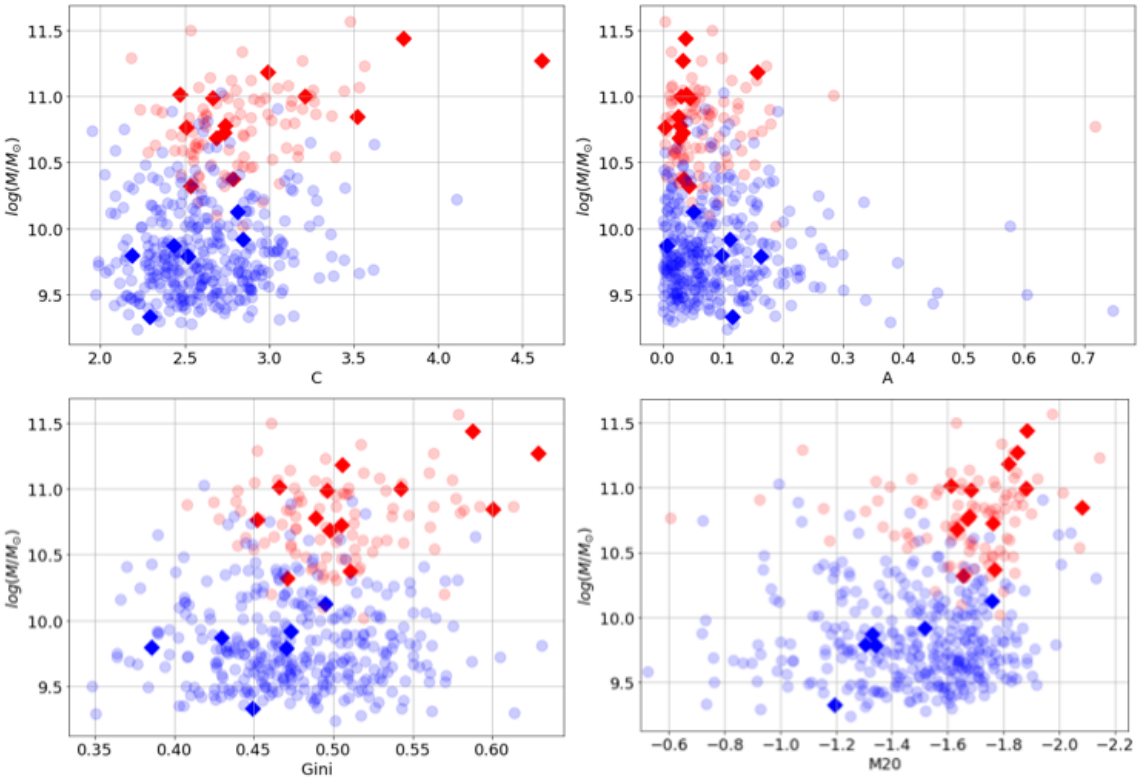

Figure 2.36: The panels show the Mass of the field and cluster galaxies versus the morphological indices C, A, Gini and M20. The red and blue dots represent the red-sequence and blue cloud from the field sample. The red and blue diamond shows the XLSSC 122 cluster members.

Another possibility as to why we do not recover the visually disturbed cluster members using Gini-M_{20}, may be due to the limitations of the technique in the type of mergers detected. It was found that the method is effective at identifying mergers from the presence of double nuclei, which are only evident during a merger event over short timescales (Lotz et al., 2008b,a, 2010). This would suggest that the disturbed galaxies in XLSSC 122, are not due to active mergers occurring at the epoch of observation, but instead are remnant features from prior interactions.

Separation of visually disturbed XLSSC 122 members: $G = -0.09M_{20}+0.34$ (2.14)

The C-A plot is efficient at recovering the bulge-dominated galaxy population classified using the Gini-M_{20} (including ID 661). Since the identification of bulge-dominated galaxies is less evident visually, especially for images with lower resolution,

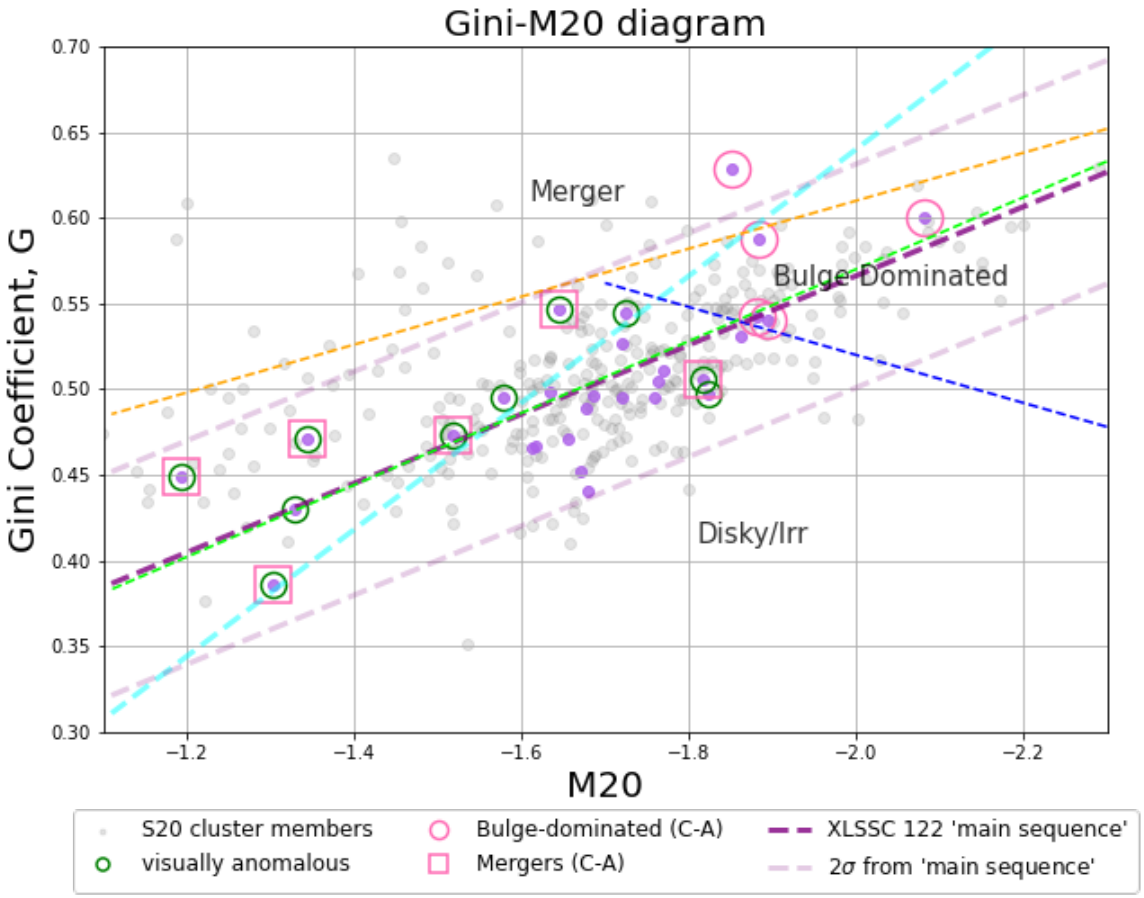

Figure 2.37: Gini-M_{20} plot comparing measurements for XLSSC 122 members and the S20 sample. The symbols are the same as in Fig.2.26. The cyan dashed line shows a suggested separation of the visually disturbed members.

it is necessary to use quantitative methods to confirm their presence. Both Gini-M_{20} and C-A effectively detect XLSSC 122 members that are visually consistent with structures of bulge-dominated galaxies.

Furthermore the C-A method recovers the majority of the visually disturbed cluster members. However it is important to note that the mergers detected using concentration and asymmetry have previously been suggested to be preferentially at the first pass of the merger or at the last stage resulting in the merger remnant, but are less likely to detect mergers during the intermediate stages of the interaction (Conselice, 2014). In Lotz et al. (2010), the possible mergers found using asymmetry are more likely to be major merger remnants with merger timescales of 0.2 to 0.4 Gyr at lower redshifts, while Gini-M_{20} is also sensitive to minor mergers. Moreover, Lotz et al. (2008a) found that high asymmetry values last longer than Gini and M_{20} values

during galaxy interactions, which are also retained after the coalescence of the progenitors. These behaviours hint towards the idea that we are not observing galaxies actively merging in the cluster. However this conclusion may differ for high redshift galaxies, since asymmetry values are sensitive to the to the gas fraction, which is higher in the early universe than it is today (Lotz et al., 2010).

Considering the mass and age measurements for the XLSSC 122 members from the study done by Trudeau et al. (2022), we find that the red-sequence galaxies are more massive, older, bulge-dominated and have short characteristic times. On the other hand, the blue cloud galaxies are less massive and younger, with disturbed features. These results are consistent with the *Archaeological Downsizing* scenario, which states that stars in more massive galaxies tend to be older and to have formed at earlier epochs over shorter times, while disky galaxies tend to be less massive and generally have younger stellar populations (Fontanot et al., 2009). This trend observed in the local universe, is very much present in XLSSC 122 at $z = 2$.

The internal properties of galaxies have long been suggested to be highly dependent on the amount and distribution of their stellar mass (Kauffmann et al., 2004). As such, the latter play an important role in driving galaxy evolution. Our analysis finds that the mass and age of the cluster members are highly correlated. This correlation raises the question as to whether the morphology of the cluster members are determined mostly by the activity of its stellar population, or by how massive they are. Evidently, these two properties, are mutually dependent. For instance, older galaxies are likely to have accreted their mass through consecutive mergers, affecting their star formation histories and to then gradually evolve through secular processes into more relaxed structures over time, as their gas content is consumed (Merritt, 1999; Kipper et al., 2021). Alternatively, galaxies that are initially established with higher mass, result in an evolutionary path with faster and earlier suppression of the mass growth via star formation, causing a more drastic transition in terms of their morphology (Burkert & Naab, 2003). According to the partial Spearman rank correlation test, between the galaxy mass and morphological indices, removing the dependence in age, the latter scenario seems more plausible, where the mass is the main driver of the morphological evolution in the cluster. However this may not be the case for galaxies in the field.

We observe the morphology-density relation in the population of galaxies in XLSSC 122, whereby the red, more massive and bulge-dominated galaxies are found in the densest region of the cluster, in its center. This is also observed in galaxy clusters at

$1.4 < z < 1,7$ (Strazzullo et al., 2019). Additionally the possible mergers are found in the lower density regions of the cluster, closer to the outskirts. These observations relate to the fact that galaxy interactions leaving detectable merger features, are more frequent in low density regions where the velocity dispersions of the galaxies are comparable to their internal velocities, while environments with higher velocity dispersion associated with denser regions and tend to suppress the rate of galaxy interactions altogether (Dressler, 1980; Delaye et al., 2014).

However, we do not find a clear monotonic trend with the properties of the cluster members and their surface local density. This behaviour may be a result of not considering the 3-dimensional distribution of the galaxies. Thus better constraints on the de-projected positions of the cluster members, may reveal clearer evidence of the morphology density relation, and whether a threshold exists within the clusters where the morphological transition occurs.

Investigating the properties of field galaxies at the same epoch as XLSSC 122, reveals that the proportion of blue galaxies in the field is twice as large as in the cluster. The majority of the field galaxies are also bluer, which is the contrary to what is observed in the cluster. If the colour is used as a proxy for the star-formation activity of the galaxies, field galaxies can be considered to be generally more star-forming in nature than galaxies in the cluster over the same mass range. These differences suggest that cluster environments favour processes suppressing star formation (Moore et al., 1999; McCarthy et al., 2008) compared to the field. As a result, this imply that the stellar mass of galaxies may not be the only determinant of the internal properties responsible for the morphological evolution of galaxies. The surrounding mass in the environment where the galaxies grow, may be an equally important factor in dictating their evolutionary path. This conclusion was also reached in a previous study of the XLSSC 122 cluster, where more concentrated or bulge-dominated (in terms of Sérsic index) galaxies are found in the cluster than in the field (Noordeh et al., 2021).

By applying the Gini-M20 method on the field galaxies, we find that the 'main sequence' for the field population is much flatter than that of the galaxies in XLSSC 122. Following up on the proposition to adjust the classification thresholds depending on the redshift of the observed population, the environment in which the galaxies are found may also have an impact on the methods used. Additionally, dust lowers the Gini value significantly, which results in merger remnants from gas-rich interactions, which are more common at high redshifts, to not be detectable with Gini-M_{20} with boundaries defined using Equations 2.3.2.

Furthermore, we observe an excess of highly asymmetric blue galaxies, with large M_{20} values in the field compared to the cluster population. This further reinforces the idea that galaxy interactions is less frequent in dense regions than in the field, but also suggest that the cluster environmental processes result in the fading of the stellar disc structures, which is still detectable in field galaxies of comparable mass.

This excess of galaxies with high asymmetry values in the field may also explain the presence of high asymmetry galaxies in the S20 cluster, absent in XLSSC 122. Due to the limitations of using the photometric redshift and red-sequence selection method to determine cluster membership, the S20 sample is more likely to be contaminated by interlopers from the field.

The range of stellar masses of the red-sequence population in XLSSC 122 and the field show no significant difference. However, the blue field galaxies reach up to higher masses than in the cluster, suggesting that mass accretion through either *in situ* or *ex situ* star formation in XLSSC 122 is surpressed. Additionally, van der Burg et al. (2020) found evidence that environmental quenching efficiency is higher in more massive galaxies. One could imply that in the cluster, higher mass galaxies evolve more quickly towards red and bulge-dominated galaxies, than those in the field. Moreover, since the overall mass of galaxies within the cluster does not reach higher values than in the field, it is likely that mass growth within the virialised cluster is less significant. In other words, most of the galaxies hierachical growth through mergers and star formation, is likely to have occurred prior to the cluster's virialisation, when the environment was dense enough for galaxies to be in close proximity, but with lower velocity dispersions. Then, once the galaxies became bound within the cluster, the frequency of interactions as well as the star formation rates are lowered, which evidently inhibited their mass growth.

These observations are also consistent with an alternate downsizing effect: *Downsizing in time* scenario (Neistein et al., 2006). This describes the observation of the sites of active star formation, shifting from high mass galaxies at at earlier epochs to lower mass systems at lower redshifts. Interestingly, according to this scenario, the population of galaxies in XLSSC 122 appear to have similar properties to low redshift galaxy population (Strazzullo et al., 2005; Cerulo et al., 2017; Vulcani et al., 2011). That similarity would provide further evidence, that galaxy clusters, provide an environment within which galaxies evolve at a faster rate into the galaxy population we observe in the local universe, and that XLSSC 122 is a mature galaxy cluster, where the conditions leading to the morphological transition of its members has occurred

prior to the epoch of observation.

According to the study done by Trudeau et al. (2022) on the star formation history of the galaxies in XLSSC 122, the redder and oldest cluster members had accreted most of their mass, prior to the assembly of the cluster. In addition, their short characteristic times suggest that it is unlikely for these galaxies to have experienced more than one epoch of star formation. Our morphological analysis of the red-sequence galaxies are consistent with the conclusion from this previous study, as those galaxies are left with structures presenting no strong indication of star forming disks.

On the other hand, the blue galaxies younger than 1 Gyr have characteristic times shorter than 0.2 Gyr or ongoing star formation (Trudeau et al., 2022). Indeed, the presence of disks with asymmetric structures, which may mark regions of star formation, that we observe in this study agree with such expectations. One could argue, that the conditions triggering star formation in this population of the XLSSC 122 members are unlikely to have occurred prior to the virialisation of the cluster at an epoch corresponding to $z \sim 2.8$ (i.e. 1 Gyr before $z = 2$, Willis et al., 2020), for them to still be morphologically detectable.

Chapter 3

Perspectives on the Accretion History of XLSSC 122 from Cosmological Simulations

The results of the morphological analysis of the HST images of XLSSC 122 support the idea that this system represents a mature galactic environment at a large lookback time. The clear red-sequence populated by bulge-dominated galaxies appear strongly similar to the populations of lower redshift ($z < 1$) galaxy clusters. We next turn to the properties of simulated high-redshift clusters in an attempt to further understand the observed properties of XLSSC 122 and its possible assembly history.

3.1 Cosmosim

To investigate the assembly history of the galaxy members of XLSSC 122, we use the publicly available database, Cosmosim[1], which provides results from cosmological simulations performed within different projects. Similar to data from large surveys such as the Sloan Digital Sky Survey (SDSS, York et al., 2000), the data products from the simulations are made accessible through SQL (Structured Interface Query Language) queries. Researchers can then retrieve and use data subsets of interest.

From the projects available, we use results from *MultiDark-Plank* (Riebe et al., 2013; Klypin et al., 2016), a collection of dark matter only cosmological simulations. They are carried out with the L-Gadget-2 code (Springel, 2005), which uses the

[1] https://www.cosmosim.org

Table 3.1: Simulation Specifications.

Simulation	Box^1	$Particles^2$	m_p	ϵ	Ω_M^3	Ω_B^3	Ω_Λ^3	σ_8	n_s	H_0
MDPL2	1.0	3840^3	1.5×10^9	5	0.307	0.048	0.693	0.829	0.96	67.8
SMDPL	0.4	3840^3	9.6×10^7	1.5	0.307	0.048	0.693	0.829	0.96	67.8

1 the size of the simulated box in h^{-1}Gpc
2 the number of particles
3 the cosmological parameters adopted
m_p: The mass per simulation particle in $h^{-1}M\odot$
ϵ: the Plummer equivalent gravitational softening length in h^{-1}kpc
σ_8: the clustering at $8h^{-1}$Mpc
n_s: the spectral index
H_0: the Hubble constant in km/s/Mpc

N-body method, following a collisionless fluid to represent dark matter particles. Though these dark matter (DM) only simulations do not mimic the evolution of baryons, they provide large-scale representations of the universe, while keeping a high enough resolution to retain reliable information about the properties of haloes such as the halo mass, virial radius, maximum circular velocity, and density profile (Klypin et al., 2016).

For the scope of this study, only considering dark matter interactions is sufficient for answering questions regarding the halo and subhalo mass assembly history. We use data from 2 particular simulation suites, *MDPL2* and *SMDPL* (Klypin et al., 2016). *SMDPL* has a simulation box length less than half that of *MDPL2*, which though results in a smaller sample of halos, *SMDPL* achieves a better mass resolution, as shown in Table 3.1.

More specifically, we consider haloes identified using Rockstar (Robust Overdensity Calculation using K-Space Topologically Adaptive Refinement) halo finder algorithm (Behroozi et al., 2013). Rockstar which uses adaptive hierarchical refinement of a friends-of-friends approach (Davis et al., 1985), in six phase-space dimensions and one time dimension, allowing for accurate extraction of subhalos.

The merger history resulting from the cosmological simulations is arranged into merger trees. As shown in Figure 3.1, a particular halo at redshift $z = 0$ is represented as the *tree root* (at the top of the figure). The branches going down the figure link to the progenitor haloes at higher redshifts, represented by the nodes (Riebe et al., 2013). The most massive progenitors at each timestep are shown on the *main branch*. The code also identifies overlapping spheres containing a given overdensity, corresponding to halos and their respective subhalos at each timestep.

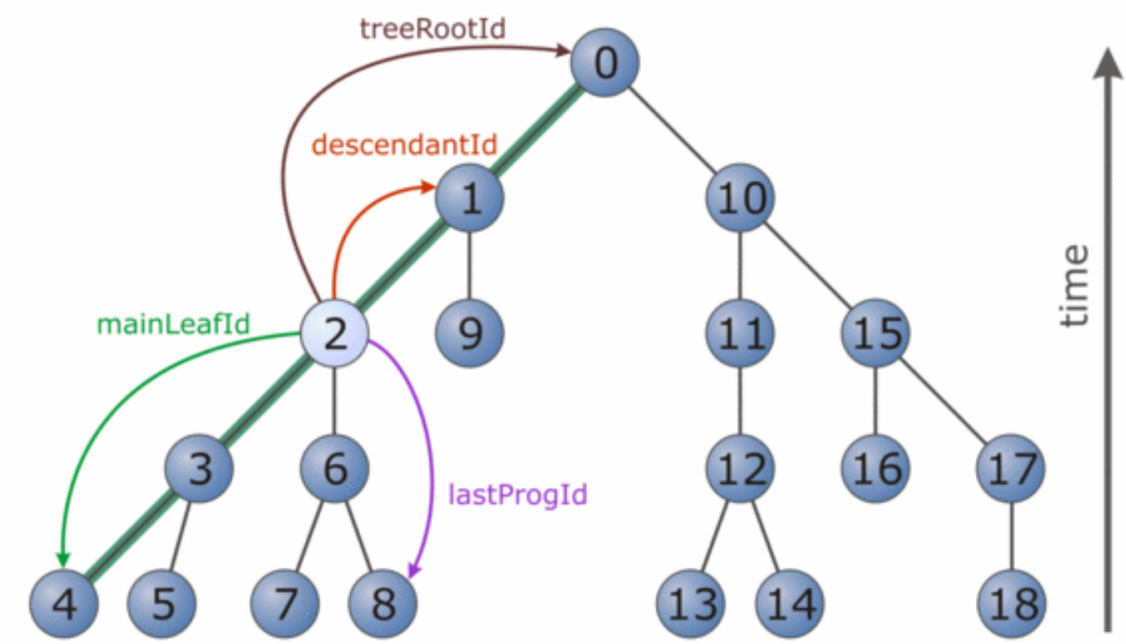

Figure 3.1: Figure 1 from Riebe et al. (2013). Merger tree of a halo at redshift $z = 0$, labelled as the *treeRootId* at the top node. Branches reach backwards in time, linking to progenitors one timestep prior. The most massive progenitors are arranged on the leftmost branch, along the *main branch*.

In this study, XLSSC 122-like halos were extracted from the simulation results by applying the criteria that their M_{500} masses are between the 1σ confidence interval ($\pm 1.5 \times 10^{13}$) from the mass of XLSSC 122, within the timestep of the simulation corresponding to $z \sim 1.98$. The resulting sample consists of 491 and 54 XLSSC 122-like halos from *MDPL2* and *SMDPL*, respectively. Figure 3.2 shows the positions of the selected XLSSC 122-like clusters from the 2 simulation suites. Within every XLSSC 122-like halo in both samples, we select their 30 most massive subhalos, which provides a comparable sample to the observed brightest XLSSC-122 galaxy members (Fig.2.2). We then extract the *main branch* progenitors of each of these subhalos to recover the merger history of the subhalos for every XLSSC 122-like cluster.

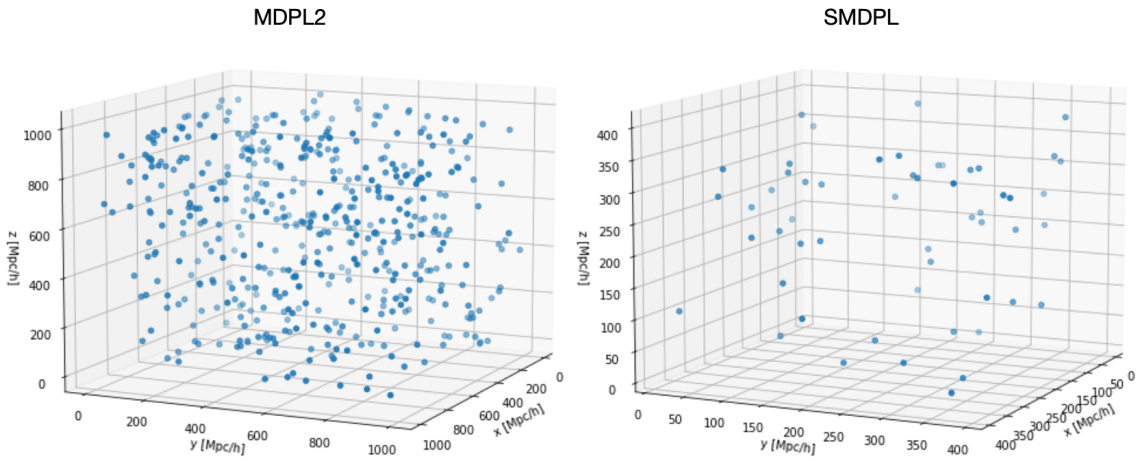

Figure 3.2: Box size and position of XLSSC 122-like clusters in *MDPL2* (*left*) and *SMDPL* (*right*).

Figures A.4 and A.5 (Appendix A.4) show the mass accretion history for the 30 most massive subhalos from a random XLSSC-122 like halo, extracted from *MDPL2* and *SMDPL*, respectively. Since *SMDPL* has a smaller box size, lower mass subhalos are more accurately resolved than *MDPL2*. Therefore, in the following steps of this study, we present results from *SMDPL*, as the larger volume does not provide additional information.

The following SQL queries are used for the extraction of the cluster haloes, their corresponding subhalos and progenitors from *SMDPL*:

Select XLSSC 122-like haloes at z=2 (snapnum=39):

```
SELECT * FROM smdpl.rockstar WHERE snapnum = 39
AND m500c > 4e13 AND m500c < 8e13
ORDER BY mvir DESC
```

Extract subhaloes for one XLSSC 122-like halo:

```
SELECT *
FROM smdpl.rockstar WHERE upid=cluster_halo_id
ORDER BY mvir DESC
```

Find mainleaf progenitors of a subhalo:

```
SELECT p.* FROM smdpl.rockstar AS p,
(SELECT depthfirstid, mainleaf_depthfirstid,
lastprog_depthfirstid FROM smdpl.rockstar
WHERE rockstarid=subhalo_id)
AS mycl WHERE p.depthfirstid
BETWEEN mycl.depthfirstid AND mycl.mainleaf_depthfirstid
ORDER BY p.snapnum
```

3.2 Merger Selection

To extract instances of significant merger events during the evolution of the subhalos, we use a selection based on measurements from their mass growth curves. Among the information available for the halos in the database, we use the halo mass accretion rate averaged over the past 1 and 2 virial dynamical times (MaxAcc1tdyn and MaxAcc2tdyn, Klypin et al., 2016). We consider the timestep when the subhalo experienced the highest mass accretion rate, to mark the period with significant merging events between $z = 2$ and $z = 3$.

Alternatively, we calculate the mass growth rate from the instantaneous slope of the mass growth curve of the subhalos for each subsequent timestep, normalised with respect to their final $z = 2$ mass. In other words, the fraction of the subhalo $z = 2$ mass gained per timestep. Similarly, we consider the maximum rate between $z = 2$ and $z = 3$ to represent events of major merging interactions. Both measurements provide appropriate representations of the trends observed in the mass growth curve. We focus on finding merger events up to $z = 3$ since it is unlikely for features resulting from interactions prior to $z = 3$ to be recognised by $z = 2$, as discussed previously.

Along with the aforementioned merger event indicators, on the mass growth curves in Figure 3.3, we also show two other measurements available from ROCKSTAR[2]: the timestep for the last major merger with mass ratio > 0.3, and the timestep at which satellites were accreted. However, we do not consider these measurement further for the analysis as they tend to mark events outside of the range of interest. Only 41% of all subhaloes have their last major merger occurring between z=2 and z=3 (Fig.A.6).

[2]https://doi.org/10.17876/cosmosim/smdpl/001

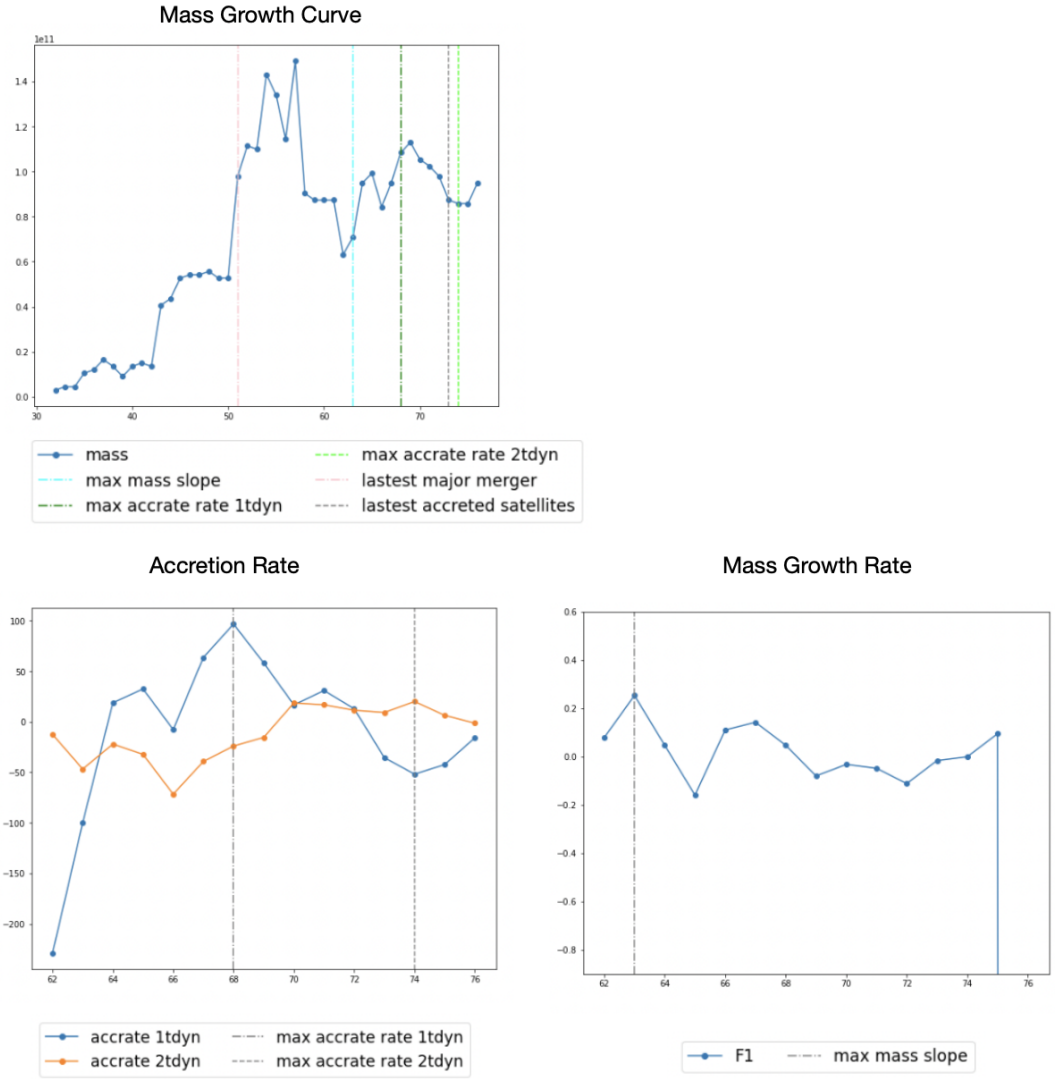

Figure 3.3: *Top:* Mass growth curve of a random subhalo from a random XLSSC 122-like cluster halo from *MDPL2*. *Bottom Left:* Accretion rate measurements for the progenitors of the subhalo between $z = 2$ and $z = 3$. *Bottom Right:* The normalised slope of the mass growth curve for the subhalo between $z = 2$ and $z = 3$. Additionally, measurements for the *latest major merger* and *latest accreted satellites* are also shown.

3.3 Comparison to Observations

After extracting the snapshots for the events described in the previous section, for each of the 30 subhalos in each of the XLSSC 122-like halos, the bins for the distribution of merger events between $z = 2$ and $z = 3$ are averaged to represent the number of merger events occurring during the evolution of a typical XLSSC 122-like galaxy

cluster. In other words, we determine the average merger rate within the cluster at each timestep. We show the distribution in terms of the lookback time from $z = 2$, Δt in Figure 3.4, where we find an average of 6 to 10 merger events occuring within 1 Gyr before the epoch of observation. This observation agrees for all merger event indicators and suggests that the epoch at $z \sim 3$ (at 1.3 Gyrs prior to z=2), may mark a period of interactions between the progenitors of the XLSSC 122 members. These interaction may then have resulted in major merger remnants features or the triggering of star formation, observed as the 10 disturbed members from the photometric analysis of XLSSC 122 (namely ID 146, 240, 434, 454, 455, 554, 604, 726, 808 and 1065).

As discussed in Chapter 2.5, the 6 disturbed members classified using the C-A plot may be remnants of gas-rich interactions which can be detected up to approximately 1 Gyr after the coalescence of their nuclei (Lotz et al., 2008a), and in Section 2.4.3, we find that the oldest stars in these galaxies have ages less than 1 Gyr. These point further strengthens the idea that the morphologies of the disturbed members of XLSSC 122 can be explained by merging events occurring around $z = 3$, which may relate to the period following the assembly of the cluster (Willis et al., 2020).

A peak in the average number of merger events is also observed at $\Delta t \sim 1$ Gyr. This period may mark the time at which the progenitors were at the latest stage of their interaction.

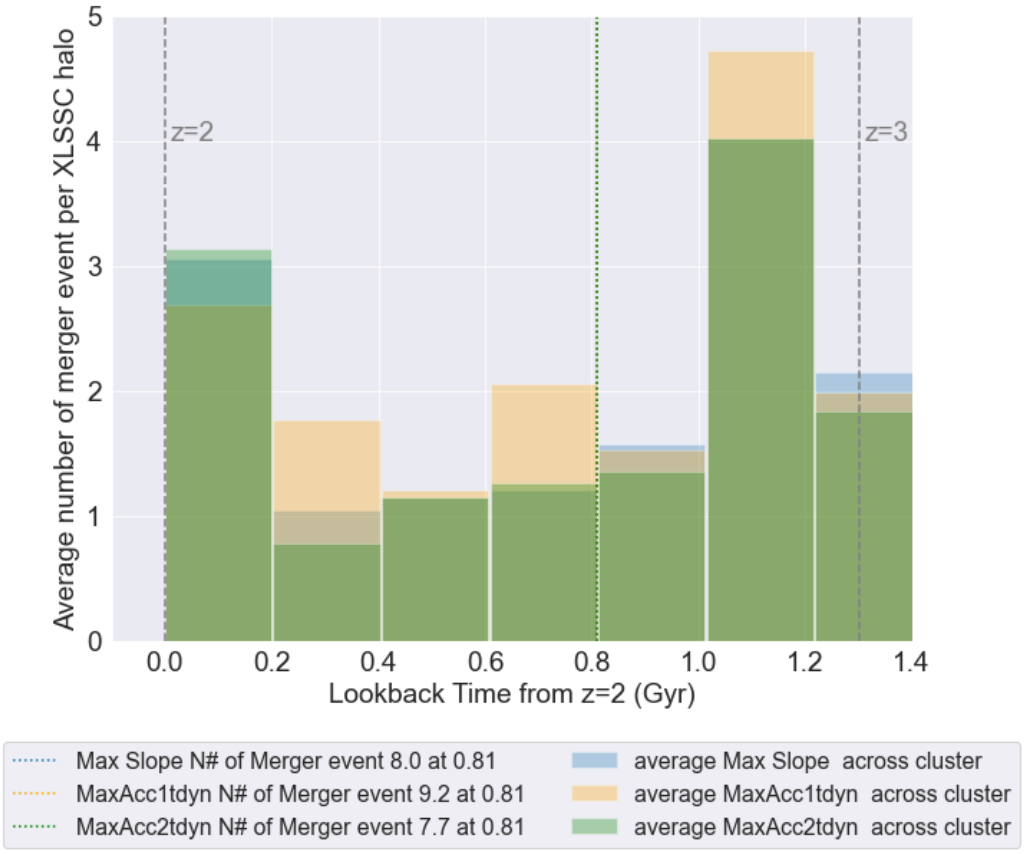

Figure 3.4: Distribution of merger events occurring in a typical XLSSC 122-like cluster between $z = 2$ and $z = 3$.

We also express the time frame of the merger events in terms of the ratio of the lookback time to the merger event, Δt to the halo's dynamical timescale, t_{dyn} at the virial radius in the snapshot of the merger event (Boylan-Kolchin et al. (2009), Fig.3.6). The halo's dynamical timescale, t_{dyn} represents the fastest time scale over which a galaxy moving through an extended halo loses its momentum and hence it determines how quickly two galaxies can merge after the merging of their haloes. These values can be calculated by:

$$\mathrm{t}_{dyn} = \frac{r_{vir}}{V_{circ}} = \sqrt{\frac{r_{vir}^3}{GM_{vir}}},$$

$$\text{Since, } M_{vir} = \frac{4\pi}{3} r_{vir}^3 \rho_{vir} \text{ and } V_{circ} = \sqrt{\frac{GM_{vir}(<r)}{r}}$$

$$\therefore t_{dyn} \propto \rho_{vir}^{-\frac{1}{2}},$$

where r_{vir} is the virial radius, V_{circ} is the circular velocity at r_{vir}, and ρ_{vir} is approximately 200 times ρ_c, the critical density of the universe at that epoch. We show the dynamical times calculated within r_{vir} and r_{500} of the progenitor haloes at the time marking significant merger events in Figure 3.5.

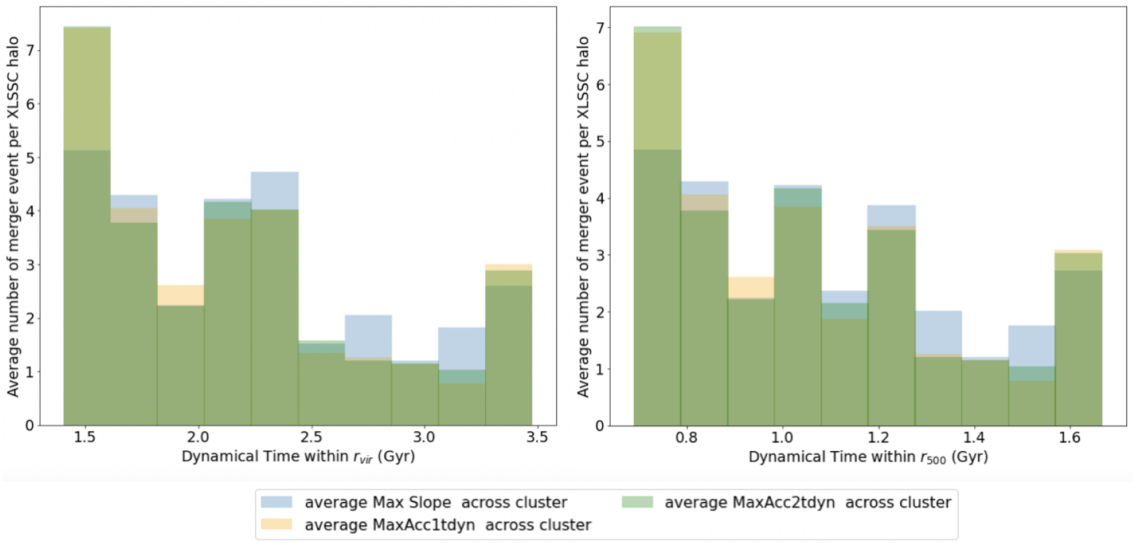

Figure 3.5: Distribution of the dynamical times of halaoes at merger events occurring in a typical XLSSC 122-like cluster between $z = 2$ and $z = 3$.

We find that 6 to 10 merger events occurred within $\Delta t < t_{dyn}$. The mode of the distribution of the merger events also occurs at $\Delta t < t_{dyn}$, suggesting longer dynamical times for the progenitors during the merger events. Longer t_{dyn} results in

disturbed structures persisting over longer period of time and thus, long lived merger signatures (Mihos & Hernquist, 1996).

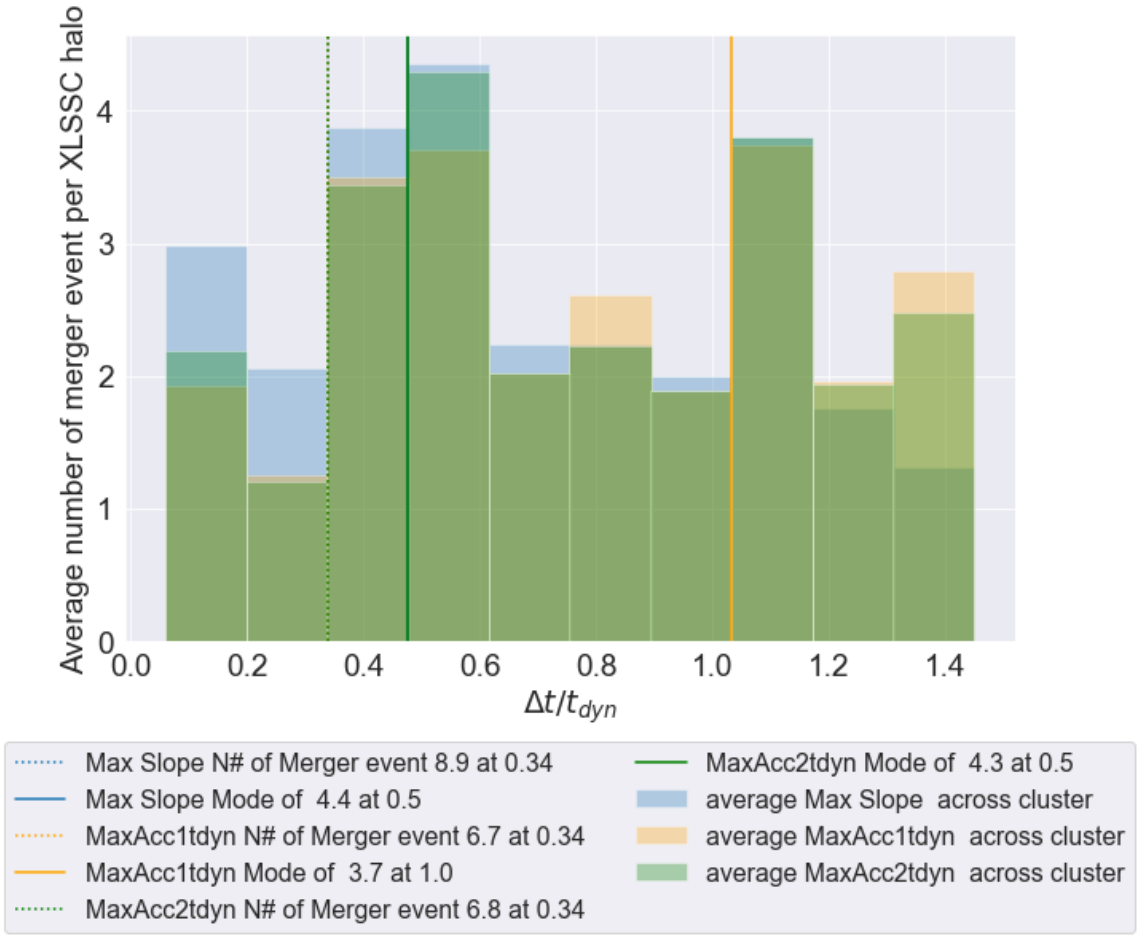

Figure 3.6: Distribution of merger events occurring in a typical XLSSC 122-like cluster between $z = 2$ and $z = 3$, in terms of the ratio of Δt to t_{dyn}.

Considering the relationship between the critical density and the dynamical time, and the fact that baryonic systems are denser than the ones resulting from the collisionless particles in dark matter simulations, we look at the dynamical times at the radius within which the density is 500 times the critical density of the universe ($t_{dyn500c}$). This choice results in smaller radii, thus larger densities, which aim to better represent the dynamical times observed in baryonic interactions. In Figure 3.7, we find that 6 to 10 merger events have $\Delta t > t_{dyn500c}$. The mode of the distribution is also at $\Delta t > t_{dyn500c}$ for events indicated using the maximum mass growth slope and the maximum accretion rate averaged over 1 dynamical time. This indicate that the

mergers may be occurring past the time frame for the two progenitors to coalesce. Therefore, would correspond to the merger stages that can be detected using the methods presented in Section 2.3.2. The conclusions resulting from analysing t_{dyn} still hold.

To further understand the conditions during the interaction of the subhaloes within XLSSC 122-like clusters, we look at the positions where the merger events occurred with respect to the virialised cluster at $z = 2$. Figure 3.8 shows the positions of the subhalo progenitors of 4 randomly selected XLSSC-like haloes. In Figure 3.9 we represent the average distribution of the clustercentric distance from the center of a typical XLSSC 122-like halo at $z = 2$ to the position of the merger events. We find that the majority of the merging events occurred outside of the virial radius of the cluster at $z = 2$, admittedly prior to the galaxies becoming part of the cluster, during the protocluster stage. This tendency is consistent with the observed population of

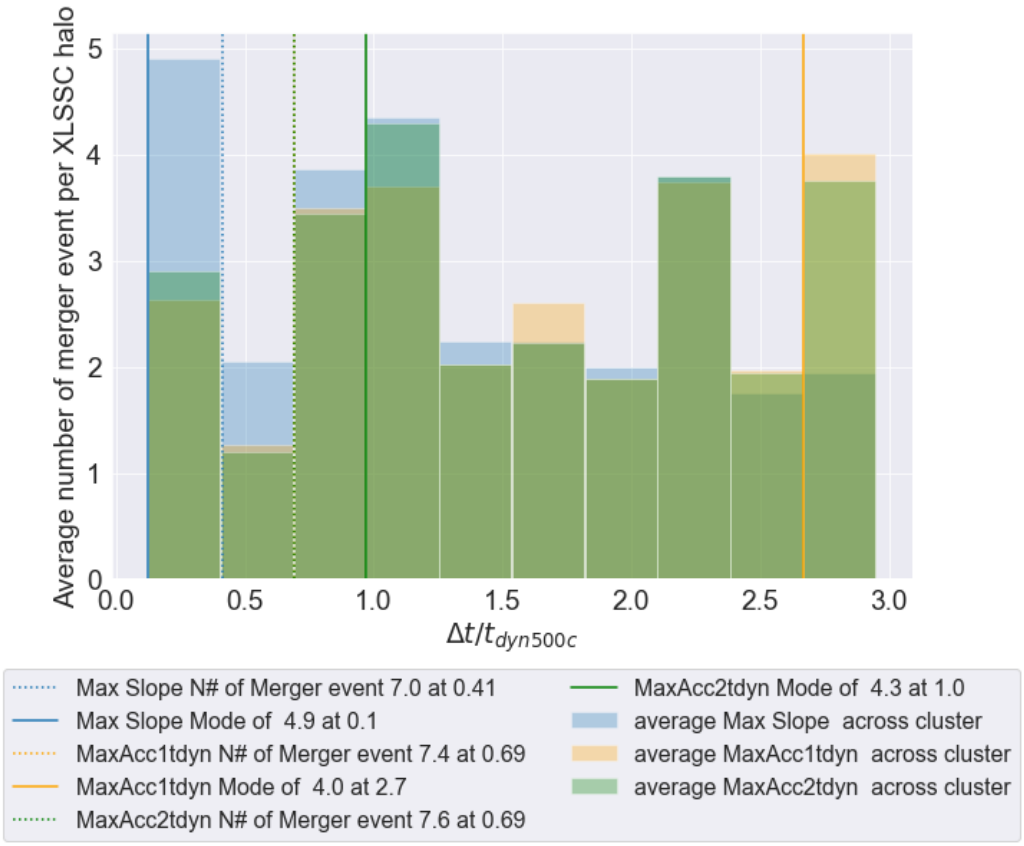

Figure 3.7: Distribution of merger events occurring in a typical XLSSC 122-like cluster between $z = 2$ and $z = 3$, in terms of the ration of Δt to $t_{dyn500c}$.

disturbed XLSSC 122 members found generally at larger radii ($R_{BCG} > 0.4$Mpc).

We also show the distribution of the velocity dispersions of the subhaloes at the time of the merger events, from the information available in ROCKSTAR (Fig.3.10). According to the simulation, the majority of the merger events occur when the velocity dispersions of the halo members are less than 200 km/s. For context, the internal velocity of galaxies ranges from 200 to 400 km/s (Veale et al., 2018). The typical velocity dispersion of massive cluster around $z = 2$ is approximately 600 km/s (Werner et al., 2023) and the average in the Coma cluster has been measured to be around 1000 km/s (Zwicky, 1937). This high velocity dispersion further suggests that merger events in clusters such as XLSSC 122 occurred prior to their virialisation of their host

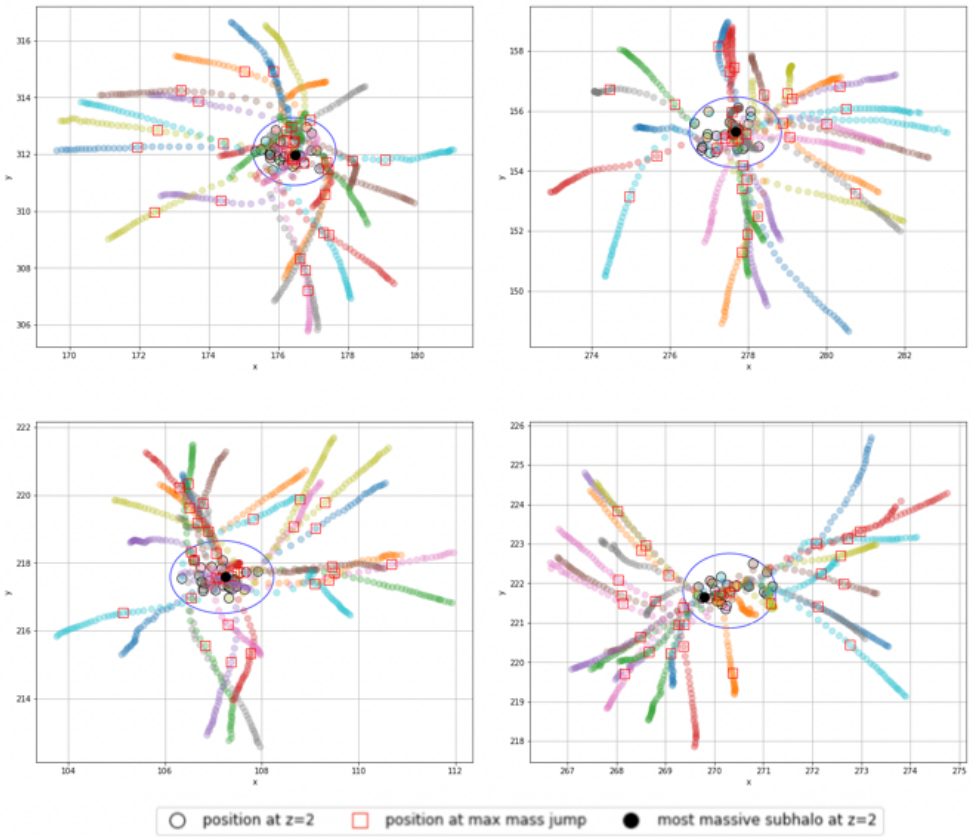

Figure 3.8: The positions of the progenitors of the 30 most massive subhaloes of 4 XLSSC 122-like halo at each timestep of the *SMDPL* simulation suite. The blue circle shows the virial radius of the XLSSC 122-like halo at z=2. The black circles mark the positions of the subhaloes at z=2. The red squares mark the positions of the progenitors when the subhalo experienced a significant merging event indicated by the maximum slope of the mass growth curve.

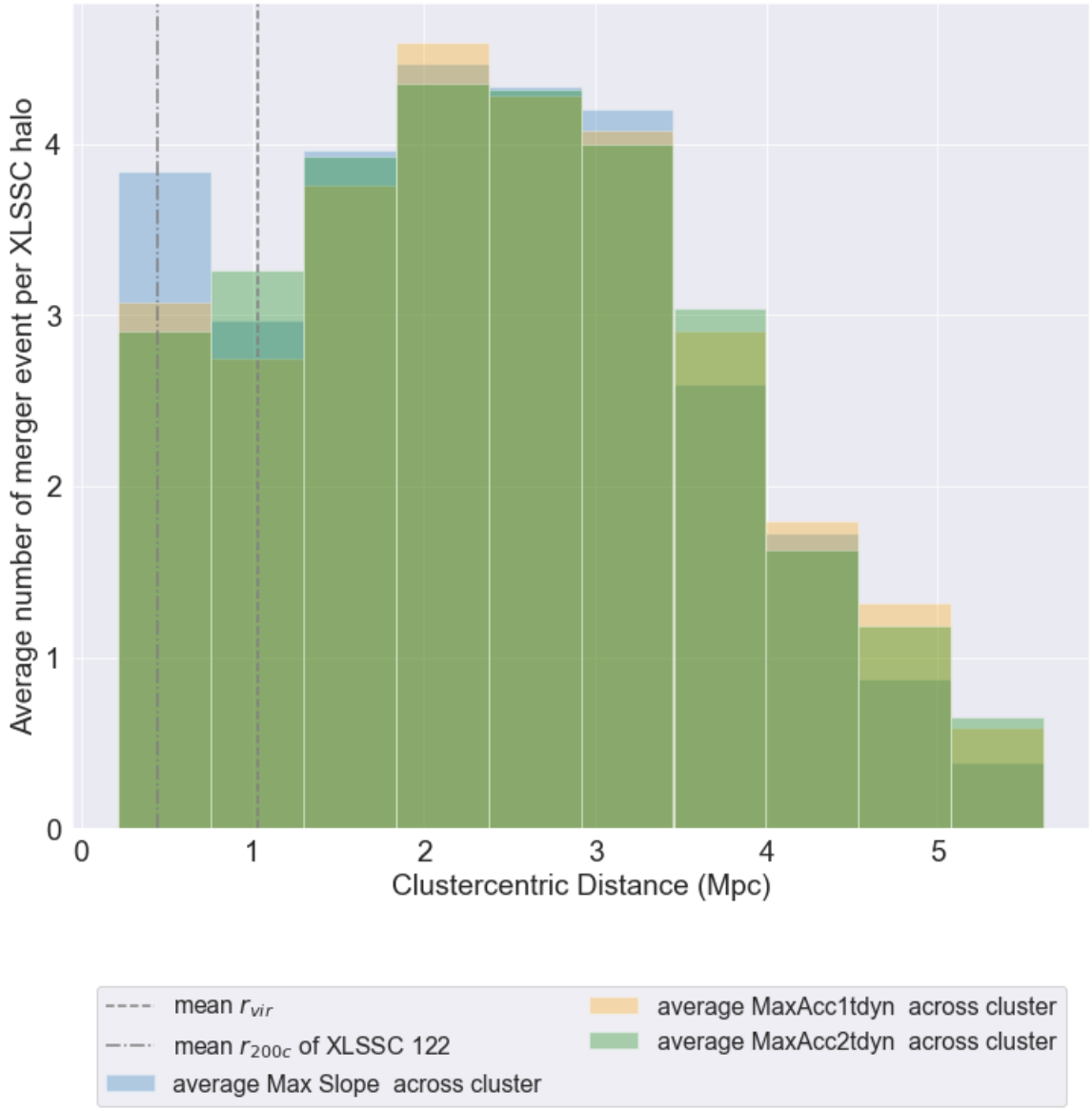

Figure 3.9: Distribution of the position of merger events occurring in a typical XLSSC 122-like cluster between $z = 2$ and $z = 3$, in terms of the radial distance to the center of the cluster at $z = 2$. The grey dashed line shows the mean virial radius of the simulated XLSSC 122-like clusters and grey the dashed-dotted line shows the r_{200c} of XLSSC 122.

clusters, when the environment was more favourable for galaxy interactions.

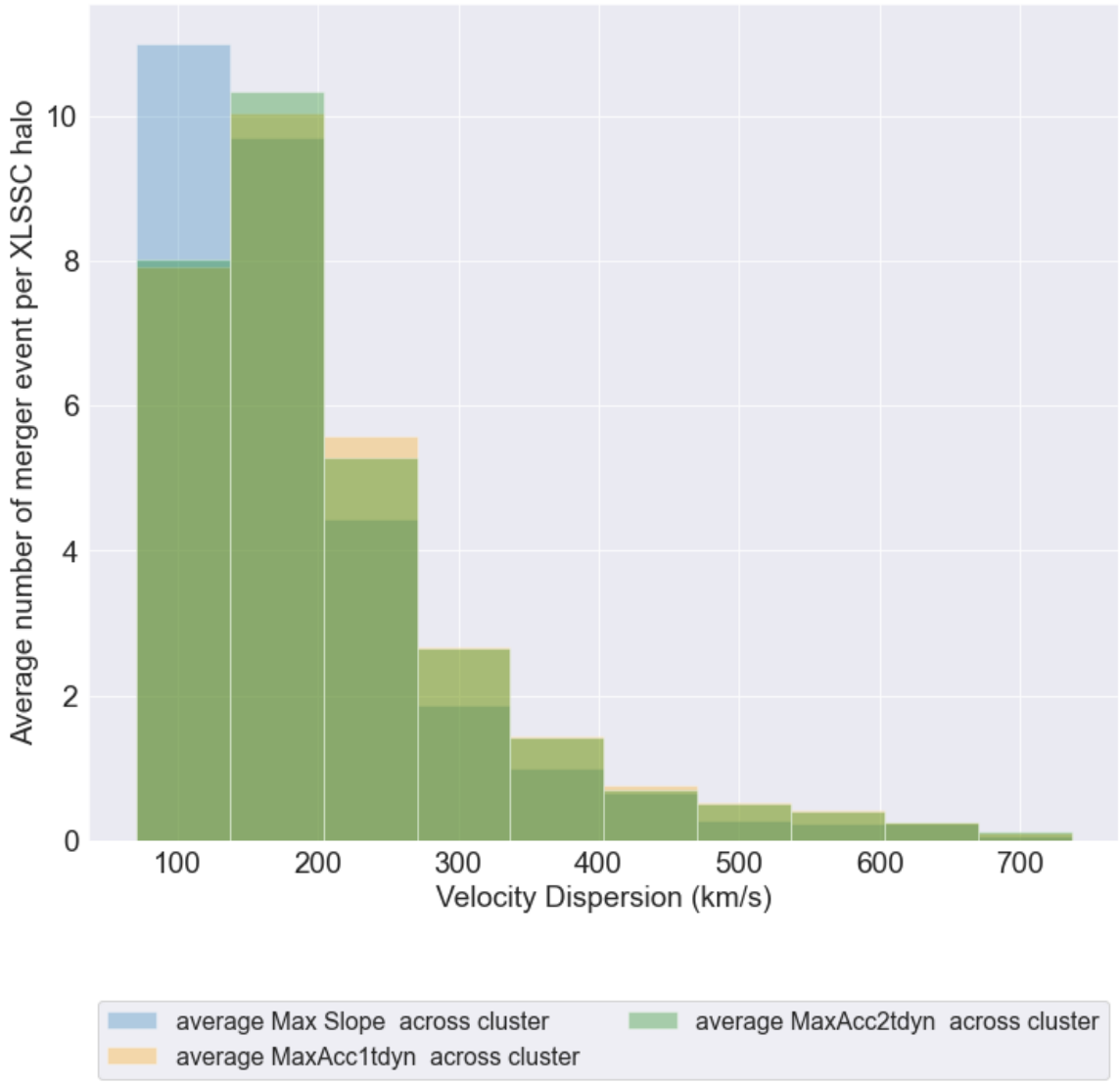

Figure 3.10: Distribution of the velocity dispersion of haloes at the time merger events occurring in a typical XLSSC 122-like cluster between $z = 2$ and $z = 3$.

Chapter 4

Conclusions

We performed a morphological analysis of HST WFC3 images of XLSSC 122, a massive cluster at a redshift of 2. Our observations confirm the presence of a well established population of red and bulge-dominated galaxies compared to the field. We also identify both visually and quantitatively, cluster members with disturbed structures indicating remnants of galaxy interactions, which are mainly found in the outskirts and less dense regions of the cluster.

Additionally the internal properties of the different populations within the cluster are consistent with galaxies observed in the local universe. Namely, the bulge-dominated galaxies of XLSSC 122 are typically redder, older, and more massive, while the disky galaxies are typically to be star forming, bluer, less massive and younger. However when XLSSC 122 is set side by side to the population of galaxies in the field, we find blue field galaxies with masses comparable to the most massive red-sequence galaxies in the cluster, indicating that even at higher mass the galaxies in the field continue growing via star formation.

Comparing the members of the XLSSC 122 to those of 4 other massive clusters at slightly lower redshifts, reveals no significant differences between the proportions of the different morphological classifications in their respective memberships. In addition, it may be fair to conclude that the environments within massive clusters present uniform conditions resulting in similar populations of galaxies, since studies of low-redshift galaxy clusters also show comparable properties to those within high redshift environments presented in this work. Following the assumption that the population of galaxies in a cluster at an epoch corresponding to a lookback time of 10.3 Gyr (at z=2), is similar to the populations observed in low redshifts clusters in the local universe (Courtois et al., 2013), we presume that the evolution in these environments

slows down significantly between these epochs. This supposition may be related to the overall downturn in star formation observed since $z = 2$ (Madau & Dickinson, 2014; Franco et al., 2020).

It is however important to note that the morphological indices are subject to uncertainties due to the signal-to-noise ratios of the images. Additionally, the bands used to observe XLSSC 122 may be biased towards certain types of galaxy populations. For instance, F814W, which is used in the field observations, is efficient at probing the star-forming galaxy population. Therefore images of XLSSC 122 in F814W band may give a different perspective on the population of the cluster members. As well as deeper images with higher resolution of the cluster can further confirm the accuracy of the morphological classification.

We furthered our understanding of the processes leading to the formation of XLSSC 122, by examining the properties of the progenitors of subhalos within a sample of XLSSC 122-like haloes at $z = 2$, from the results of dark matter only simulations. The mass accretion history reveals events of high merger rates around redshift $z = 3$, approximately 1.2 Gyr prior to the epoch of observation, at distances higher than the virial radius of the XLSSC-like cluster and in regions of lower velocity dispersions. These results from large-scale-structure simulations, further insinuate that the disturbed galaxy members in XLSSC 122 may be remnants from galaxy interactions prior to the virialisation of the cluster.

The analyses presented in this work paint the following picture about the morphological evolution of the XLSSC 122 cluster members. Starting in the field, galaxies infall onto group structures in the outskirts of clusters (Bahé et al., 2013), where they have lower velocity dispersions and can accrete mass through frequent interactions and mergers, inducing star formation. The conditions in these regions are such that star formation is sustained, perhaps fueled by gas-rich mergers or by gas from cosmic filaments, via the mechanism termed as 'pre-processing'. Once the galaxies infall into the virialised cluster, the merger rate decreases due to the higher velocity dispersions of galaxies in denser regions. The galaxies are also subject to the cluster environmental processes, such as harassment, whereby the frequent interactions cause tidal stripping, disrupting the disk structure of the interacting galaxies (Larson et al., 1980; Balogh et al., 2000). Additionally, the high velocity of the galaxies with respect to the ICM gives rise to ram pressure stripping, which refers to the removal of galaxies cold gas reservoir (Gunn & Gott, 1972). The combination of these phenomena, contribute to suppressing the star formation rates, depleting the gas content and erasing

the disc structures of galaxies, resulting in the red-sequence, bulge-dominated population observed in cluster cores arises, which subsequently grows in mass through dissipationless mergers between gas-poor spheroids. These mergers, however, which are unlikely to affect the morphology of the remnants or trigger further star formation (Boylan-Kolchin et al., 2005).

One way to test this picture, is through further observations of the outskirts of XLSSC 122 at larger radii, where we can possibly probe the region where the various mechanisms may become significant as galaxies get caught by the cluster, or the region linking the transition from the field, to groups, where star formation is supported. Such studies will soon be possible with new expected images of the outskirts of XLSSC 122 out to twice its virial radius, as well as in the ACS F814W band imaging scheduled in cycle 30 of the Hubble Space Telescope (Fig4.1, Canning et al., 2022).

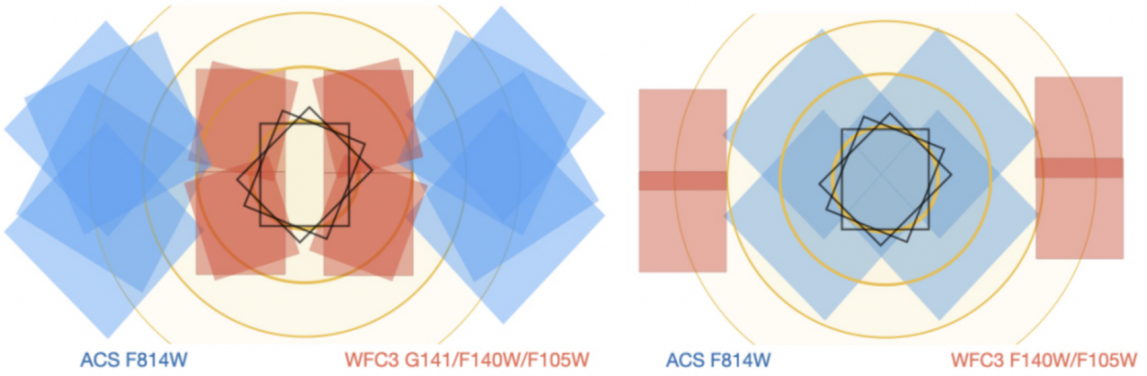

Figure 4.1: An illustration of the observation setup for the observation of XLSSC 122 in cycle 30 of HST. The black frame shows the coverage of the images used in this study. The orange circles outlines 1, 2, 3 and 4 4 r_{vir}. The ACS F814W imaging are shown in blue and will be taken in parallel with the WFC3 observations shown in red.

The evolution of the oldest galaxies in XLSSC 122 is suspected to have followed different evolutionary paths from the rest of the cluster's galaxy population (De Lucia & Blaizot, 2007). Their formation hypothetically originate from the 'primordial collapse' of matter within dark matter overdensities in the early universe (Stasielak et al., 2007). Subsequently, they would have followed more secular evolutionary paths to become the massive bulge-dominated galaxies we observed, due to the disparate constitution and structure of the universe following the Big Bang and Inflation period. Novel observations using the James Webb Space Telescope (JWST) can provide us

with more insight on the origin of the red-galaxies in XLSSC 122, by unveiling the properties of galaxies in protoclusters at even higher redshifts.

Additionally our studies and those alike are limited, since the processes involving the active galactic nuclei have not been considered, and these may also be affected by galaxy interactions and produce structural features in the hosts (Dubois et al., 2016; Zhong et al., 2022). Spectroscopy from JWST of these populations may help clarify basic issues about nebular line emission and the degree to which it has affected the photometric analyses that have been carried out to date.

High-resolution cosmological hydrodynamic simulations of large volumes which considers baryonic processes are promising tools to gain further insights on the origin of galaxy clusters. The computational cost for these kind of simulations, however, is currently prohibitively high. Furthermore, they would require the input of cosmological initial conditions about processes affecting the baryons, such as the star formation, radiative cooling, and supernova feedback, that are still poorly constrained. Forthcoming advancements in high-redshift spectroscopic observations and improved efficiencies of large-scale baryonic simulations hold significant promise to uncover more about the formation of clusters such as XLSSC 122 and subsequently clusters found in the local universe.

Bibliography

Abell G. O., 1958, , 3, 211

Abraham R. G., van den Bergh S., Glazebrook K., Ellis R. S., Santiago B. X., Surma P., Griffiths R. E., 1996, , 107, 1

Abraham R. G., van den Bergh S., Nair P., 2003, , 588, 218

Bahé Y. M., McCarthy I. G., Balogh M. L., Font A. S., 2013, , 430, 3017

Baldry I. K., Balogh M. L., Bower R. G., Glazebrook K., Nichol R. C., Bamford S. P., Budavari T., 2006, Monthly Notices of the Royal Astronomical Society, 373, 469

Balogh M. L., Navarro J. F., Morris S. L., 2000, , 540, 113

Balogh M. L., Baldry I. K., Nichol R., Miller C., Bower R., Glazebrook K., 2004, The Astrophysical Journal, 615, L101

Barton E. J., Geller M. J., Kenyon S. J., 2000, , 530, 660

Behroozi P. S., Wechsler R. H., Conroy C., 2013, The Astrophysical Journal, 770, 57

Bernardi M., Shankar F., Hyde J. B., Mei S., Marulli F., Sheth R. K., 2010, , 404, 2087

Bershady M. A., Jangren A., Conselice C. J., 2000, , 119, 2645

Bertin, E. Arnouts, S. 1996, Astron. Astrophys. Suppl. Ser., 117, 393

Blanton M. R., Moustakas J., 2009, , 47, 159

Böhringer H., et al., 2002, , 566, 93

Boylan-Kolchin M., Ma C.-P., Quataert E., 2005, , 362, 184

Boylan-Kolchin M., Springel V., White S. D. M., Jenkins A., Lemson G., 2009, , 398, 1150

Brammer G., 2019, Grizli: Grism redshift and line analysis software, Astrophysics Source Code Library, record ascl:1905.001 (ascl:1905.001)

Brammer G. B., et al., 2012, , 200, 13

Brinchmann J., et al., 1998, The Astrophysical Journal, 499, 112

Burkert A., Naab T., 2003, in Contopoulos G., Voglis N., eds, , Vol. 626, Galaxies and Chaos. pp 327–339, doi:10.1007/978-3-540-45040-5˙27

Buta R. J., 2013, in Oswalt T. D., Keel W. C., eds, , Vol. 6, Planets, Stars and Stellar Systems. Volume 6: Extragalactic Astronomy and Cosmology. p. 1, doi:10.1007/978-94-007-5609-0˙1

Canning R. E. A., et al., 2022, Caught in the act: Galaxy quenching beyond the core of a redshift two galaxy cluster?, HST Proposal. Cycle 30, ID. #17172

Cantale N., et al., 2016, , 589, A82

Capak P., et al., 2007, , 172, 99

Carnall A. C., McLure R. J., Dunlop J. S., Davé R., 2018, , 480, 4379

Cavaliere A. G., Gursky H., Tucker W. H., 1971, , 231, 437

Cerulo P., et al., 2017, , 472, 254

Chester C., Roberts M. S., 1964, , 69, 635

Conselice C. J., 2003, , 147, 1

Conselice C. J., 2014, , 52, 291

Conselice C. J., Bershady M. A., Jangren A., 2000a, , 529, 886

Conselice C. J., Bershady M. A., Jangren A., 2000b, , 529, 886

Courtois H. M., Pomarède D., Tully R. B., Hoffman Y., Courtois D., 2013, , 146, 69

Cowan N. B., Ivezić Ž., 2008, , 674, L13

Davis M., Efstathiou G., Frenk C. S., White S. D. M., 1985, , 292, 371

De Lucia G., Blaizot J., 2007, , 375, 2

Delaye L., et al., 2014, , 441, 203

Dressler A., 1980, , 236, 351

Driver S. P., Windhorst R. A., Ostrander E. J., Keel W. C., Griffiths R. E., Ratnatunga K. U., 1995, , 449, L23

Dubois Y., Peirani S., Pichon C., Devriendt J., Gavazzi R., Welker C., Volonteri M., 2016, , 463, 3948

Ellison S. L., Simard L., Cowan N. B., Baldry I. K., Patton D. R., McConnachie A. W., 2009, , 396, 1257

Ferreras I., et al., 2021, Experimental Astronomy, 51, 729

Fontanot F., De Lucia G., Monaco P., Somerville R. S., Santini P., 2009, , 397, 1776

Forman W., Kellogg E., Gursky H., Tananbaum H., Giacconi R., 1972, , 178, 309

Franco M., et al., 2020, , 643, A30

Gavazzi G., Boselli A., Cortese L., Arosio I., Gallazzi A., Pedotti P., Carrasco L., 2006, , 446, 839

Gini C., 2005, Metron, 63, 3

Gladders M. D., Yee H. K. C., 2000, , 120, 2148

Gladders M. D., Yee H. K. C., Majumdar S., Barrientos L. F., Hoekstra H., Hall P. B., Infante L., 2007, , 655, 128

Gómez P. L., et al., 2003, , 584, 210

Grudić M. Y., Hopkins P. F., Faucher-Giguère C.-A., Quataert E., Murray N., Kereš D., 2018, , 475, 3511

Gunn J. E., Gott J. Richard I., 1972, , 176, 1

Hatch N. A., Muldrew S. I., Cooke E. A., Hartley W. G., Almaini O., Simpson C. J., Conselice C. J., 2016, , 459, 387

Hennig C., et al., 2017, , 467, 4015

Herschel W., 1785, Philosophical Transactions of the Royal Society of London Series I, 75, 213

Holmberg E., 1958, Meddelanden fran Lunds Astronomiska Observatorium Serie II, 136, 1

Hubble E. P., 1925, Popular Astronomy, 33, 252

Hubble E., 1926a, , 38, 258

Hubble E., 1926b, Contributions from the Mount Wilson Observatory / Carnegie Institution of Washington, 324, 1

Hubble E. P., 1936, Realm of the Nebulae

Hubble E., Humason M. L., 1931, Contributions from the Mount Wilson Observatory / Carnegie Institution of Washington, 427, 1

Ivezić Ž., Vivas A. K., Lupton R. H., Zinn R., 2005, , 129, 1096

Joseph R. D., Wright G. S., 1985, , 214, 87

Jr. F. J. M., 1951, Journal of the American Statistical Association, 46, 68

Kauffmann G., White S. D. M., Heckman T. M., Ménard B., Brinchmann J., Charlot S., Tremonti C., Brinkmann J., 2004, , 353, 713

Kennicutt R. C. J., 1983, , 88, 483

Kennicutt Robert C. J., 1998, , 36, 189

Kent S. M., 1985, , 59, 115

Kipper R., Tamm A., Tempel E., de Propris R., Ganeshaiah Veena P., 2021, , 647, A32

Klypin A., Yepes G., Gottlöber S., Prada F., Heß S., 2016, Monthly Notices of the Royal Astronomical Society, 457, 4340

Kravtsov A. V., Borgani S., 2012, , 50, 353

Kriek M., van Dokkum P. G., Labbé I., Franx M., Illingworth G. D., Marchesini D., Quadri R. F., 2009, , 700, 221

Kron R. G., 1980, , 43, 305

Kurk J., et al., 2009, , 504, 331

Larson R. B., Tinsley B. M., Caldwell C. N., 1980, , 237, 692

Lilly S. J., Fevre O. L., Crampton D., Hammer F., Tresse L., 1995, The Astrophysical Journal, 455, 50

Lin L., et al., 2008, , 681, 232

Liu Q., Li C., Wanga V., Shepherd B. E., 2018, Biometrics, 74, 595

Lotz J. M., Primack J., Madau P., 2004, , 128, 163

Lotz J. M., Jonsson P., Cox T. J., Primack J. R., 2008a, , 391, 1137

Lotz J. M., et al., 2008b, , 672, 177

Lotz J. M., Jonsson P., Cox T. J., Primack J. R., 2010, , 404, 575

Luisi M., et al., 2021, Science Advances, 7, eabe9511

Madau P., Dickinson M., 2014, , 52, 415

Mantz A. B., et al., 2014, , 794, 157

Mantz A. B., et al., 2018, , 620, A2

McCarthy I. G., Frenk C. S., Font A. S., Lacey C. G., Bower R. G., Mitchell N. L., Balogh M. L., Theuns T., 2008, , 383, 593

Meekins J. F., Fritz G., Chubb T. A., Friedman H., 1971, , 231, 107

Mehrtens N., et al., 2012, , 423, 1024

Merritt D., 1999, , 111, 129

Messier C., 1781, Catalogue des Nébuleuses et des Amas d'Étoiles (Catalog of Nebulae and Star Clusters), Connoissance des Temps ou des Mouvements Célestes, for 1784, p. 227-267

Mihos J. C., Hernquist L., 1996, , 464, 641

Mo H., van den Bosch F. C., White S., 2010, Galaxy Formation and Evolution

Momcheva I. G., et al., 2016, , 225, 27

Moore B., Lake G., Quinn T., Stadel J., 1999, , 304, 465

Muldrew S. I., et al., 2012, , 419, 2670

Neistein E., van den Bosch F. C., Dekel A., 2006, , 372, 933

Noordeh E., Canning R. E. A., Willis J. P., Allen S. W., Mantz A., Stanford S. A., Brammer G., 2021, , 507, 5272

Norberg P., et al., 2002, , 332, 827

Papovich C., et al., 2012, , 750, 93

Papovich C., et al., 2018, , 854, 30

Pearson W. J., et al., 2019, , 631, A51

Peng C. Y., Ho L. C., Impey C. D., Rix H.-W., 2002, , 124, 266

Pierre M., et al., 2004, , 2004, 011

Postman M., et al., 2005, , 623, 721

Quadri R. F., Williams R. J., Franx M., Hildebrandt H., 2012, , 744, 88

Riebe K., et al., 2013, Astronomische Nachrichten, 334, 691

Rodriguez-Gomez V., et al., 2019, , 483, 4140

Rykoff E. S., et al., 2014, , 785, 104

Sanders D. B., Mirabel I. F., 1996, , 34, 749

Sazonova E., et al., 2020, , 899, 85

Sérsic J. L., 1963, Boletin de la Asociacion Argentina de Astronomia La Plata Argentina, 6, 41

Shimizu M., Kitayama T., Sasaki S., Suto Y., 2003, , 590, 197

Simard L., Mendel J. T., Patton D. R., Ellison S. L., McConnachie A. W., 2011, , 196, 11

Skelton R. E., et al., 2014, , 214, 24

Smith S., 1936, , 83, 23

Smith G. P., Treu T., Ellis R. S., Moran S. M., Dressler A., 2005, , 620, 78

Spearman 2008, Spearman Rank Correlation Coefficient. Springer New York, New York, NY, pp 502–505, doi:10.1007/978-0-387-32833-1˙379, https://doi.org/10.1007/978-0-387-32833-1_379

Springel V., 2005, , 364, 1105

Stasielak J., Stachniewicz S., Kutschera M., 2007, in Island Universes. p. 565 (arXiv:astro-ph/0612071), doi:10.1007/978-1-4020-5573-7˙97

Stewart S. G., et al., 1999, arXiv e-prints, pp astro–ph/9910098

Strazzullo V., Paolillo M., Longo G., Puddu E., Djorgovski S. G., De Carvalho R. R., Gal R. R., 2005, , 359, 191

Strazzullo V., et al., 2010, , 524, A17

Strazzullo V., et al., 2019, , 622, A117

Sunyaev R. A., Zeldovich Y. B., 1970, , 7, 3

Tempel E., Saar E., Liivamägi L. J., Tamm A., Einasto J., Einasto M., Müller V., 2011, , 529, A53

Tran K.-V. H., et al., 2010, , 719, L126

Trudeau A., Willis J. P., Rennehan D., Canning R. E. A., Carnall A. C., Poggianti B., Noordeh E., Pierre M., 2022, , 515, 2529

Veale M., Ma C.-P., Greene J. E., Thomas J., Blakeslee J. P., Walsh J. L., Ito J., 2018, , 473, 5446

Visvanathan N., Sandage A., 1977, , 216, 214

Vulcani B., et al., 2011, , 412, 246

Webb T., et al., 2013, The Astronomical Journal, 146, 84

Werner S. V., Hatch N. A., Matharu J., Gonzalez A. H., Bahé Y. M., Mei S., Noirot G., Wylezalek D., 2023, , 523, 91

Willis J. P., et al., 2013, , 430, 134

Willis J. P., et al., 2020, , 577, 39

Wilson G., et al., 2009, , 698, 1943

Wolf M., 1908, Publikationen des Astrophysikalischen Instituts Koenigstuhl-Heidelberg, 3, 109

Wolf C., Gray M. E., Aragón-Salamanca A., Lane K. P., Meisenheimer K., 2007, , 376, L1

York D. G., et al., 2000, The Astronomical Journal, 120, 1579

Zhong Y., Inoue A. K., Yamanaka S., Yamada T., 2022, , 925, 157

Zwicky F., 1933, Helvetica Physica Acta, 6, 110

Zwicky F., 1937, , 86, 217

de Vaucouleurs G., 1959, Handbuch der Physik, 53, 275

de Vaucouleurs G., 1961, , 5, 233

van der Burg R. F. J., et al., 2020, , 638, A112

Łokas E. L., Mamon G. A., 2003, Monthly Notices of the Royal Astronomical Society, 343, 401

Appendix A

Additional Information

A.1 Smoothness Measurement

The Smoothness measurement for the cluster members do not give conclusive results. The SNR of the HST images may not be sufficient for accurate measurements of this index.

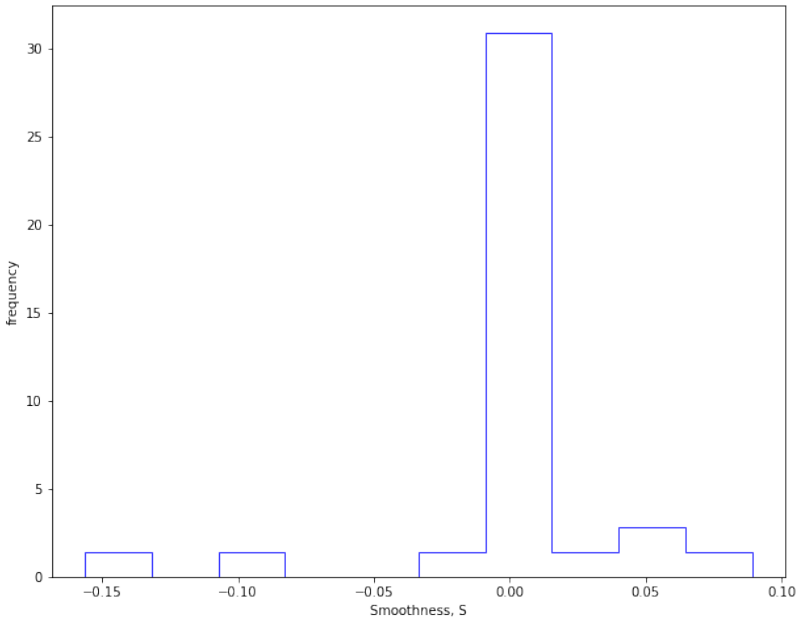

Figure A.1: Histogram showing the distribution of Smoothness measurements for the cluster members.

A.2 Morphological Measurement of ID 661

ID 661 is a neighbouring galaxy to the BCG of XLSSC 122 (Top of Fig.A.2). Its segmentation map is highly contaminated by the light from the BCG, which may have led to the unexpected high Gini value measured. Manipulating the segmentation map to feed into STATMORPH does not improve the measurement.

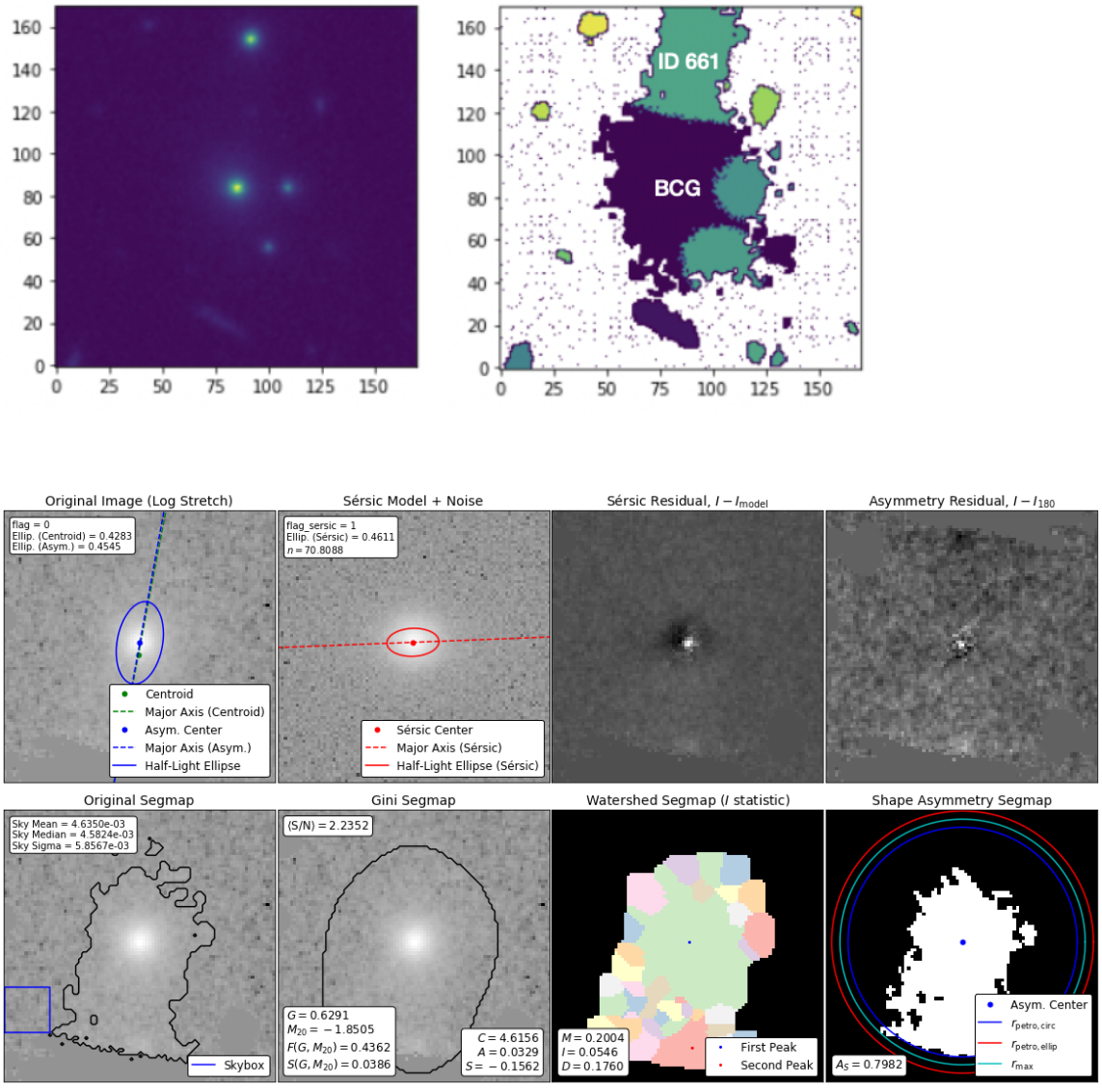

Figure A.2: *Top:* Cutout of the image and segmentation map for the BCG and neighbouring galaxies. *Bottom:* Result from STATMORPH analysis of ID 661.

A.3 Map of XLSSC 122

Position of the different types of cluster members in XLSSC 122.

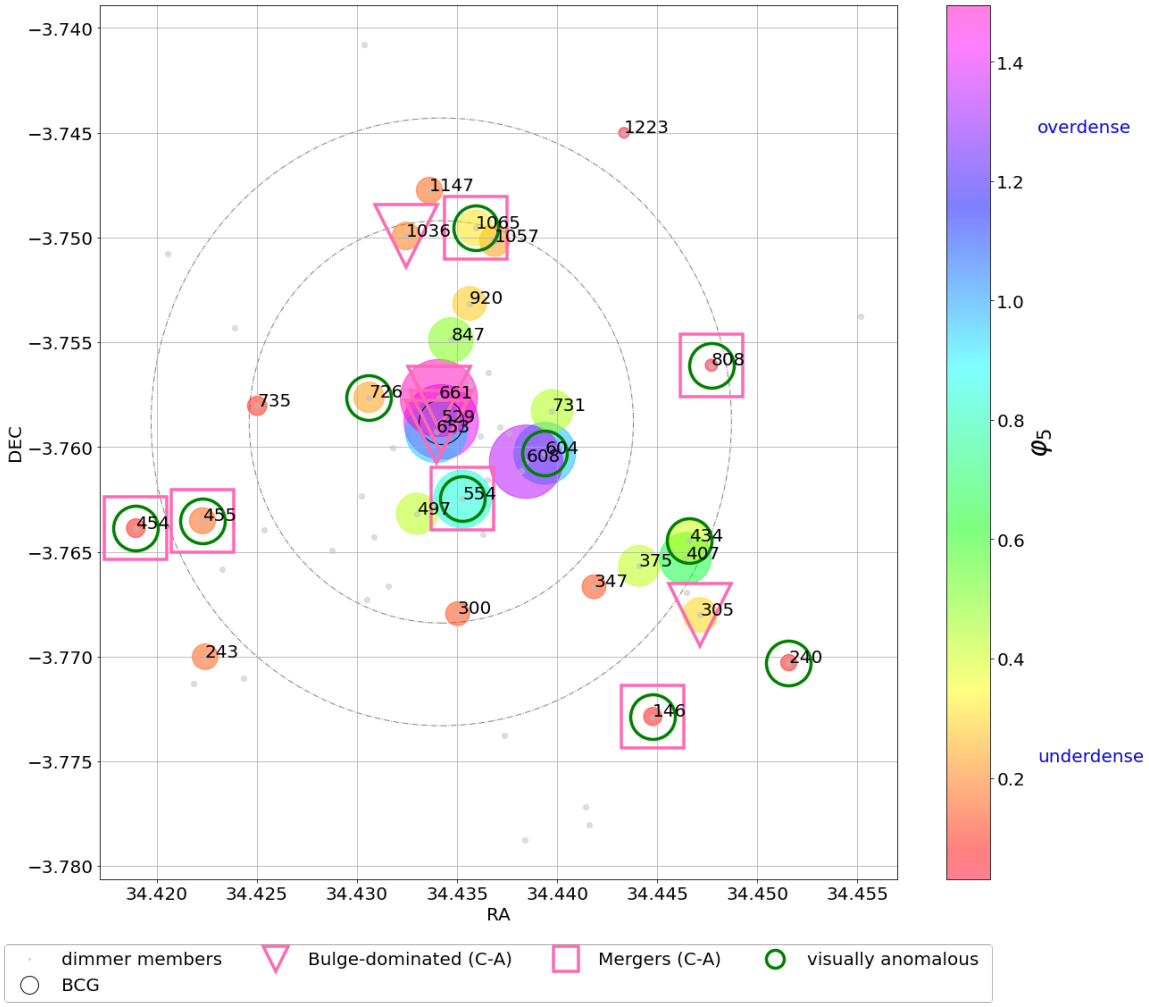

Figure A.3: Replica of Figure 2.17 with the ID of the XLSSC 122 members.

A.4 Mass Growth Curve

Mass growth curves of the 30 most massive subhaloes in a randomly selected XLSSC 122-like halo from *MDPL2* and *SMDPL*.

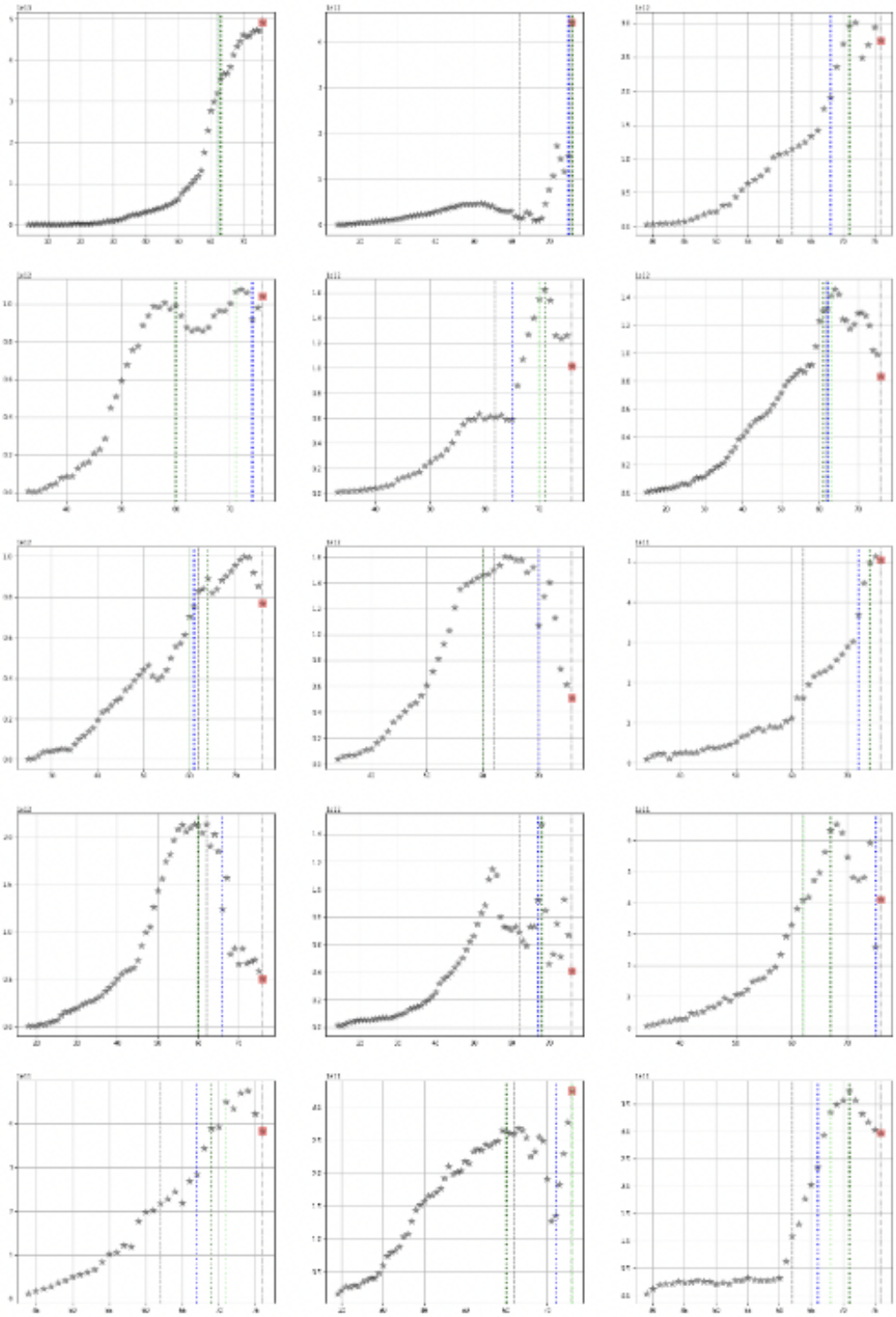

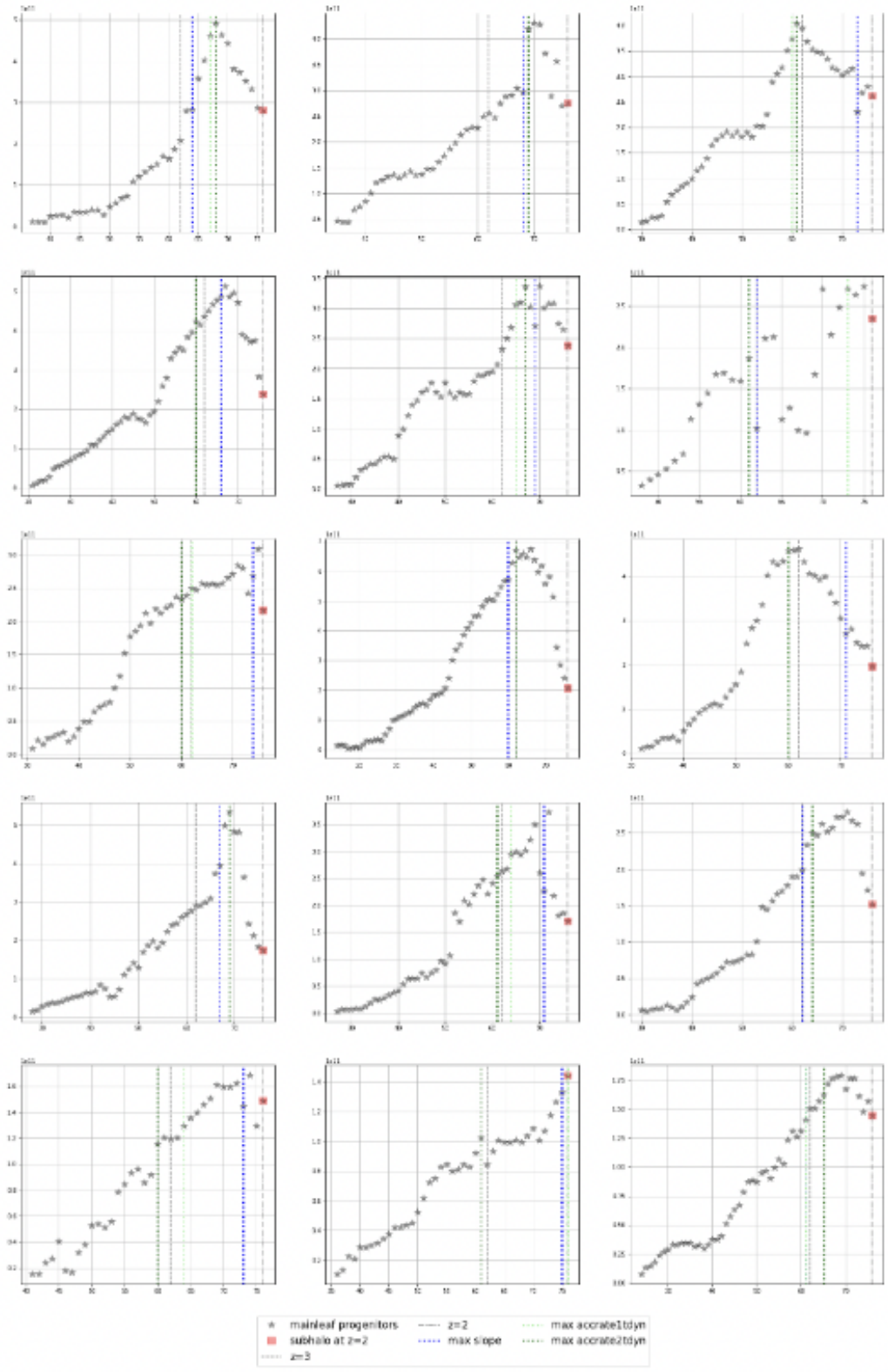

Figure A.4: Mass Growth Curve of the 30 subhaloes in XLSSC 122-like halo from *MDPL2*.

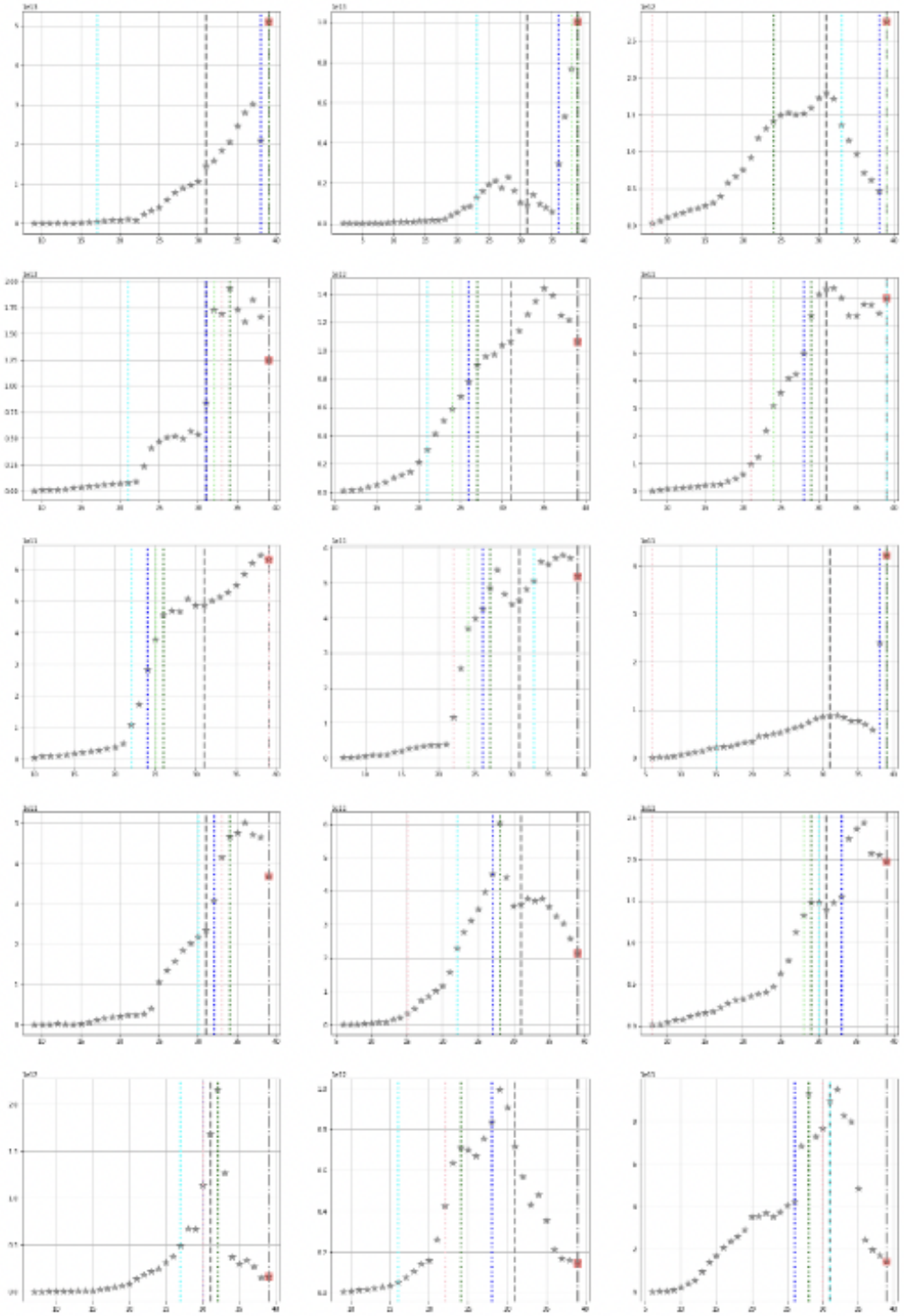

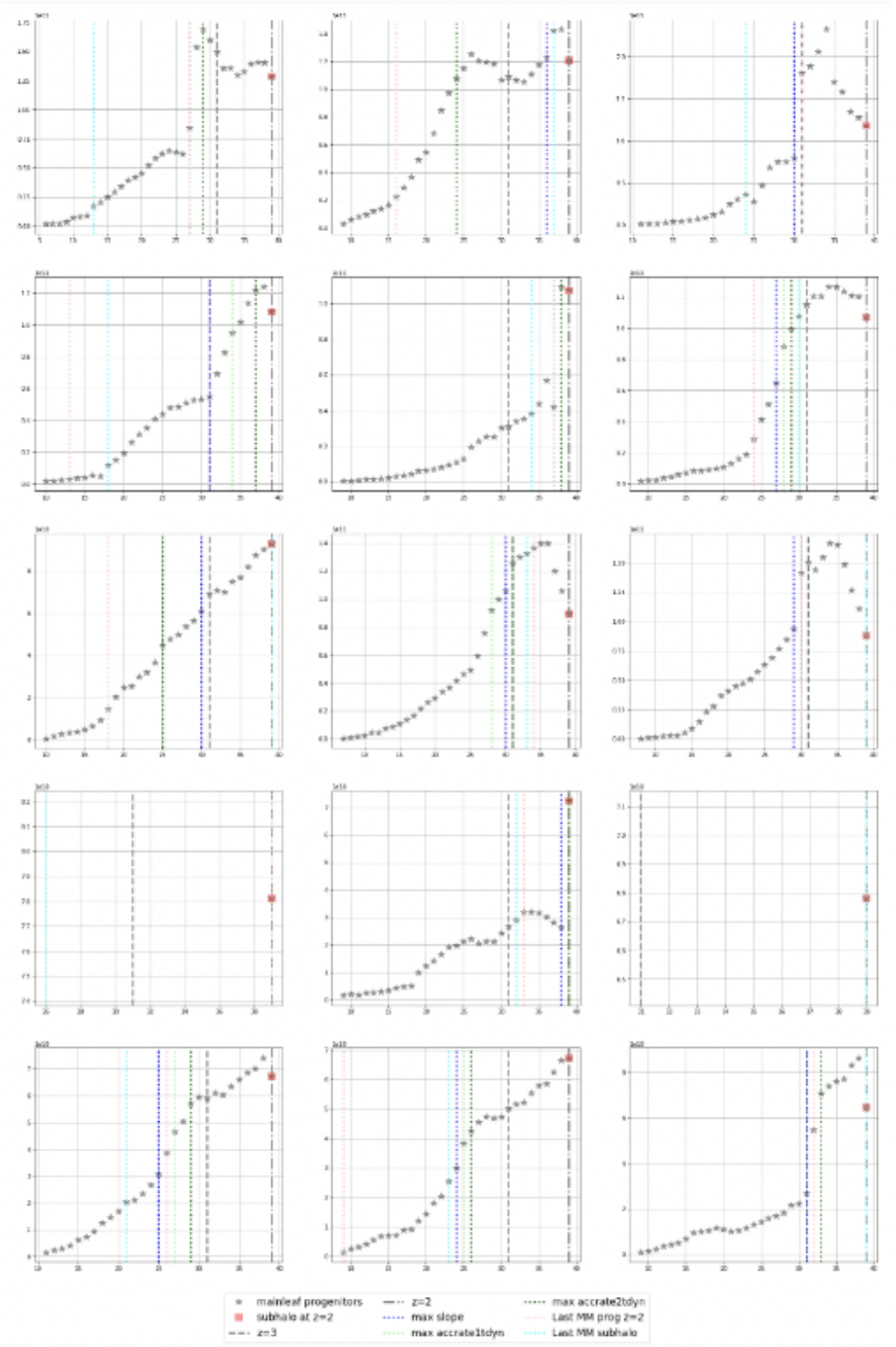

Figure A.5: Mass Growth Curve of the 30 subhaloes in XLSSC 122-like halo from *SMDPL*.

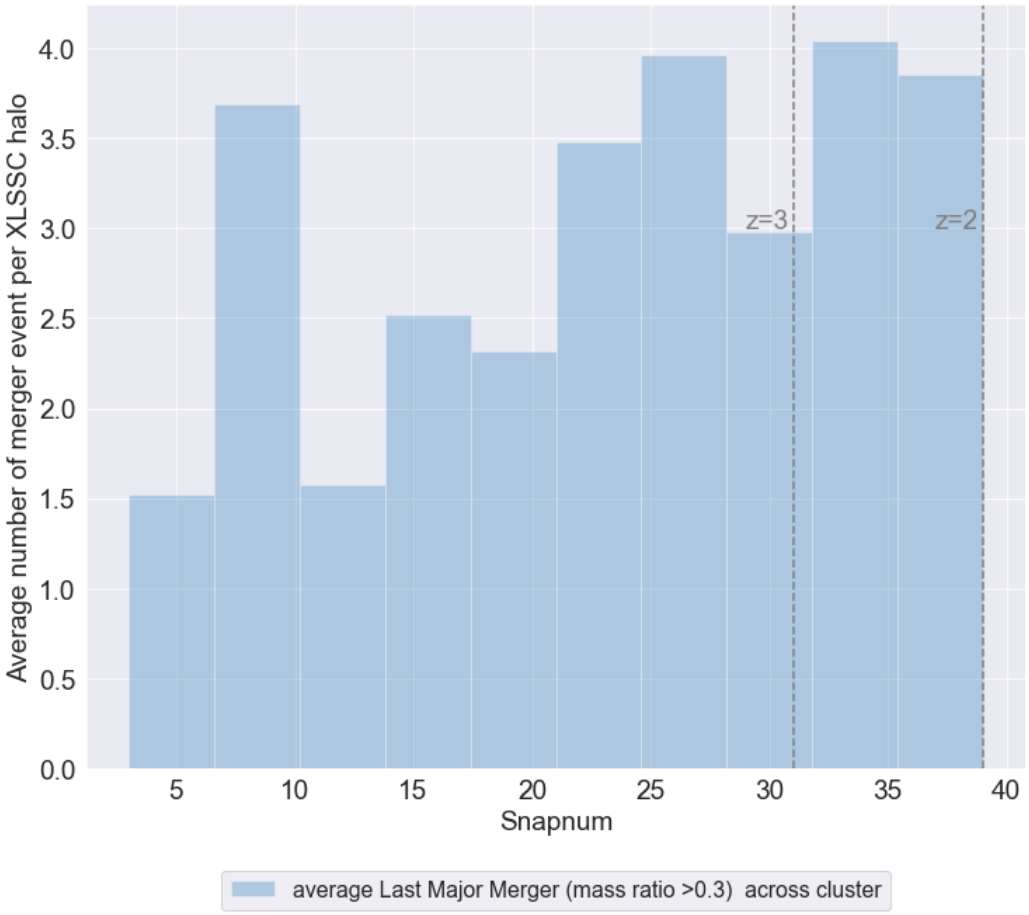

Figure A.6: Timestep Last Major Merger event measurement from ROCKSTAR